



HAL
open science

Fundamental and Harmonic Ultrasound Image Joint Restoration

Mohamad Hourani

► **To cite this version:**

Mohamad Hourani. Fundamental and Harmonic Ultrasound Image Joint Restoration. Image Processing [eess.IV]. Institut National Polytechnique de Toulouse - INPT, 2022. English. NNT: 2022INPT0002 . tel-04189983

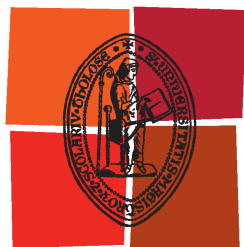
HAL Id: tel-04189983

<https://theses.hal.science/tel-04189983v1>

Submitted on 29 Aug 2023

HAL is a multi-disciplinary open access archive for the deposit and dissemination of scientific research documents, whether they are published or not. The documents may come from teaching and research institutions in France or abroad, or from public or private research centers.

L'archive ouverte pluridisciplinaire **HAL**, est destinée au dépôt et à la diffusion de documents scientifiques de niveau recherche, publiés ou non, émanant des établissements d'enseignement et de recherche français ou étrangers, des laboratoires publics ou privés.



Université
de Toulouse

THÈSE

En vue de l'obtention du

DOCTORAT DE L'UNIVERSITÉ DE TOULOUSE

Délivré par :

Institut National Polytechnique de Toulouse (Toulouse INP)

Discipline ou spécialité :

Informatique et Télécommunication

Présentée et soutenue par :

M. MARCEL MOHAMAD HOURANI

le mardi 4 janvier 2022

Titre :

Fundamental and Harmonic Ultrasound Image Joint Restoration

Ecole doctorale :

Mathématiques, Informatique, Télécommunications de Toulouse (MITT)

Unité de recherche :

Institut de Recherche en Informatique de Toulouse (IRIT)

Directeur(s) de Thèse :

M. DENIS KOUAMÉ

M. JEAN-YVES TOURNERET

Rapporteurs :

MME NICOLAS BARBARA, CNRS

MME RUAN SU, UNIVERSITE DE ROUEN

Membre(s) du jury :

M. JEAN-MARC GIRAULT, GROUPE ESEO ANGERS, Président

M. ADRIAN BASARAB, UNIVERSITE LYON 1, Membre

M. DENIS KOUAMÉ, UNIVERSITE PAUL SABATIER, Membre

M. JEAN-YVES TOURNERET, TOULOUSE INP, Membre

Acknowledgements

Firstly, I would like to express my sincere gratitude to my supervisors professors Adrian Basarab, Jean-Yves Tourneret and Denis Kouamé. You convincingly guided and encouraged me professionally and personally when the roads got tough. This thesis would not be possible without your guidance, mentoring, and encouragement. I am very grateful to all the insightful discussions and to all the life and professional lessons that I will carry my whole life.

Also, I would like to thank my PhD jury members: professors Barbara Nicolas, Jean-Marc Girault and Su Ruan, for their time and effort reading my manuscript. Thanks to your intuitive roles, insightful comments, and encouragement concerning my work.

I would like to particularly thank Professor Jean-Marc Girault for believing in my potential and motivation to research during my master's year. You granted me this opportunity by your support in August 2016.

I would thank all MINDS team at IRIT for being there, for the fruitful discussions that we had. I would particularly thank Oumaima for sharing the office with me for 3 years and being always there when i needed help and for the support specially when extra hours of work was needed. I would always thank Janka for being the mentor, for the experienced advises on the personal and the scientific levels.

I would like to thank the doctoral school EDMIITT for offering me the opportunity of being part of its office. I would thank particularly Agnès Requis for presenting me the administrative work in academia and its complications and for the coffee breaks and many of delicious cookies.

I want to thank the 'Association les amis du Liban- Toulouse' family, specially Paul, Farid, Roula,

Elena, Anthony, Maen, i learnt a lot from you and you were always supportive in each step i took. These years were a little bit rough, a challenging test where i tend to spend the time by myself. I would thank in particular Tohme, Yara, Patricia, Maroun, Ali k., Ali J., Ranine, Carmella, Carine, Inès, Rana, Michella, Jihane, Said, Yara Saleme, Joseph, Hadi. You were my second family here in Toulouse, and i want you to know that your support was the main element to overcome all the challenges specially in COVID period. I want to thank Catherine, the friend with whom i rarely met, yet a strong friendship was built full of support and long phone calls. Thank you all for being there for me.

I want to thank particularly the 'Caféclopéstan' (Wafaa, Flo, Oihana, Elio, Anthony, François) for sharing unforgettable memories on the balcony of IRIT, for all the coffee breaks and the giggles.

I want to thank my lifetime friends Rihab, khaled, Mahmoud, and Bob. Despite that each one of us is living in a continent, however, late night calls were always our way to keep pushing each others. Thank you for being always here.

My family, i can't thank you for all your sacrifices that you did in order to reach my dream. I hope that i made you proud. My mother, you was my number one supporter since day one, thank you for believing in me and my projects. My father, you always said to me that all this hard work will pay off once you reach you dreams. I hope that i made you proud today. To my sisters: Nancy you was here "literally" from day one, you supported me in every step on this road and i'll be always here for you, twin. Katia, you told me always to that you inspired your ambition from mine, these words was always keep me pushing forwards. To my brother, Ali, your smile, your power, you ability to overcome the hardest disabilities will be always my source of inspiration. Keep smiling buddy, you give us the sense of living each day. For my grandfather, i know that you want to be here to see me this day unfortunately Covid was the winner this time. But i know that you are watching me from the sky with grandmother besides you smiling. I hope i made you proud. Cheers.

نحن أحياء وبقون وللحلم بقية...

محمود درويش

We are living and staying, and the dream is to be continued ...

Mahmoud Darwish

Résumé

L'imagerie ultrasonore conserve sa place parmi les principales modalités d'imagerie en raison de ses capacités à révéler l'anatomie et à inspecter le mouvement des organes et le flux sanguin en temps réel, d'une manière non invasive et non ionisante, avec un faible coût, une facilité d'utilisation et une grande vitesse de reconstruction des images. Néanmoins, l'imagerie ultrasonore présente des limites intrinsèques en termes de résolution spatiale.

L'amélioration de la résolution spatiale des images ultrasonores est un défi actuel et de nombreux travaux ont longtemps porté sur l'optimisation du dispositif d'acquisition. L'imagerie ultrasonore à haute résolution atteint cet objectif grâce à l'utilisation de sondes spécialisées, mais se confronte aujourd'hui à des limites physiques et technologiques.

L'imagerie harmonique est la solution intuitive des spécialistes pour augmenter la résolution lors de l'acquisition. Cependant, elle souffre d'une atténuation en profondeur. Une solution alternative pour améliorer la résolution est de développer des techniques de post-traitement comme la restauration d'images ultrasonores.

L'objectif de cette thèse est d'étudier la non-linéarité des échos ultrasonores dans le processus de restauration et de présenter l'intérêt d'incorporer des images US harmoniques dans ce processus. Par conséquent, nous présentons une nouvelle méthode de restauration d'images US qui utilise les composantes fondamentales et harmoniques de l'image observée. La plupart des méthodes existantes sont basées sur un modèle linéaire de formation d'image. Sous l'approximation de Born du premier ordre, l'image RF est supposée être une convolution 2D entre la fonction de réflectivité et la réponse impulsionnelle du système. Par conséquent, un problème inverse résultant est formé et résolu en

utilisant un algorithme de type ADMM. Plus précisément, nous proposons de récupérer la fonction de réflectivité inconnue en minimisant une fonction composée de deux termes de fidélité des données correspondant aux composantes linéaires (fondamentale) et non linéaires (première harmonique) de l'image observée, et d'un terme de régularisation basé sur la parcimonie afin de stabiliser la solution. Pour tenir compte de l'atténuation en profondeur des images harmoniques, un terme d'atténuation dans le modèle direct de l'image harmonique est proposé sur la base d'une analyse spectrale effectuée sur les signaux RF observés. La méthode proposée a d'abord été appliquée en deux étapes, en estimant d'abord la réponse impulsionnelle, suivi par la fonction de réflectivité. Dans un deuxième temps, une solution pour estimer simultanément la réponse impulsionnelle et la fonction de réflectivité est proposée, et une autre solution pour prendre en compte la variabilité spatiale de la réponse impulsionnelle est présentée. L'intérêt de la méthode proposée est démontré par des résultats synthétiques et *in vivo* et comparé aux méthodes de restauration conventionnelles.

Abstract

Ultrasound imaging maintains its position among the leading imaging modalities because of its abilities to reveal anatomy and inspect organ movement and blood flow in real time, with noninvasive, non-ionizing risk, low cost, ease of use, and high speed of image reconstruction. Nevertheless, ultrasound imaging has some intrinsic limitations in terms of its spatial resolution.

Improving the spatial resolution of ultrasound images is a current challenge and many works have long been concerned with the optimization of the acquisition device. High-resolution ultrasound imaging achieves this goal through the use of specialized probes, but is now encountering physical and technological limitations.

Harmonic imaging is the intuitive solution for specialists to increase the resolution during acquisition. However, it suffers from attenuation at depth. An alternative solution to improve resolution is to develop post-processing techniques as restoration of ultrasound images.

The objective of this PhD thesis is to investigate the non-linearity of ultrasound echoes in the restoration process and present the interest of incorporating harmonic US images into the process. Therefore, we present a new US image restoration method that utilizes the fundamental and harmonic components of the observed image. Most of the existing methods are based on a linear image formation model. Under the first-order Born approximation, the RF image is assumed to be a 2D convolution between the TRF and the point spread function of the system. Therefore, a resulting inverse problem is formed and solved using an ADMM-like algorithm. More specifically, we propose to recover the unknown TRF by minimizing a function composed of two data fidelity terms corresponding to the linear (fundamental) and nonlinear (first harmonic) components of the observed image, and a

sparsity-based regularization term to stabilize the solution. To account for the attenuation in the depth of harmonic images, an attenuation term in the direct model of the harmonic image is proposed based on a spectral analysis performed on the observed RF signals. The proposed method was first applied in a two-step manner: first estimating PSF, followed by estimating TRF. In a second step, a solution to simultaneously estimate the PSF and the TRF is proposed, and another solution to account for the spatial variability of the PSF is presented. The interest of the proposed method is shown on synthetic and *in vivo* results and compared with the conventional restoration methods.

Acronyms

ADMM	Alternating Direction Method of Multipliers
AL	Augmented Lagrangian
AMP	Approximate Message Mapping
ARMA	Autoregressive Moving Average
AWGN	Additive White Gaussian Noise
BCCB	Block Circulant with Circulant Block
CMUTs	Capacitive Micromachined Ultrasound Transducers
CNR	Contrast-to-Noise Ratio
C-SALSA	Constrained Salsa
CT	Computed Tomography
DAS	Delay and Sum
EM	Expectation Maximization
FISTA	Fast ISTA
FOV	Field Of View
FWHM	Full Width at Half Maximum
GGD	Generalized Gaussian Distribution

GSPR	Gradient Projection Method
HIFU	High Intensity Focused Ultrasound
HOS	Higher-Order Statistics
INPT	Institut national polytechnique de Toulouse
IRIT	Institut de Recherche en Informatique de Toulouse
IRLS	Iteratively Reweighted Least Square
ISTA	Iterative Shrinkage-Thresholding Algorithm
i.i.d	Independent and Identically Distributed
MAP	Maximum A Posteriori
ML	Maximum Likelihood
MRI	Magnetic Resonance Image
NRMSE	Normalized Root Mean Square Error
NESTA	Nesterov's algorithm
PDE	Partial Differential Equation
PDF	Probability Density Function
PFB	Proximal Forward Backward
PI	Pulse Inversion
PSF	Point Spread Function
PZT	Piezoelectric Zirconate Titanate
REC	Resolution Enhancement Compression
RF	Radio-Frequency
RG	Resolution Gain
RMSE	Root Mean Square Error

SALSA	Split Augmented Lagrangian Shrinkage Algorithm
SAR	Synthetic Aperture Radar
SIMO	Single-Input Multiple-Output
SNR	Signal-to-Noise Ratio
SPARSA	Sparse Reconstruction by Separable Approximation
SRAD	Speckle Reducing Anisotropic Diffusion
SSIM	Structural Similarity Index Measure
TRF	Tissue Reflectivity Function
THI	Tissue Harmonic Imaging
TV	Total Variation
TwIST	Two Steps IST
TX	Transmission
UCA	Ultrasound Contrast Agents
US	Ultrasound

Contents

Acknowledgements	iii
Résumé	vii
Abstract	ix
Acronyms	xi
Chapter 1 Introduction	1
1.1 Context of ultrasound imaging	2
1.2 Physics of Ultrasound	5
1.2.1 Piezoelectric elements and transducers	5
1.2.2 Ultrasound wave propagation	6
1.2.3 Linear propagation	6
1.2.4 Nonlinear propagation	8
1.2.4.1 Nonlinear parameter	8
1.2.4.2 Wave distortion	9
1.2.4.3 Nonlinear propagation equation	12
1.2.5 Reflection and transmission	12
1.2.6 Scattering	14
1.2.7 Attenuation and penetration	15
1.3 Ultrasound image formation	16

1.3.1	Imaging principle	16
1.3.2	Beamforming to RF image	17
1.3.3	US image modes	19
1.3.3.1	A-mode	19
1.3.3.2	M-mode	20
1.3.3.3	B-mode	20
1.3.3.4	Doppler Mode	21
1.3.4	Spatial resolution	23
1.3.4.1	Axial resolution	23
1.3.4.2	Lateral resolution	23
1.3.4.3	Azimuthal resolution	24
1.3.5	Speckle	25
1.4	Open challenges	25
1.4.1	Organization of the manuscript:	26
List of publications		29
Chapter 2 Stat-of-art : Ultrasound image restoration		31
2.1	Introduction	32
2.2	US image formation model	32
2.2.1	Incident pressure	34
2.2.2	Scattered pressure field	34
2.2.3	Force on the received aperture	36
2.2.4	RF voltage	36
2.2.5	2D image model	37
2.3	Pre-processing techniques	38
2.3.1	Modern beamforming techniques	38
2.3.1.1	Dynamic focusing	38
2.3.1.2	Synthetic aperture	39

2.3.1.3	Coded transmission and pulse compression	39
2.3.2	Compounding	41
2.3.3	Harmonic imaging	43
2.3.4	Pulse inversion	45
2.4	Post processing techniques	46
2.4.1	Filtering	46
2.4.2	Deconvolution	49
2.4.2.1	Point spread function (PSF)	50
2.4.2.2	Problem statement	53
2.4.2.3	Regularizations	54
2.5	Blind image deconvolution	58
2.5.1	Deconvolution with pre-estimated PSF	59
2.5.2	Fully blind deconvolution	61
2.6	Orientations	61
Chapter 3 Joint ultrasound image deconvolution		63
3.1	Introduction	64
3.2	US image formation models	65
3.3	Problem reformulation	66
3.4	Optimization	67
3.4.1	Basics of the Alternating Direction Method of Multipliers	67
3.4.2	Proposed ADMM parametrization	68
3.4.3	Implementation details	69
3.5	PSF estimation	71
3.6	Data and evaluation metrics	73
3.6.1	Data simulation and acquisition	73
3.6.1.1	Synthetic data	73
3.6.1.2	Experimental images	74

3.6.2	Spectral analysis of the experimental data	76
3.6.3	Quantitative metrics	78
3.7	Results and discussion	79
3.7.1	Results on synthetic data	80
3.7.1.1	Supervised approach	80
3.7.1.2	Joint deconvolution with pre-estimated PSF approach	84
3.7.2	Results on phantom and real images	89
3.7.2.1	Phantom image	89
3.7.2.2	Carotid results	92
3.8	Discussion	95
3.9	Conclusion and perspectives	98
Chapter 4 On the fully blind and block-wise joint restoration		99
4.1	Introduction	100
4.2	Fully blind joint deconvolution	100
4.2.1	Problem reformulation	101
4.2.2	Optimization algorithm	101
4.2.2.1	TRF estimation	102
4.2.2.2	PSF estimation	102
4.2.3	Results	103
4.2.3.1	Simulated image	104
4.2.3.2	Phantom image	108
4.2.3.3	Carotid image	110
4.2.4	Discussion	112
4.3	Joint deconvolution with a spatially varying PSF	114
4.3.1	Block-wise joint deconvolution	115
4.3.2	Results	116
4.4	Conclusion	120

Chapter 5	Conclusions and perspectives	121
	Conclusions and perspectives	121
5.1	Conclusions	121
5.2	Future work and perspectives	122
	Appendices	125
	Appendix A Blurring operator in spatial and frequency domains	127
A.1	Block circulant matrix with circulant blocks	127
A.2	Spectral decomposition of the BCCB matrix	129
	Bibliography	153

List of Figures

1.1	(a-c) Direct , (d-e) inverse piezoelectric effect [MF06].	5
1.2	US probe linear array on the left, curvilinear array on the right [Tou14].	6
1.3	(a) Plane wave and (b) Spherical wave [Mor13].	7
1.4	Distortion of US waves due to nonlinearity: (a) Sinusoidal pressure wave transmitted at $z = 0$ and (b) after $z = 500$ mm . In the Fourier spectrum, (c) the harmonics are initially not visible and appear in (d) due to wave distortion. The illustration has been obtained for a 3 MHz wave with an initial pressure of 100 kPa after 500 mm of propagation in water ($B/A = 5$) [Var11].	11
1.5	Reflection and transmission on the boundaries of two regions.	13
1.6	(a) Specular (mirror effect) and (b) scattering [Kou].	15
1.7	Block diagram of US imaging process.	17
1.8	(a) Convex array transducer, (b) Linear array transducer, (c) Phased array transducer [Sza16].	18
1.9	Delay-and-sum beamforming in a phased array ultrasound imaging system [JKKY05].	19
1.10	A-mode graph [PL06].	20
1.11	(a) Scheme for obtaining the M-Mode, (b) an M-Mode example in cardiac imaging [Sza04]	21
1.12	Relationship between RF and B-mode image for a thyroid image [Bas08]. (a) RF image, (b) B-Mode image, (c) an extraction of axial profile, RF signal in blue and corresponding envelope in red	22

1.13	Doppler effect application in medical US imaging.	22
1.14	(a) A high frequency wave with a short pulse length, (b) A low frequency wave with a long pulse length [Che16]	24
1.15	lateral resolution in US imaging.	24
2.1	Coordinate system of the scattering field [NPK ⁺ 06].	35
2.2	Basic principle of synthetic aperture method [Nik02].	40
2.3	Simulated impulse responses, chirps, and convolutions. (a) Pulse with approximately 48 % 3 dB pulse/echo bandwidth. (b) Pulse with approximately 97 % 3 dB pulse/echo bandwidth. (c) Modified chirp used to excite the 48% bandwidth source. (d) Linear chirp used to excite the 97% bandwidth source. (e) Convolution of the pulses with their respective chirps sequences. [Oel07].	41
2.4	Spatial compounding. A, diagram of sound waves transmitted and received at multiple different angles in spatial compounding. B, conventional US image of a mass without spatial compounding. C, US image with spatial compounding of the same mass, which accentuates lesion boundaries and increased lesion conspicuity. D, left breast mammogram in the craniocaudal view showing a popcorn-like calcification in the outer breast. E, correlative conventional US image of the popcorn-like calcification showing posterior acoustic shadowing. F, Ultrasound image of the same calcification with spatial compounding showing complete loss of posterior acoustic features [CHS17]. . .	43
2.5	Representation of pressure pulse distortion at the origin of harmonic US imaging and examples of fundamental and harmonic US images.	46
2.6	Images at (a) the fundamental and (b) second harmonic (bottom) of chronic cholecystitis [TGEP99]	47
2.7	Point spread function phantom simulated using the Field II software [Jen53]. Different apodization and focolization are employed in each image.	52
2.8	Variation in pressure-pulse shape of an initially Gaussian pulse propagating in a medium with a $1dB/MHz^{1.5} - cm$ absorption for three different increasing propagation distances (z) [Sza04].	52

2.9	(a) Observed B-mode image, (b) restored B-mode images with ℓ_2 -norm, (c) ℓ_1 -norm and (d) ℓ_p -norm (results from [ZBKT16])	58
3.1	Phantom model 404GS LE, Gammex Inc.	75
3.2	Position of the patient’s neck during ultrasound carotid imaging [CAN ⁺ 17].	76
3.3	Carotid image: (a) Spectrum of the original RF image, (b) spectrum of the filtered RF image containing the mixed information from fundamental and harmonic data, (c) spectrum of the fundamental image \mathbf{y}_f after filtering, (d) spectrum of the harmonic image \mathbf{y}_h after filtering, (e) spectrum of one RF line highlighting the fundamental and first harmonic filtering.	77
3.4	Example of weights for the carotid image: (a) Regions used to compute the energies of the fundamental (red) and harmonic (blue) spectra, (b) Diagonal elements of \mathbf{W} with respect to the axial direction.	78
3.5	(a) TRF mimicking a human kidney (\mathbf{r} of size 1150×300 pixels), (b) simulated fundamental image \mathbf{y}_f , (c) simulated harmonic image \mathbf{y}_h , (d) attenuation map used to simulate the harmonic image in (b), whose values are equal to 1 (no attenuation) close to the probe and to 0.3 (high attenuation) at the bottom of the image. Note that all the images are shown in B-mode for better visualisation and with 60 dB dynamic range.	82
3.6	(a) TRF mimicking a human kidney (\mathbf{r} of size 1150×300 pixels), TRF estimated by (b) LASSO-fundamental, (c) LASSO-harmonic, (d) LASSO-sum and (e) proposed method. All the estimated TRFs are obtained using a supervised approach, i.e., using the true PSF. Note that all the images are shown in B-mode for better visualisation and with 60 dB dynamic range.	83
3.7	Estimated TRF using the joint deconvolution with pre-estimated PSF: (a) LASSO-fundamental estimated from the fundamental image in Figure 3.5 (b), (b) LASSO-harmonic estimated from the harmonic image in Figure 3.5(c), (c) LASSO-sum and (d) proposed method. All the TRF were estimated using PSF pre-estimated by homomorphic filtering of the RF images. Note that all the images are shown in B-mode for better visualisation and with 60 dB dynamic range.	85

3.8	Left column shows the fundamental PSF: (a) true, (c) estimated by homomorphic filtering. Right column shows the harmonic PSF: (b) true, (d) estimated by homomorphic filtering.	87
3.9	Results on data simulated with CREANUIS: (a) Fundamental image (blue and green regions are used to compute the CNR), (b) harmonic image (yellow region is used to compute the RG), TRF estimated by (c) LASSO-fundamental, (d) LASSO-harmonic, (e) LASSO-sum, and (f) the proposed method. All the TRF were restored using a PSF pre-estimated by homomorphic filtering. Note that all the images are shown in B-mode for better visualisation and with 60 dB dynamic range.	88
3.10	Results on phantom data: (a) Fundamental image (yellow region is used to compute the RG), (b) harmonic image (blue and green regions are used to compute the CNR), TRF estimated by (c) LASSO-fundamental, (d) LASSO-harmonic, (e) LASSO-sum, and (f) proposed method. All the TRF were restored using a PSF pre-estimated by homomorphic filtering. Note that all the images are shown in B-mode for better visualisation and with 60 dB dynamic range.	90
3.11	Horizontal profile passing by the two cysts (regions 1 and 3) and the wire in between (region 2), the orange line in Figure3.10.(d).	91
3.12	Results on carotid data: (a) Fundamental image (green region is used to compute the RG), (b) harmonic image (blue regions are used to compute the CNR), TRF estimated by (c) LASSO-fundamental, (c) LASSO-harmonic, (d) LASSO-sum, and (e) proposed method. All the TRF were restored using PSF pre-estimated by homomorphic filtering. Note that all the images are shown in B-mode for better visualisation and with 60 dB dynamic range	93
3.13	(a) TRF profiles corresponding to the red line in (b).	94
3.14	Simulation data (a) TRF, (b,c,d) joint solution with l-1 norm, l-p norm (p=3/2), lp norm (p=4/3).	96
3.15	Illustration of the influence of the hyperparameter μ on the result in terms of (a) PSNR and (b) NRMSE.	97

3.16	Illustration of the influence of the hyperparameter β on the result in terms of (a) PSNR and (b) NRMSE.	97
4.1	(a) TRF mimicking a human kidney (\mathbf{r} of size 1150×300 pixels), (b) simulated fundamental image \mathbf{y}_f , (c) simulated harmonic image \mathbf{y}_h , (d) attenuation map used to simulate the harmonic image in (b), whose values are equal to 1 (no attenuation) close to the probe and to 0.3 (high attenuation) at the bottom of the image. Note that all the images are shown in B-mode for better visualisation.	105
4.2	Estimated TRF using an alternating estimation approach with: (a) LASSO-fundamental estimated from the fundamental image, (b) LASSO-harmonic estimated from the harmonic image, (c) LASSO-sum and (d) proposed method. All the TRF were estimated by alternating the estimation of the PSF explained in Section 4.2.2 and the estimation of the TRF with one of the restoration techniques considered.	106
4.3	The upper row shows the fundamental PSF: (a) true, (b) estimated by homomorphic filtering and (c) estimated by alternative minimization. The lower row shows the harmonic PSF: (d) true, (e) estimated by homomorphic filtering and (f) estimated by alternative minimization.	107
4.4	Wire phantom image: (a) Fundamental B-mode image, (b) Harmonic B-mode image.	108
4.5	Results on phantom data: TRF estimated by (a) LASSO-fundamental, (b) LASSO-harmonic, (c) LASSO-sum, and (d) proposed method. All the TRF were restored using PSF estimated alternatively with the TRF.	109
4.6	Carotid image: (a) Fundamental B-mode image, (b) Harmonic B-mode image.	111
4.7	Results on carotid data: TRF estimated by (a) LASSO-fundamental, (b) LASSO-harmonic, (c) LASSO-sum, and (d) proposed method. All the TRF were restored using PSF estimated alternatively with the TRF.	112
4.8	(a) Zero phase fundamental PSF $\hat{\mathbf{h}}_f$, (b) Estimated fundamental PSF h_f , (c) Zero phase harmonic PSF $\hat{\mathbf{h}}_h$, (d) Estimated harmonic PSF h_h	113
4.9	PSF estimation and image deconvolution using a sequence of estimated PSFs.	115

4.10 Principle of block weighting and weighting functions w_i corresponding to the different PSFs as a function of depth.	116
4.11 Phantom experiment: (a) fundamental image, (b) harmonic image, (c) deconvolution solution using a spatially invariant PSF, and (d) deconvolution solution using the proposed method. The second row shows a zoom corresponding to the rectangular region displayed in (a).	117
4.12 Phantom experiment: gains of FWHM for each wire at each depth in the proposed method and in the joint deconvolution with invariant PSF.	118
4.13 Carotid experiment: (a) fundamental image, (b) harmonic image, (c) deconvolution solution using an invariant PSF, and (d) deconvolution solution using the proposed method.	119

List of Tables

1.1	Comparison of imaging modalities [Sza04].	4
1.2	Acoustical characteristics for some materials [Sza04]	14
1.3	Attenuation coefficient for different type of tissues [Sza04]	16
3.1	Quantitative results corresponding to the images Figure 3.6(b),(c),(d) and (e). The CNR is computed with respect to the rectangular regions shown in Figure 3.5.	84
3.2	Quantitative results corresponding to the images of Figure 3.7.	86
3.3	Quantitative assessment of the estimated PSF with respect to the true PSF.	86
3.4	Quantitative results corresponding to the images of Figure 3.9.	87
3.5	Quantitative results computed from the images of Figure 3.10.	91
3.6	Quantitative results computed from the images in Figure 3.12.	94
3.7	Quantitative results computed from the images in Figure 3.14 using SSIM, RMSE and PSNR.	96
4.1	Quantitative results corresponding to the images of Figure 4.2.	107
4.2	Quantitative assessment of the estimated PSF with respect to the true PSF.	107
4.3	Quantitative results computed from the images of Figure 4.5.	109
4.4	Quantitative results computed from the images of Figure 4.7.	110
4.5	Quantitative results comparing the fundamental and harmonic PSFs estimated by the proposed method in contrast to the smoothing integration method.	111
4.6	Comparison of the computation time of the blind deconvolution methods.	114

CHAPTER 1

Introduction

Contents

2.1	Introduction	32
2.2	US image formation model	32
2.2.1	Incident pressure	34
2.2.2	Scattered pressure field	34
2.2.3	Force on the received aperture	36
2.2.4	RF voltage	36
2.2.5	2D image model	37
2.3	Pre-processing techniques	38
2.3.1	Modern beamforming techniques	38
2.3.1.1	Dynamic focusing	38
2.3.1.2	Synthetic aperture	39
2.3.1.3	Coded transmission and pulse compression	39
2.3.2	Compounding	41
2.3.3	Harmonic imaging	43
2.3.4	Pulse inversion	45
2.4	Post processing techniques	46
2.4.1	Filtering	46
2.4.2	Deconvolution	49
2.4.2.1	Point spread function (PSF)	50
2.4.2.2	Problem statement	53
2.4.2.3	Regularizations	54
2.5	Blind image deconvolution	58
2.5.1	Deconvolution with pre-estimated PSF	59
2.5.2	Fully blind deconvolution	61
2.6	Orientations	61

1.1 Context of ultrasound imaging

An acoustic wave is a mechanical wave that creates vibration in a medium and propagates with a proper sound velocity. During propagation, the sound waves create a successive series of compression and decompression in the adjacent region of the medium in the direction of propagation. The wavelength of the sound waves, λ , is the spatial period where the sound pattern repeats in the medium:

$$\lambda = \frac{c}{f} \quad (1.1)$$

where f is the wave frequency and c is the speed of sound in the medium. In the soft tissues, the average of speed of sound is about 1540 m s^{-1} .

Ultrasound (US) refers to the sound waves with frequencies higher than the upper limit of human hearing which is 20,000 Hz. In the middle of 18th century, Lazzaro Spallanzani discovered that the reflected echoes of inaudible sound help bats to navigate. In the early of the 20th century, the Austrian neurologist Karl Dussik exploited transmitted ultrasound waves for the study of the brain ventricles. Later, the Swedish cardiologist Inge Edler, and the German physicist Carl Hellmuth Hertz were the first to use ultrasound in the study of heart movement, so-called echocardiography, by studying the reflected ultrasound waves [SG07]. Since that discovery, followed by the improvement in the field of electronics in the mid of the 20th century, US imaging is widely used until these days in several medical application for diagnostic and therapeutic reasons:

- Diagnostic ultrasound

In this category, US is mainly used as imaging tool, where US images had become a essential reference for the physician's diagnosis. Thus, US images can be in the following applications:

- Fetal ultrasound imaging is used to examine a fetus during pregnancy. It is also used to view the ovaries and uterus during pregnancy.
- An abdominal ultrasound examines abdominal organs and tissues.
- Breast ultrasound screening can help detect breast cancer in women.

- Bone sonometry is a type of ultrasound imaging that play a growing role in the assessment and management of osteoporosis.
- An echocardiogram is the US imaging of the heart. Echocardiograms are often combined with Doppler ultrasound, which visualizes blood flow through blood vessels and organs.
- Ophthalmic ultrasound examines traumatic eye injuries, evaluates of intraocular tumors, retinal detachment and vascular disease.
- Ultrasound can help assess joint inflammation.
- Pelvic Ultrasound can examine the uterus, bladder, or prostate. A pelvic ultrasound can diagnose abnormal bleeding, pain, menstrual problems, ovarian cysts, kidney or bladder stones, and cancer in the uterus or ovaries.
- Ultrasound skin imaging is used to detect skin cancer and inflammatory conditions as well as in cosmetic.

- Therapeutic Applications

Based on their physical characteristics, the US waves are used, in this case, to treat some medical problems [TH07]. Some typical applications in this category include:

- High intensity focused ultrasound (HIFU) consists of applying high power energy on a focal point. This mechanism leads to instantaneous cell death and coagulative necrosis
- Lithotripsy is used to treat kidney, liver or bladder stones using high energy shock waves.
- Sonophoresis used to increase the penetration of pharmacologically active drugs through the skin.
- Sonothrombolysis can aid the dissolution of blood clots.

There exist many other applications. The therapeutic application of US is out of the scope of this thesis.

Nowaday, US imaging keeps several advantages over other medical imaging modalities. First, US presents one of the lowest cost techniques among medical imaging modalities. US imaging can also

Modality	Ultrasound	X-ray	CT	MRI
Physical agent	Ultrasound	X-ray	X-ray	Magnetic field
Principle	Mechanical properties frequency and axially dependent 0.3 – 3 mm	Mean tissue absorption	Tissue absorption	Biochemistry
Spatial resolution	frequency dependent 3 – 25 cm	~ 1 mm	~ 1 mm	~ 1 mm
Penetration	Very good	Excellent	Excellent	Excellent
Safety	\$	Ionizing radiation	Ionizing radiation	Very good
cost	Excellent	Good	Poor	Poor
Portability	≤ 10 ms	~ 1 min	≥ 1 min	≤ 0.1 s
Speed				

Table 1.1: Comparison of imaging modalities [Sza04].

deliver a high frame rate, which helps to obtain a real-time imaging of the moving organs as in echocardiography. In addition, US is non-ionizing, unlike computed tomography (CT) and X-ray, and harmless to the human body (see Table 1.1). All the cited advantages have placed the US imaging in the top of used imaging techniques in the medical diagnosis phase.

Despite all the previously cited advantages, US imaging cannot compete with most of the other medical imaging modalities in terms of image quality, where the resolution represents one of the most important criteria. The resolution represents the ability of the imaging system to distinguish fine details. One can see in Table 1.1 that the spatial resolution of US images is frequency dependant. Thus, one of the intuitive appropriate methods to improve resolution is increasing the frequency. Hence, with such an approach, another limitation occurs, related to the depth of US wave penetration. Due to the physics of US, the penetration of US waves in the medium decreases with the increase of the frequency. Nevertheless, the use of high frequencies ultrasound is particularly adapted to applications such as skin or eye imaging. However, the use of such high frequencies induces a number of instrumentation-related technological challenges. In particular, building probes performing at high frequencies is an ongoing challenge in this field.

1.2 Physics of Ultrasound

1.2.1 Piezoelectric elements and transducers

Generating US waves and collecting US echoes is performed using US transducers (probe). The latter consists of one or a series of piezoelectric elements. These elements work using the double piezoelectric effect (direct and inverse) discovered experimentally by Pierre Curie and his brother Jacques in 1880. This detailed piezoelectric effect is as follows (see Figure 1.1):

- The direct piezoelectric effect: by applying mechanical constraints, the piezoelectric elements transform the mechanical waves into voltage.
- The inverse piezoelectric effect: by applying a voltage, the piezoelectric crystal produces mechanical deformation.

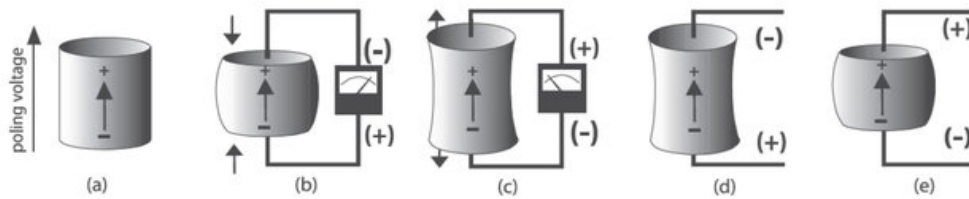


Figure 1.1: (a-c) Direct , (d-e) inverse piezoelectric effect [MF06].

Thus, in practice, a voltage is applied to the transducer's piezoelectric elements to generate US waves that propagate through the medium. After interacting with the tissues, the echoes return to the transducer, where its piezoelectric sensors transform the received vibration into a voltage that will be processed afterward to form the US image. Most commercial US transducers are formed by tens or hundreds of piezoelectric elements arranged in a linear or curvilinear array (see Figure 1.2). A detailed description of the types of the transducers and their acquisition schemes will be presented in the Section. 1.3.2. The elements (elementary transducers) are characterized by width in the lateral direction and height in the elevation direction. The Kerf is the spacing between elements, and pitch is the distance between the centers of two consecutive elements. The crystal elements used widely in

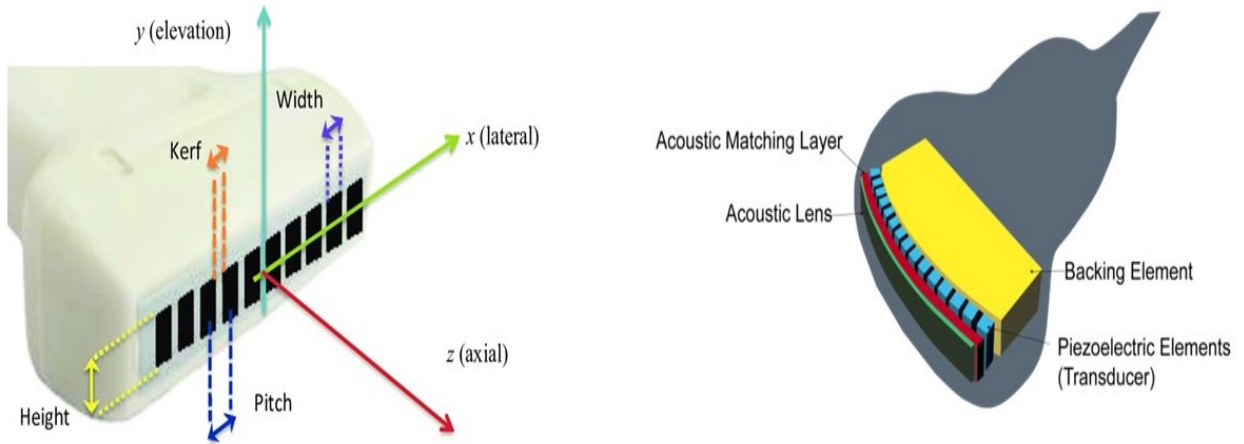


Figure 1.2: US probe linear array on the left, curvilinear array on the right [Tou14].

the US probes nowadays are the lead zirconate titanate (PZT) due to its high conversion ratio. The frequency range is between 1 and 50 MHz for most clinical applications. The choice of the transducer specifications relies on the application.

1.2.2 Ultrasound wave propagation

1.2.3 Linear propagation

US waves carry the information from the imaged medium to the imaging system. During propagation, the US waves interact with the medium yielding different physical phenomena: reflection, scattering, and attenuation. In this section, the US wave propagation is described under the hypothesis of linear propagation. In order to build the propagation equation, two linearized Euler's equations describing the conservation of the mass and the motion are considered in a homogeneous medium with no viscosity and heat conversion [HB88]:

- Conservation of mass:

$$\frac{\partial \rho}{\partial t} + \rho \operatorname{div}(\vec{v}) = 0. \quad (1.2)$$

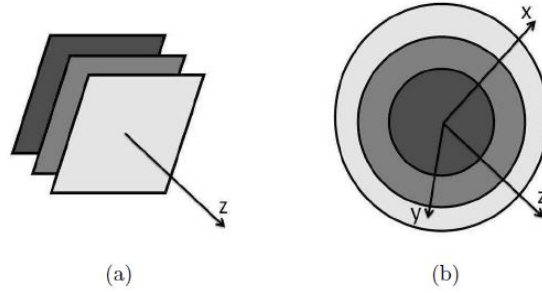


Figure 1.3: (a) Plane wave and (b) Spherical wave [Mor13].

- Conservation of momentum

$$\rho_0 \frac{\partial \vec{u}}{\partial t} + \nabla p = 0. \quad (1.3)$$

where \vec{u} represents the particle velocity, ∇ and $div(\cdot)$ represent the gradient and the divergence operator respectively. The equation (1.2) considers that no mass loss or gain occur during propagation. Based on the Newton's second law, the equation (1.3) relates the perturbation of the medium to external forces. Thus, by applying the divergence operator on the equation (1.3) and the time derivative on the equation (1.2) we obtain the Helmholtz equation [Bey74]:

$$\frac{1}{c^2} \frac{\partial^2 p}{\partial t^2} - \nabla^2 p = 0, \quad (1.4)$$

where ∇^2 refers to the Laplacian operator defined as follows:

$$\nabla^2 = \frac{\partial^2}{\partial x^2} + \frac{\partial^2}{\partial y^2} + \frac{\partial^2}{\partial z^2}. \quad (1.5)$$

The analytical solution of the equation (1.4) depends on the geometry of the US waves. The US waves are considered as spherical or plane waves. The corresponding wavefronts (i.e. the phase surfaces during propagation) are shown in Figure 1.3.

While propagation, the thermal conductivity is relatively low. Thus, the compression is considered adiabatic and can be expressed as follows:

$$\frac{p}{p_0} = \left(\frac{\rho}{\rho_0} \right)^\gamma, \quad (1.6)$$

where γ refers to the ratio of specific heat. p_0 and ρ_0 represent the pressure and density at equilibrium. The US propagation is considered isentropic (there is no net transfer of heat or matter), and therefore, for a constant entropy s , the speed of propagation can be written as:

$$c^2 = \left(\frac{\partial p}{\partial \rho} \right)_s \quad (1.7)$$

Using (1.6) and (1.7), the relation between the speed of the propagation of US waves, the initial transmitted pressure and the density of the medium can be expressed as follows:

$$c_0^2 = \gamma \frac{p_0}{\rho_0}. \quad (1.8)$$

1.2.4 Nonlinear propagation

The propagation of US waves was assumed linear in the previous section. However, in medical applications, the US propagation is in fact a nonlinear process. In this case, the equation (1.3) should consider a propagation in a non viscous and lossless medium and therefore becoming [HB88]:

$$\rho \left(\frac{\partial \vec{u}}{\partial t} + (\vec{u} \cdot \nabla) \vec{u} \right) + \nabla p = 0 \quad (1.9)$$

In (1.9), the term $(\vec{u} \cdot \nabla) \vec{u}$ represents the consecutive acceleration that has been introduced to (1.3). This added term makes the propagation a nonlinear process. This section presents the nonlinear parameter that expresses the level of non linearity in the medium, the distortion effect, and the nonlinear propagation equation.

1.2.4.1 Nonlinear parameter

During the propagation process, the US waves are distorted due to the nonlinear interaction with the medium. A nonlinear parameter was deducted to quantify the level of this non-linearity. The equation (1.6) is valid for gases and does not present the relation between the pressure and the density. Therefore, a Taylor expansion is applied on the pressure in order to express its evolution as a function of the density [FW54, Bey60]:

$$p = p_0 + \left(\frac{\partial p}{\partial \rho} \right)_s (\rho - \rho_0) + \frac{1}{2!} \left(\frac{\partial^2 p}{\partial \rho^2} \right)_s (\rho - \rho_0)^2 + \dots \quad (1.10)$$

Considering $p' = p - p_0$ and $\rho' = \rho - \rho_0$, (1.10) can be written as follows:

$$p' = A \frac{\rho'}{\rho_0} + \frac{1}{2!} B \left(\frac{\rho'}{\rho_0} \right)^2 + \dots, \quad (1.11)$$

with the parameter A and B expressed as:

$$\begin{cases} A = \rho_0 \left(\frac{\partial p}{\partial \rho} \right)_s \equiv \rho_0 c_0^2 \\ B = \rho_0^2 \left(\frac{\partial^2 p}{\partial \rho^2} \right)_s \end{cases} \quad (1.12)$$

Considering only A , the relation between the density and the wave pressure is linear and the propagation is considered linear. However, by also considering B , the relation between density and wave pressure becomes nonlinear. The nonlinear parameter is thus defined as the ratio between B and A . B can be re-written as follows:

$$B = \rho_0^2 \left(\frac{\partial^2 p}{\partial \rho^2} \right)_{\rho=\rho_0} = \rho_0^2 \left(\frac{\partial}{\partial \rho} \left(\frac{\partial p}{\partial \rho} \right) \right)_{\rho=\rho_0} = \rho_0^2 \left(\frac{\partial c^2}{\partial \rho} \right)_{\rho=\rho_0} = 2c\rho_0^2 \left(\frac{\partial c}{\partial \rho} \right)_{\rho=\rho_0} = 2\rho_0^2 c_0^3 \left(\frac{\partial c}{\partial p} \right)_{\rho=\rho_0}. \quad (1.13)$$

Hereby, the nonlinear parameter (the ratio between the quadratic, B , and the linear, A , coefficient of the Taylor development) can be expressed as follows:

$$\frac{B}{A} = 2\rho_0 c_0 \left(\frac{\partial c}{\partial p} \right)_{\rho=\rho_0}, \quad (1.14)$$

In the literature, a nonlinear coefficient β is used for standardization and simplification reasons and is expressed as follows:

$$\beta = 1 + \frac{B}{2A} \quad (1.15)$$

1.2.4.2 Wave distortion

The nonlinear parameter has a direct impact on the velocity of the pressure wave:

$$c = c_0 \left(1 + \frac{B}{2A} \frac{u}{c_0} \right)^{\frac{2A}{B} + 1} \quad (1.16)$$

Because the ratio between the particle velocity and the u/c_0 is small, the speed of propagation is usually simplified by:

$$c = c_0 + \left(1 + \frac{B}{2A} \right) u = c_0 + \beta u \quad (1.17)$$

Using the expression of the particle velocity, the speed of propagation in (1.17) can be further expressed as:

$$c = c_0 + \beta \frac{p}{\rho_0 c_0} \quad (1.18)$$

Therefore, the speed of sound variation Δc can then be expressed as a function of the pressure variation Δp :

$$\Delta c = c - c_0 = \frac{\beta}{\rho_0 c_0} \Delta p \quad (1.19)$$

However, in the particular case of the ultrasound propagation, the mean pressure value is null and the variation is the same of the pressure value ($\Delta p = p$). The maximum and minimum of the speed of propagation, respectively c^+ and c^- , are then expressed in two successive phase as follows:

- Compression: The pressure variation is positive and the velocity of the wave in the medium is greater than c_0 :

$$c^+ = c_0 + \Delta c = c_0 + \frac{B}{2A} \frac{p}{\rho_0 c_0} \quad (1.20)$$

- Dilatation case: where the variation of pressure is negative and the velocity of the wave is less than c_0 :

$$c^- = c_0 - \Delta c = c_0 - \frac{B}{2A} \frac{p}{\rho_0 c_0} \quad (1.21)$$

Thus, (1.20) and (1.21) demonstrate that in the compression phase, the US waves travel faster than the dilatation phases (lower pressure wave). Thereby, in the presence of nonlinearity, a distortion phenomenon takes place and harmonics appear in the spectrum of the signal. These harmonics translate the nonlinear behavior of the wave propagation (see Figure 1.4). The higher the nonlinear coefficient, the faster the distortion. In theory, the distortion is amplified during propagation until the pressure wave becomes a sawtooth at a shock distance z_{sh} [MMGZ05, RS77]:

$$z_{sh} = \frac{\rho_0 c_0^3}{\omega_0 \beta p_0} \quad (1.22)$$

Due to the frequency dependant attenuation, it is hard to reach this shock distance in the case of medical imaging, especially when the energy of initial wave pressure is low. However, we can see in (1.22) that the nonlinear process is not only linked to the nonlinear coefficient but also to the

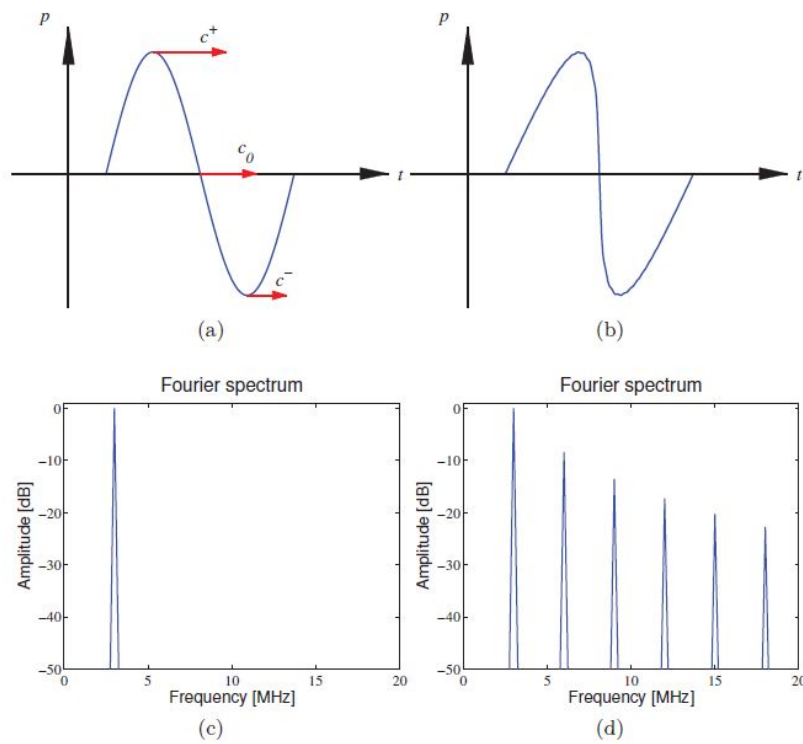


Figure 1.4: Distortion of US waves due to nonlinearity: (a) Sinusoidal pressure wave transmitted at $z = 0$ and (b) after $z = 500$ mm . In the Fourier spectrum, (c) the harmonics are initially not visible and appear in (d) due to wave distortion. The illustration has been obtained for a 3 MHz wave with an initial pressure of 100 kPa after 500 mm of propagation in water ($B/A = 5$) [Var11].

frequency. Indeed, the nonlinear process can be fastly developed by increasing the frequency of the initial wave. However, due to the frequency dependant dissipation, the higher frequencies (harmonics) are more attenuated than the fundamental one. This makes hard to reach the shock distance easily in the medium.

1.2.4.3 Nonlinear propagation equation

The nonlinear wave propagation has been largely described in the literature [HB88, HB⁺98]. One of the first equations describing the nonlinear propagation was the Burger's equation [Bey74]. In medical imaging, the finite size of the elementary transducer elements has to be taken into consideration. The Burger's equation does not consider the source diffraction. Therefore, the KZK equation, developed by Kuznetsov, Zabolotskaya and Khokhlov [Zab69, ABTT84], had upgraded the Burger's equation by adding the term considering the diffraction effect related to the source. The upgraded equation is expressed as follows:

$$\frac{\partial p}{\partial z} = \Delta_{\perp} p + \frac{D}{2c_0^3} \frac{\partial^2 p}{\partial \tau^2} + \frac{\beta p}{\rho_0 c_0^3} \frac{\partial p}{\partial \tau} \quad (1.23)$$

where Δ_{\perp} represents the diffraction's effect of the transducer. In medical imaging, the geometric dimension of medical probes defines the diffraction in the KZK equation. For example, for linear arrays, the diffraction element Δ_{\perp} is expressed as follows:

$$\Delta_{\perp} p = \int_{-\infty}^{\tau} \left(\frac{\partial^2 p}{\partial x^2} + \frac{\partial^2 p}{\partial y^2} \right) d\tau', \quad (1.24)$$

where (x, y) are the lateral and elevation dimensions in the probe plane, and τ' is the integration variable to the delayed time τ .

1.2.5 Reflection and transmission

The US waves are reflected or transmitted on the boundaries between two media with different acoustic impedance Z (expressed in $Kg.m^{-2}.s^{-1}$ or Rayleigh) like in geometrical optics with:

$$Z = \rho \times c, \quad (1.25)$$

where c is the speed of sound in the medium.

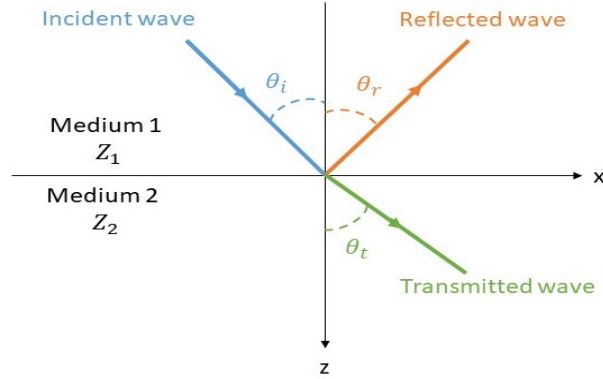


Figure 1.5: Reflection and transmission on the boundaries of two regions.

Different classical values of acoustic impedance, speed of sound and density are presented in Table 1.2. Based on the Snell law, the difference of impedance between two regions in the medium creates an interface where the incident pressure waves are divided into reflected and transmitted waves (see Figure 1.5). This phenomenon plays a major role in the definition of the interface and the characteristics of the medium at the end of the process in the US image.

The amplitude of the two transmitted and reflected waves depends on the incident angle θ_i and on the acoustic impedance of the two media. The intensity of reflection and transmitted wave are defined by the reflection coefficient R and transmission coefficient T :

$$\begin{cases} R = \frac{(Z_2 \cos(\theta_i) - Z_1 \cos(\theta_t))^2}{(Z_2 \cos(\theta_i) + Z_1 \cos(\theta_t))^2} \\ T = 1 - R = \frac{4Z_1 Z_2 \cos(\theta_i) \cos(\theta_t)}{(Z_2 \cos(\theta_i) + Z_1 \cos(\theta_t))^2} \end{cases} \quad (1.26)$$

Under normal incidence (*i.e.*, $\theta_i = 0$), the coefficient of reflection depends mainly on the difference of impedance between the two regions and the formulation of R and T are simplified to:

$$\begin{cases} R_0 = \frac{(Z_2 - Z_1)^2}{(Z_2 + Z_1)^2} \\ T_0 = \frac{4Z_1 Z_2}{(Z_2 + Z_1)^2} \end{cases} \quad (1.27)$$

Medium	Density kg/m ³	Speed of sound m/s	Characteristic acoustic impedance kg/m ² · s
Air	1.2	333	0.4×10^3
Blood	1.06×10^3	1566	1.66×10^8
Bone	$1.38 - 1.81 \times 10^3$	2070 – 5350	$3.75 - 7.38 \times 10^6$
Brain	1.03×10^3	1505 – 1612	$1.55 - 1.66 \times 10^6$
Fat	0.92×10^3	1446	1.33×10^8
Kidney	1.04×10^3	1567	1.62×10^8
Lung	0.40×10^3	650	0.26×10^6
Liver	1.06×10^3	1566	1.66×10^8
Muscle	1.07×10^3	1542 – 1626	$1.65 - 1.74 \times 10^6$
Spleen	1.06×10^3	1566	1.66×10^8
Distilled water	1.00×10^3	1480	1.48×10^8

Table 1.2: Acoustical characteristics for some materials [Sza04]

For example, in the case of imaging skull, the difference between the acoustical impedance of the bone of the skull and the gel added in the intermediate region between the transducer and the skin is relatively high. This leads to high reflection coefficient. This makes the imaging of brain a hard task to accomplish using US imaging. However, another type of reflection depending on the size of the imaged particles can occur during propagation, namely the scattering, explained hereafter.

1.2.6 Scattering

A scattering effect occurs when US waves interact with a target whose size is much smaller than the wavelength of the incident waves (see Figure 1.6). In this case, the Snell law does not hold anymore, and the results of this type of interaction are spherical waves going in all the directions called back-scattered waves. The targets are called scatterers. This scattering phenomenon is the origin of the speckle noise in the US images (further detailed in the Section 1.3.5). Furthermore, tissues are often

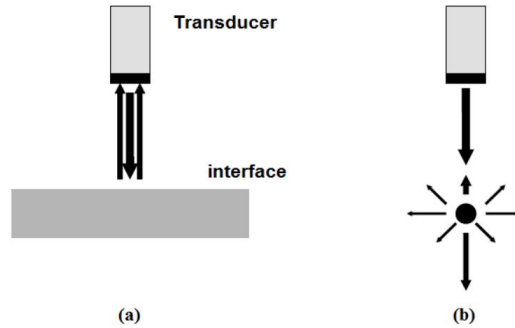


Figure 1.6: (a) Specular (mirror effect) and (b) scattering [Kou].

modeled as set of scatterers. Thus, in low-frequency US imaging, the scattering is more likely to appear since the wavelengths are long.

1.2.7 Attenuation and penetration

The intensity of ultrasound waves experiences loss as they travel through tissues. This loss is referred to as 'attenuation'. The penetration is defined by the maximum depth that the ultrasonic waves can reach in the imaged tissues. The attenuation is mainly caused by absorption and diffraction. Considering a forward plane wave, the local pressure can be expressed as follows:

$$p(z, t) = A(z)s(t - z/c), \quad (1.28)$$

where $s(t - z/c)$ is the wave emitted by the probe along the axial depth z , and t is the propagation time. In the ideal case, in the absence of attenuation, $A(z) = A_0$, where A_0 is the original amplitude of the US emitted wave at $z = 0$. Yet, typical tissues concerned by ultrasound imaging exhibit attenuation, thus $A(z)$ depends on z -position and the amplitude decay can be expressed as follows:

$$A(z) = A_0 e^{-\alpha_L z}, \quad (1.29)$$

where α_L is the amplitude attenuation coefficient expressed in $Nepers.cm^{-1}$ and written as follows:

$$\alpha_L = \frac{1}{z} \times \ln\left(\frac{A_0}{A(z)}\right). \quad (1.30)$$

Medium	Attenuation at 1 MHz $dB.cm^{-1}$	$\alpha(f)/\beta$
Air	12	f^2
Water at 20°C	0.0022	f^2
Blood	0.18	$f^{1.3}$
Brain	0.85	f
Fat tissues	0.63	$\approx f$
Lung	41	$1/f$

Table 1.3: Attenuation coefficient for different type of tissues [Sza04]

Hereby, the attenuation coefficient, in $dB.m^{-1}$, is expressed as follows:

$$\alpha = 20 \log_{10}(e) \alpha_L \approx 8.69 \alpha_L. \quad (1.31)$$

The latter coefficient is related to the frequency of the US waves by the following equation:

$$\alpha(f) = \beta f^m, \quad (1.32)$$

where m is a number between 1 and 2 for biological tissues. Therefore, one may observe that the attenuation is not only depth dependant but also frequency dependant. In other words, the higher the frequency of the US pulse, the lower will be the penetration depth. Table. 1.3 presents the attenuation in different biological medium.

1.3 Ultrasound image formation

1.3.1 Imaging principle

Within US imaging, the US transducer is placed against the skin with a gel placed in between the skin and the probe in order to decrease the attenuation due to the propagation of US waves in the air. Then, the transducer sends US waves, and records the echoes that are afterwards used to construct the US image through series of processing techniques. Finally, the image is presented on the machine display (see Figure 1.7).

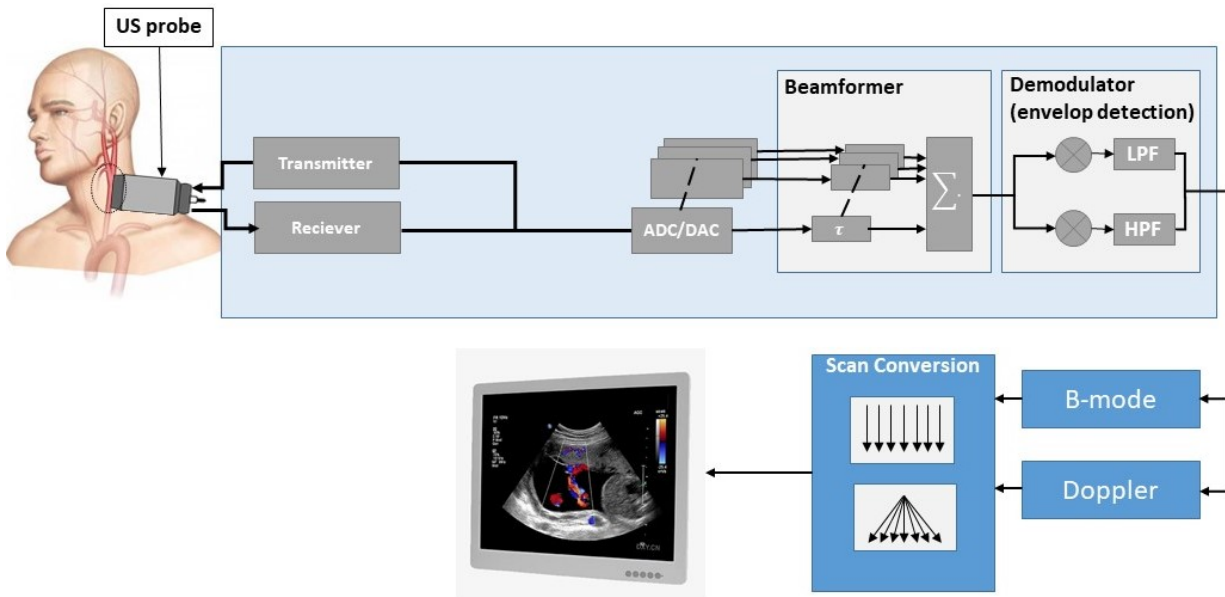


Figure 1.7: Block diagram of US imaging process.

1.3.2 Beamforming to RF image

The acquisition scheme in US imaging is fundamentally related to the transducer configuration. Two main schemes exist in application: the sector and the rectangular schemes.

Rectangular scans are obtained using a linear transducer (see Figure 1.8(b)). Within a linear transducer, the piezoelectric elements are arranged in line. This type of transducers is used, for example, in imaging of the carotid, thyroid or cysts in the liver.

Sector scans are obtained either using a convex or a phased array transducer. In the case of the convex transducer the elementary transducers are placed in a convex form. The resulted field of view (FOV) is then polar cross-sectional and are larger than the rectangular transducers (see Figure 1.8 (a)).

In the phased array, all the elementary transducer are used in the same time in transmission and reception. A delay is applied to the elements in order to control the direction of the beam. The phased array enable to have a large FOV with a small array. The phased array was revolutionary in the heart imaging where a small transducer is needed to image between the ribs and having a

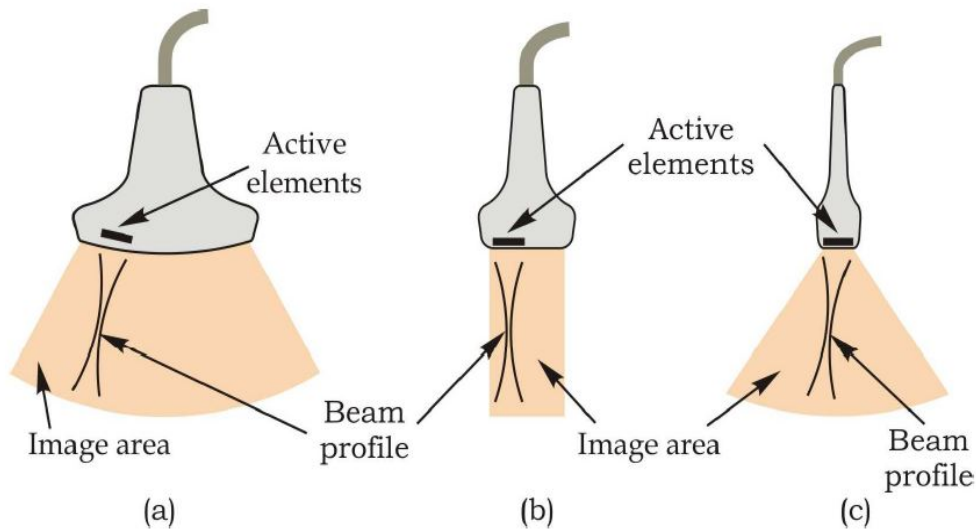


Figure 1.8: (a) Convex array transducer, (b) Linear array transducer, (c) Phased array transducer [Sza16].

controllable and large FOV (see Figure 1.8(c)). Beamforming plays a crucial role in US image formation, heavily influencing the characteristics of the final image. The standard way of beamforming is to delay and weight the reflected echoes before averaging them. A sub-part of transducer elements (called aperture) are activated in the transmission phase. Then, in reception, the US probe collects the back-scattered waves and transforms them into electrical signals. In the classical methods, the same aperture is used in emission and reception. Each active transducer of the aperture records an electric signal called radio frequency (RF) signal. All the received signals are delayed and summed in order to compensate the delays due to the time-of-flight differences and build hereafter the RF line. This procedure is repeated by shifting the activated zone (aperture) all along the transducer surface in order to build the different RF lines of the image. This technique is called delay and sum (DAS) and is most commonly used and represents the conventional US beamforming (see Figure 1.9). The set of beamforming delays defines the steering angle and focal distance of the transmitted and received beams. In the last decades, a breakthrough in the domain of the beamforming had

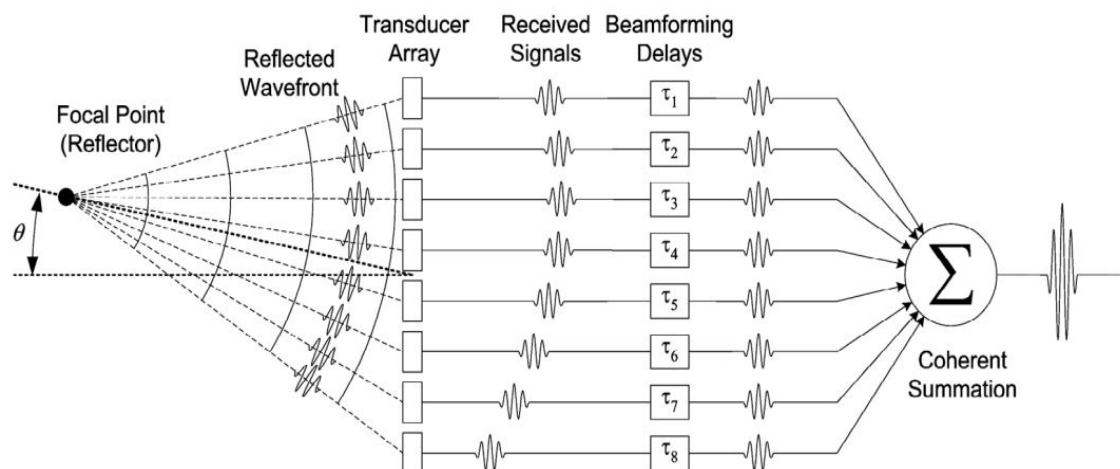


Figure 1.9: Delay-and-sum beamforming in a phased array ultrasound imaging system [JKKY05].

existed through several modern beamforming techniques. The latter techniques had accelerated the advances in the fast imaging techniques and improved the quality of the images. These methods will be detailed in the Chapter 2.

1.3.3 US image modes

After receiving the US waves, there are several methods to visualize the received echoes depending on the application. Here we present the different modes of the US images applied to presents the US image.

1.3.3.1 A-mode

A-mode refers to amplitude mode. This mode represents an historical application of ultrasound. The envelope of the received signal is built and presented in function of time. Based on the receiving time, and knowing the speed of the sound of in the medium, the depth of each interface can be precisely estimated (see Figure 1.10). This visualization mode was used to reveal brain tumors and nowadays is widely applied in ophtalmologic applications in which a precise measurements of the inside of the eyes are needed.

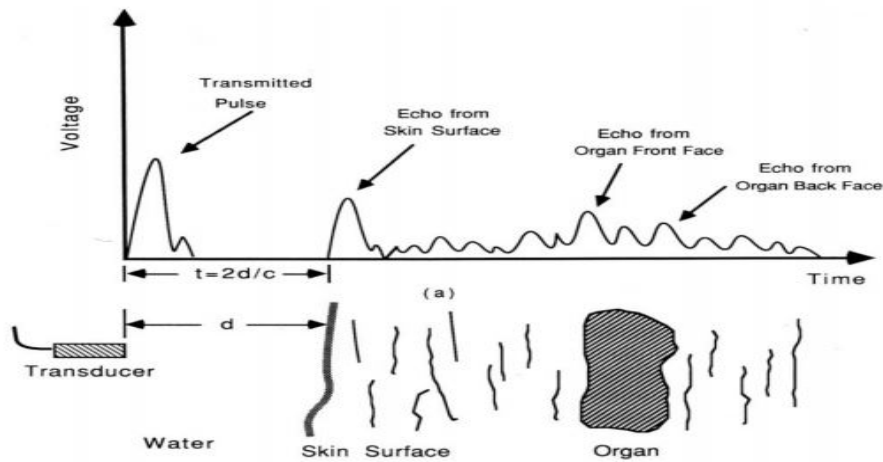


Figure 1.10: A-mode graph [PL06].

1.3.3.2 M-mode

M-mode refers to motion mode (also called also TM-mode refers to time motion mode). This mode consists on the juxtaposition of the same scan line (A-mode) in order to form 2D images through time in order to detect the motion of active organs. The results are presented as an intensity in a brightness mode on the y-axis and the time on the x-axis. This technique is highly applied in the emergency department, in order to visualize the movement of the heart or a specific valve inside the heart. For example in Figure 1.11 (b), one can follow the motion of the heart valves with respects to time in parallel with the EEG signal presented in the bottom of the image.

1.3.3.3 B-mode

The US B-mode (B stands for brightness) images are 2D displays of echo signal amplitudes. In order to form the 2D image, the active aperture of the transducer is moved according to the lateral axis x where the beam is directed in the axial direction z . One RF line represents one column of the 2D image. The RF lines are juxtaposed in order to build the 2D RF image, also called RF image. The interpretation of RF image is visually difficult. Thus, a demodulation step should be applied. This demodulation can be done using the envelope detection techniques such as Hilbert transform

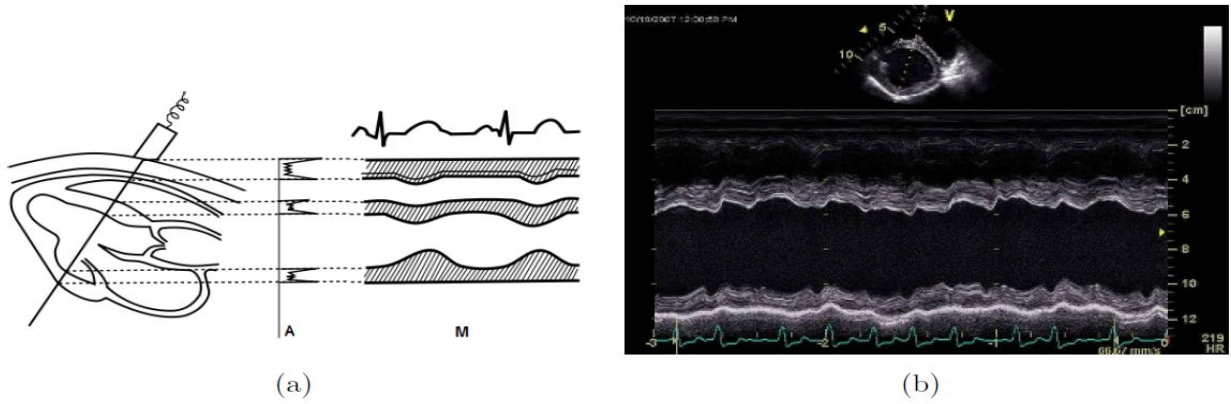


Figure 1.11: (a) Scheme for obtaining the M-Mode, (b) an M-Mode example in cardiac imaging [Sza04]

followed by a logarithmic compression. The latter compression reduces the dynamic of the image from 120 to 60 dB to suit the human vision. The detailed representation of envelope detection and logarithmic compression is illustrated in Figure 1.12.

1.3.3.4 Doppler Mode

Another important application of US in medical applications is the Doppler effect. It consists of the estimation of the blood flow velocity and its direction (see Figure 1.13). The frequency of the emitted US waves f_0 is shifted lower or higher as the US waves are reflected by blood. Therefore, the transducer receives US waves with a different central frequency, and the frequency shift Δf , so called Doppler shift, is expressed as follows:

$$\Delta f = \frac{2f_0 v \cos(\theta)}{c}, \quad (1.33)$$

where c is the velocity of US waves, θ is the angle between the wave front direction and the target velocity direction, and v is the velocity of the blood flow.

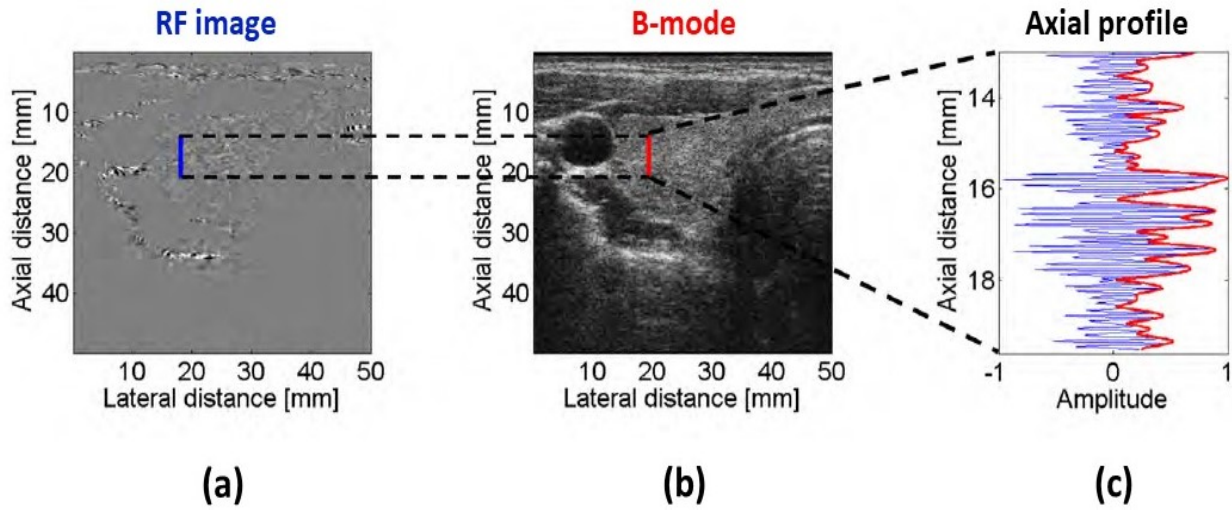


Figure 1.12: Relationship between RF and B-mode image for a thyroid image [Bas08]. (a) RF image, (b) B-Mode image, (c) an extraction of axial profile, RF signal in blue and corresponding envelope in red

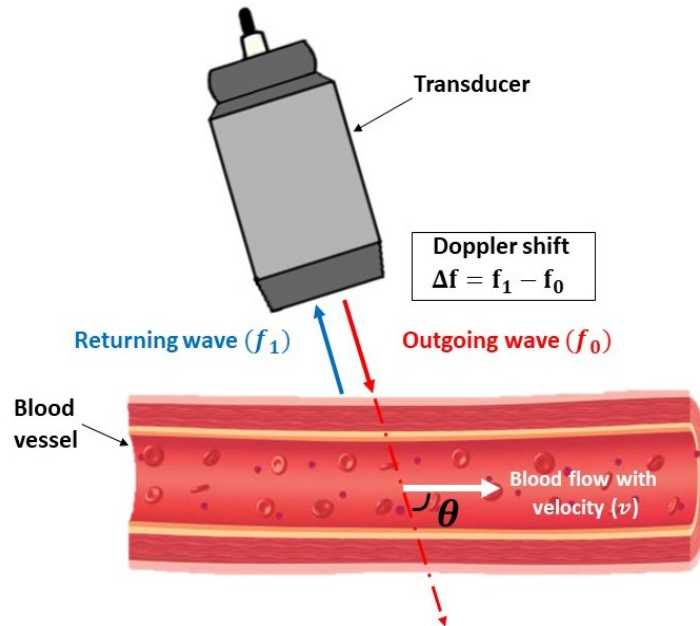


Figure 1.13: Doppler effect application in medical US imaging.

1.3.4 Spatial resolution

The imaging system is characterized by the spatial resolution. The spatial resolution is the ability of the imaging system to differentiate and highlight two closed structures in the imaged field. The spatial resolution includes three type of resolutions: axial, lateral and azimuthal resolutions.

1.3.4.1 Axial resolution

Axial resolution is the capability of the imaging system to differentiate two close structures located in the axial direction of the US beams (z-direction). The axial resolution depends on the number of cycles of the transmitted signal, in other words it depends on the US frequency and the bandwidth. The axial resolution r_{ax} can be expressed as follows [Jen07]:

$$r_{ax} = \lambda \frac{M}{2}, \quad (1.34)$$

where M is the number of cycles of the transmitted signal. Since the axial resolution is frequency-dependent, it can be improved by increasing the frequency of US waves and thus decreasing the length of the transmitted pulse. This technique is applied in US high frequency imaging (see Figure 1.14). However, the attenuation is frequency dependant, thus by increasing the frequency, the penetration of the US waves decreases. In practice, for central frequencies of 5 Mhz and with 3 cycles of the transmitted signal, the axial resolution is about 0.2 mm.

1.3.4.2 Lateral resolution

The lateral resolution is the ability of the system to distinguish and display two close structures that lie in the plane perpendicular to the ultrasound beam direction. Lateral resolution depends on the geometry (i.e, on wavelength λ , and focal distance, L_f), and it depends on the inverse of the diameter of the active transducer, D [Jen96]:

$$r_{lat} = \lambda \frac{L_f}{D}. \quad (1.35)$$

The lateral resolution is maximum in the focal point were the beam is the thinner (see Figure 1.15). Thus, the thinner the beam, the better the lateral resolution. Therefore there exist two ways to improve lateral resolution. First, lateral resolution can be improved using beamforming techniques

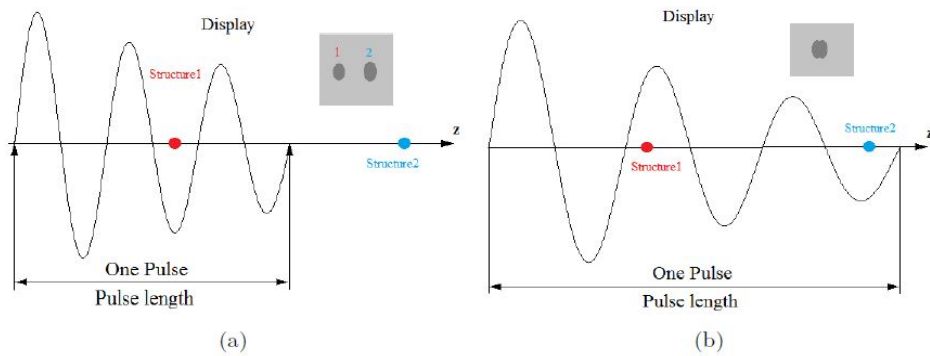


Figure 1.14: (a) A high frequency wave with a short pulse length, (b) A low frequency wave with a long pulse length [Che16]

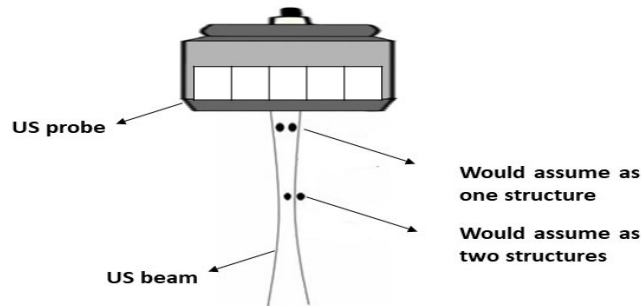


Figure 1.15: lateral resolution in US imaging.

in order to adjust the focal point in the region of interest dynamically. Second, the lateral resolution can be improved by increasing the frequency and improving the geometry of the transducer. For example, in practice, the lateral resolution goes from 1.01 to 0.64 mm by increasing the frequency from 3 MHz to 5 MHz.

1.3.4.3 Azimuthal resolution

Azimuthal resolution (so called elevational resolution) represents the extent to which an ultrasound system is able to resolve objects within an axis perpendicular to the plane formed by the axial and lateral dimensions. The elevational axis represents the 'thickness' of the beam itself. The beam height

depends on the height of the individual piezoelectric transducer elements (i.e. on the geometry of the transducer elements).

1.3.5 Speckle

US imaging is characterized by a granular texture called speckle, which indirectly carries information on the structure of the medium but greatly affects the contrast and boundary of objects of interest such as organs or cysts. The scattering detailed before, is the origin of the speckle noise. Depending on the location of other scatterers in the medium, the scattered ultrasound waves may either undergo constructive or destructive interference depending on the phase of the waves when they interact. This results in a granular texture made of light and dark areas in the formed image. The distribution of speckle can be used in speckle tracking and tissue characterization.

1.4 Open challenges

As presented in this introductory chapter, US imaging presents several advantages: effectiveness, low cost, non-invasiveness. Thus, US imaging is one of the most used techniques in medical imaging. However, several drawbacks appear in the quality of US images. US images present, in contrast with other imaging modalities, a low signal-to-noise ratio. The main reasons behind the latter issue are: firstly, the presence of speckle, secondly, the use of short pulses in time, which makes the broadband spectrum in the frequency domain more affected by multiple noise sources. On the other hand, the resolution enhancement of the US images is one of the main challenges in US applications. However, two trade-offs between resolution\contrast and resolution\penetration should be considered through the enhancement process. In order to increase contrast, the transmit and receive bandwidths must be narrowed, which reduces resolution. The penetration of ultrasound signals can be improved by reducing their frequency, which consequently occurs a degradation in the resolution of US images. Therefore, many studies proposed several methods in order to enhance the US image resolution taking into consideration the trade-offs previously cited. These studies can be classified into two main categories: pre-processing and post-processing techniques. The thesis

proposes a post-processing method applied jointly on two US image modalities with the goal to enhance resolution, while preserving a good contrast and overcome the attenuation in depth.

1.4.1 Organization of the manuscript:

The remaining of the thesis consists of 3 chapters.

- **Chapter 2:** This chapter presents, as exhaustive as possible, the US image modelling from the US propagation equation. In the following, the state-of-art of the pre-processing techniques (modern beamforming techniques, harmonic imaging and pulse inversion) and post-processing methods (filtering and deconvolution) applied for US image enhancement is presented. The orientation of this thesis by adopting the post-processing approach, more precisely the deconvolution, is justified at the end of the chapter.

Main contributions:

- **Chapter 3:** Based on the advantages of both image restoration and the harmonic image in Chapter 2, this chapter introduces a new approach of joint deconvolution of fundamental and harmonic images. We presented a slightly different harmonic image model than the fundamental one by considering an attenuation matrix in depth of the harmonic image. The joint deconvolution problem is solved in the ADMM framework. The advantage of joint deconvolution was presented on simulation data [HBK⁺18, HBKT19a, HBKT19b]. Encouraged by the latter results, this approach is applied on deeper scale by considering real data images which consist a bigger challenge of the proposed methods [HBKT21]. This chapter follows the trend of deconvolution with pre-estimated PSF where the PSF is estimated in a first step before the restoration process. In this chapter, we present the entirety of the results on real and simulation data and prove the interest of the proposed approach.
- **Chapter 4:** This chapter considers an upgrade of the restoration method presented in Chapter 3. The contribution in this chapter is twofold: Firstly, an fully blind joint deconvolution solution

is presented in order to estimate the PSF simultaneously with the restoration process. Results are presented on phantom and real data [HBM⁺20]. In the second part of this chapter, we present a solution considering the spatial variability of the PSF all along the axial direction of the image. This solution considers a smooth interpolation (depth-dependant) of different restored image on different depth with the corresponding PSF [HBV⁺20]. Results on real data are presented and compared to the results presented in the Chapter 2 where the PSF was considered spatially invariant all along the image.

List of publications

International Journal papers

1. M. Hourani, A. Basarab, D. Kouamé and J. -Y. Tournernet, **Ultrasound Image Deconvolution Using Fundamental and Harmonic Images**, in *IEEE Transactions on Ultrasonics, Ferroelectrics, and Frequency Control*, vol. 68, no. 4, pp. 993-1006, April 2021

Conference papers

1. M. Hourani, A. Basarab, D. Kouamé, J.-M. Girault and J.-Y. Tournernet, **Restoration of Ultrasonic Images using Non-linear System Identification and Deconvolution**, in *Proc. IEEE Int. Symp. Biomed. Imaging (ISBI)*, Washington, USA, Apr. 2018.
2. M. Hourani, A. Basarab, D. Kouamé, and J.-Y. Tournernet, **Tissue Reflectivity Function Restoration from Fundamental and Harmonic Ultrasound Images**, in *Workshop on Signal Processing with Adaptive Sparse Structured Representations (SPARS 2019)*, Toulouse, France, Jul. 2019.
3. M. Hourani, A. Basarab, D. Kouamé, and J.-Y. Tournernet, **Joint Deconvolution of Fundamental and Harmonic Ultrasound Images**, in *Proc. IEEE Int. Ultrason. Symp. (IUS)*, Glasgow, UK, Oct. 2019.
4. M. Hourani, A. Basarab, O. Michailovich, G. Matrone, A. Ramalli, D. Kouamé, and J.-Y. Tournernet, **Blind Deconvolution of Fundamental and Harmonic Ultrasound Images**,

- in *Proc. IEEE Int. Symp. Biomed. Imaging (ISBI)*, Iowa city, USA, Apr. 2020.
5. M. Hourani, A. Basarab, F. Varray, D. Kouamé and J. -Y. Tournieret, **Block-Wise Ultrasound Image Deconvolution from Fundamental and Harmonic Images**, in *IEEE International Ultrasonics Symposium (IUS)*, 2020, pp. 1-4,

CHAPTER 2

Stat-of-art : Ultrasound image restoration

Contents

3.1	Introduction	64
3.2	US image formation models	65
3.3	Problem reformulation	66
3.4	Optimization	67
3.4.1	Basics of the Alternating Direction Method of Multipliers	67
3.4.2	Proposed ADMM parametrization	68
3.4.3	Implementation details	69
3.5	PSF estimation	71
3.6	Data and evaluation metrics	73
3.6.1	Data simulation and acquisition	73
3.6.1.1	Synthetic data	73
3.6.1.2	Experimental images	74
3.6.2	Spectral analysis of the experimental data	76
3.6.3	Quantitative metrics	78
3.7	Results and discussion	79
3.7.1	Results on synthetic data	80
3.7.1.1	Supervised approach	80
3.7.1.2	Joint deconvolution with pre-estimated PSF approach	84
3.7.2	Results on phantom and real images	89
3.7.2.1	Phantom image	89
3.7.2.2	Carotid results	92
3.8	Discussion	95
3.9	Conclusion and perspectives	98

2.1 Introduction

As presented in the previous chapter, the US images suffer from different drawbacks related to the physics of ultrasound, and instrumentation. In addition, the usefulness of US depends partly on the skills of the technician performing the examination. Thus, the reproduction of the same images is hard and depends on human skills. All the cited drawbacks have presented a challenge to researchers in order to enhance or restore the US images.

A lot of research and advances have been made during the last decades to improve the US image quality through several goals: removing the speckle (despeckling), enhancing the resolution, improving the contrast, denoising, increasing the penetration and the frame rate. In medical US imaging, the image enhancement can be done: 1) during acquisition, and in this case, the methods are titled as pre-processing methods, or 2) after the acquisition, and the methods in this case are classified as post-processing methods.

This chapter will present the state-of-art of enhancement methods and is organized as follows: firstly, the US image model is shown. Secondly, the pre-processing methods are presented, and thirdly, the state-of-art of post-processing methods applied on US images are discussed in detail.

2.2 US image formation model

Several methods were introduced in literature to solve the linear and non-linear US propagation equation starting from the full-wave non-linear equation and model hereafter the US image. The partial differential equation (PDE) was solved in the time domain using finite difference methods [TTC11, PDRT09] and in the Fourier domain using spectral methods such as the angular spectrum method [TTC11, PDRT09].

In the case of linear propagation, [Tup69, P. 71] present an ultrasound imaging model based on the spatial impulse response approach. In the absence of any scattering targets, the medium is considered uniform with density ρ_0 and adiabatic compressibility κ_0 . In this case the speed of propagation c_0 can be written as follows:

$$c_0 = \frac{1}{\sqrt{\rho_0 \kappa_0}} \quad (2.1)$$

In the presence of inhomogeneity, the scatterers can be modeled by adding spatially dependent terms $\Delta\rho$ and $\Delta\kappa$ to the density and the compressibility respectively. The total pressure field $p(\mathbf{r}, t)$ at time t and position \mathbf{r} can be expressed in the following partial differential equation (PDE) [GL77]:

$$\nabla^2 p(\mathbf{r}, t) - \frac{1}{c_0^2} \cdot \frac{\partial^2 p}{\partial t^2}(\mathbf{r}, t) = \frac{1}{c_0^2} \cdot \frac{\partial^2 p}{\partial t^2}(\mathbf{r}, t) \gamma(\mathbf{r}) + \nabla \cdot [\mu(\mathbf{r}) \nabla p(\mathbf{r}, t)] \quad (2.2)$$

The scattering terms $\gamma(\mathbf{r})$ and $\mu(\mathbf{r})$ represent the monopole and the dipole radiation (see [AT00] for detailed definition) and expressed as follows:

$$\gamma(\mathbf{r}) \equiv \frac{\Delta\kappa(\mathbf{r})}{\kappa_0}, \quad \mu(\mathbf{r}) \equiv \frac{\Delta\rho(\mathbf{r})}{\rho_0 + \Delta\rho(\mathbf{r})} \quad (2.3)$$

The solution of (2.2) is not straightforward. Many ways exist in the literature to solve it. For better clarity, we recall here the method presented by [NPK+06]. The full linear propagation equation in (2.2) is expressed by the PDE in the Fourier domain as follows [GL77, MI86] :

$$\nabla^2 P(\mathbf{r}, \omega) + \left(\frac{\omega}{c_0}\right)^2 P(\mathbf{r}, \omega) = -(\mathcal{S}P)(\mathbf{r}, \omega) \quad (2.4)$$

where \mathbf{r} represents an arbitrary position in scattering volume. $P(\mathbf{r}, \omega)$, the solution of the PDE, is the total pressure in the field, c_0 is the sound velocity in the medium at equilibrium and \mathcal{S} is the scattering operator that depends to the variation of the compressibility $\gamma(\mathbf{r})$ and the variation density $\mu(\mathbf{r})$ as well. \mathcal{S} can be defined:

$$\mathcal{S} \equiv \gamma(\mathbf{r}) \left(\frac{\omega}{c_0}\right)^2 - \nabla \cdot \mu(\mathbf{r}) \nabla. \quad (2.5)$$

The PDE (2.4) is linear and homogeneous. However, it can be considered as inhomogeneous equation by considering the right term in (2.4) as the source of scattered pressure waves [GL77]. In this case, the PDE denotes an homogeneous solution and particular solution. The homogeneous solution, $P_i(\mathbf{r}, \omega)$, is the incident pressure when the scattering term is set to zero. $P_s(\mathbf{r}, \omega)$ is the particular solution representing the scattered pressure field. Therefore, thanks to the linearity of (2.4), the total pressure field can be expressed as the sum of the incident pressure field transmitted by the probe and the scattered field produced by the interaction with the scatterers and can be expressed as follows:

$$P(\mathbf{r}, \omega) = P_i(\mathbf{r}, \omega) + P_s(\mathbf{r}, \omega) \quad (2.6)$$

2.2.1 Incident pressure

The incident field is generated from the US transducer. The coordinate of the system are presented in Figure 2.1, where \mathcal{A} is a surface bounding the transmit and receive subapertures, \mathbf{r}_0 is the location of the center of \mathcal{A} , \mathbf{r}_a is an arbitrary point on \mathcal{A} , \mathcal{V} is a volume within which the scatterers being considered are contained and \mathbf{r}' is an arbitrary point in \mathcal{V} . The surface \mathcal{A} is made up of infinitesimally small area elements $d^2\mathbf{r}_a$. Each of this elements contributes as a simple point source mounted on a rigid baffle. A perception of the sound field for a fixed time instance can be obtained by employing Huygens' principle in which every point on the surface \mathcal{A} is the origin of an outgoing spherical wave. Further, the aperture \mathcal{A} is assumed flat, so no re-radiation from scattering and reflection takes place. Thus, the incident pressure field is expressed as the Rayleigh integral [Jen91]:

$$P_i(\mathbf{r}, \mathbf{r}_0, \omega) = \frac{\rho_0}{2\pi} \int_{\mathcal{A}} j\omega V(\mathbf{r}_a, \omega) \frac{e^{-j\frac{\omega}{c_0}|\mathbf{r}-\mathbf{r}_0-\mathbf{r}_a|}}{|\mathbf{r}-\mathbf{r}_0-\mathbf{r}_a|} d^2\mathbf{r}_a = j\omega\rho_0 H_t(\mathbf{r}-\mathbf{r}_0, \omega), \quad (2.7)$$

where

$$H_t(\mathbf{r}, \omega) \equiv \int_{\mathcal{A}} V(\mathbf{r}_a, \omega) \frac{e^{-j\frac{\omega}{c_0}|\mathbf{r}-\mathbf{r}_a|}}{2\pi|\mathbf{r}-\mathbf{r}_a|} d^2\mathbf{r}_a \quad (2.8)$$

refers to as the spatial transmit transfer function that accounts entirely for the spatial distribution of the incident pressure field and incorporates the effects of apodization and focusing. $V(\mathbf{r}_a, \omega)$ is the temporal Fourier transform of the normal velocity on the transmit subaperture's surface \mathcal{A} .

2.2.2 Scattered pressure field

In order to calculate the scattered pressure field, the Helmholtz equation (2.4) is solved using the Green function method where the scattering term is replaced by a point source as follows:

$$\nabla^2 G(\mathbf{r}, \mathbf{r}', \omega) + \left(\frac{\omega}{c_0}\right)^2 G(\mathbf{r}, \mathbf{r}', \omega) = \delta(\mathbf{r}-\mathbf{r}') \quad (2.9)$$

where $G(\mathbf{r}, \mathbf{r}', \omega)$, the Green function, is the solution of (2.9) and represents the pressure field in the presence of a point source centred at \mathbf{r}' . The scattered waves from the volume \mathcal{V} are considered to be propagating into an effectively unbounded medium (*i.e* \mathcal{V} covers all of three-dimensional space) and thus $G(\mathbf{r}, \mathbf{r}', \omega)$ can be expressed as follows:

$$G(\mathbf{r}, \mathbf{r}', \omega) = -\frac{e^{-j\frac{\omega}{c_0}|\mathbf{r}-\mathbf{r}'|}}{4\pi|\mathbf{r}-\mathbf{r}'|} \quad (2.10)$$

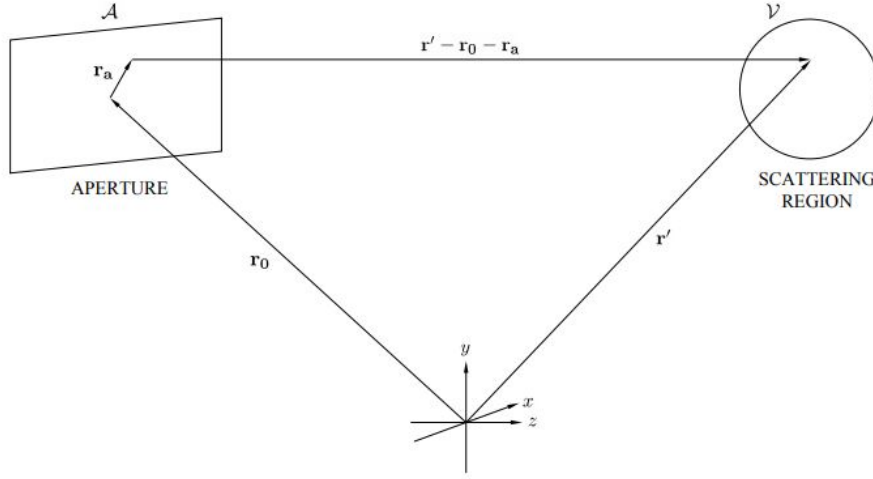


Figure 2.1: Coordinate system of the scattering field [NPK⁺06].

The particular solution to (2.4) is then the product of the right hand side of (2.4) and $G(\mathbf{r}, \mathbf{r}', \omega)$ integrated over the volume \mathcal{V} :

$$P_s(\mathbf{r}, \mathbf{r}_0, \omega) = - \int_{\mathcal{V}} (\mathcal{S}P)(\mathbf{r}', \mathbf{r}_0, \omega) G(\mathbf{r}, \mathbf{r}', \omega) d^3\mathbf{r}' \quad (2.11)$$

Considering a weak scattering, the scattered pressure is negligible in equation (2.6), and the total pressure field becomes equivalent to the incident pressure: $P(\mathbf{r}, \mathbf{r}_0, \omega) \approx P_i(\mathbf{r}, \mathbf{r}_0, \omega)$. Using the equations (2.10) and (2.11), the scattered pressure field can be expressed as follows:

$$P_s(\mathbf{r}, \mathbf{r}_0, \omega) \approx \int_{\mathbb{R}^3} (\mathcal{S}P_i)(\mathbf{r}', \mathbf{r}_0, \omega) \frac{e^{-j\frac{\omega}{c_0}|\mathbf{r}-\mathbf{r}'|}}{4\pi|\mathbf{r}-\mathbf{r}'|} d^3\mathbf{r}' \quad (2.12)$$

(2.12) represents the scattering field as a convolution between the incident pressure and the spherical wave $\frac{1}{4\pi|\mathbf{r}|} \exp\left(-j\frac{\omega}{c_0}|\mathbf{r}|\right)$ which refers to the first Born approximation. The latter approximation considers the multiple scattering (interaction between the scattering of waves of more than one target) as negligible. By replacing the incident pressure in (2.12) by the formula in (2.7), the scattered field is expressed as follows:

$$P_s(\mathbf{r}, \mathbf{r}_0, \omega) \approx j\omega\rho_0 \int_{\mathbb{R}^3} (\mathbf{S}H_t)(\mathbf{r}' - \mathbf{r}_0, \omega) \frac{e^{-j\frac{\omega}{c_0}|\mathbf{r}-\mathbf{r}'|}}{4\pi|\mathbf{r}-\mathbf{r}'|} d^3\mathbf{r}' \quad (2.13)$$

2.2.3 Force on the received aperture

As explained before, the transducer elements receive the scattered echoes, and form the RF trace thanks to the electromechanical properties of the PZT elements. The A-line $R(\mathbf{r}_0, \omega)$ is the summation of the scattered pressure field over the receive subaperture and filtering this sum by the electromechanical response of PZT elements. Therefore, the force exerted on the receive subaperture is expressed as follows:

$$F(\mathbf{r}_0, \omega) = \int_{\mathcal{A}} W(\mathbf{r}_a, \omega) P_s(\mathbf{r}_0 + \mathbf{r}_a, \mathbf{r}_0, \omega) d^2\mathbf{r}_a, \quad (2.14)$$

where $W(\mathbf{r}_a, \omega)$ is the spatio-temporal response of the active aperture on reception and incorporates the effects of apodization and focusing on reception collectively. For convenience, $H_r(\mathbf{r}, \omega)$ is defined as the spatial receive transfer function:

$$H_r(\mathbf{r}, \omega) \equiv \int_{\mathcal{A}} W(\mathbf{r}_a, \omega) \frac{e^{-j\frac{\omega}{c_0}|\mathbf{r}-\mathbf{r}_a|}}{4\pi|\mathbf{r}-\mathbf{r}_a|} d^2\mathbf{r}_a \quad (2.15)$$

By substituting $P_s(\mathbf{r}_0 + \mathbf{r}_a, \mathbf{r}_0, \omega)$ by its expression in (2.12), and replace \mathcal{S} by its expression in (2.5) (see [NPK⁺06] for details) the received force can be expressed as:

$$F(\mathbf{r}_0, \omega) \approx \frac{j\omega^3 \rho_0}{c_0^2} \times \int_{\mathbb{R}^3} H_t(\mathbf{r}' - \mathbf{r}_0, \omega) H_r(\mathbf{r}' - \mathbf{r}_0, \omega) [\gamma(\mathbf{r}') - \mu(\mathbf{r}')] d^3\mathbf{r}' \quad (2.16)$$

2.2.4 RF voltage

In this section, the electromechanical conversion of the received force into a voltage trace is presented. The A-line $R(\mathbf{r}_0, \omega)$ is a measure of the force on the active aperture when it is centred at \mathbf{r}_0 over the surface of the active aperture weighted by the electromechanical transfer function $E_m(\omega)$ and thus the RF voltage trace in the Fourier domain can be expressed as:

$$R(\mathbf{r}_0, \omega) \approx \frac{j\omega^3 \rho_0}{c_0^2} E_m(\omega) \times \int_{\mathbb{R}^3} H_t(\mathbf{r}' - \mathbf{r}_0, \omega) H_r(\mathbf{r}' - \mathbf{r}_0, \omega) [\gamma(\mathbf{r}') - \mu(\mathbf{r}')] d^3\mathbf{r}'. \quad (2.17)$$

For representation, we can express the RF voltage trace as the Fredholm integral of the first kind:

$$R(\mathbf{r}_0, \omega) \approx \int_{\mathbb{R}^3} H_{pe}(\mathbf{r}' - \mathbf{r}_0, \omega) f(\mathbf{r}') d^3\mathbf{r}' \quad (2.18)$$

where $f(r)$ represents the reflectivity function (scatterer field). $H_{pe}(\mathbf{r}, \omega)$ is the pulse echo kernel containing the pulse echo wavelet $V_{pe}(\omega)$, receive and transmit transfer function. The voltage trace can thus be expressed as follows:

$$R(\mathbf{r}_0, \omega) \approx V_{pe}(\omega) H_t(-\mathbf{r}, \omega) H_r(-\mathbf{r}, \omega) \otimes f(\mathbf{r})|_{\mathbf{r}=\mathbf{r}_0}, \quad (2.19)$$

where

$$\begin{aligned} H_{pe}(\mathbf{r}, \omega) &\equiv V_{pe}(\omega) H_t(\mathbf{r}, \omega) H_r(\mathbf{r}, \omega), \\ V_{pe}(\omega) &= j\omega^3 E_m(\omega), \\ f(\mathbf{r}) &\equiv \frac{\rho_0}{2c_0^2} [\gamma(\mathbf{r}) - \mu(\mathbf{r})], \end{aligned} \quad (2.20)$$

The voltage trace in (2.18) can be expressed in the time domain as follows:

$$r(\mathbf{r}_0, t) \equiv \frac{1}{2\pi} \int_{-\infty}^{\infty} R(\mathbf{r}_0, \omega) e^{j\omega t} dt \approx \int_{\mathbb{R}^3} h_{pe}(\mathbf{r}' - \mathbf{r}_0, t) f(\mathbf{r}') d^3\mathbf{r}' \quad (2.21)$$

where the pulse echo integral kernel $h_{pe}(\mathbf{r}, t)$ is given by:

$$h_{pe}(\mathbf{r}, t) \equiv \frac{1}{2\pi} \int_{-\infty}^{\infty} H_{pe}(\mathbf{r}, \omega) e^{j\omega t} dt = v_{pe}(t) *_t h_t(\mathbf{r}, t) *_t h_r(\mathbf{r}, t) \quad (2.22)$$

where v_{pe} represents the pulse-echo electromechanical impulse response, $h_{pe}(\mathbf{r}, t)$ the pulse-echo spatial impulse response representing the point spread function (PSF) of the system and $f(\mathbf{r})$ the inhomogeneity in the field due to the presence of scatterers so called the tissue reflectivity function (TRF).

2.2.5 2D image model

We align the coordinates of the system with x, y and z in a way that the aperture surface relies in the xy plan, and thus the position vector \mathbf{r}_0 is expressed as $(x_0, y_0, 0)$ and \mathbf{r}' is written as (x, y, z) . The equation (2.21) can be written as:

$$r(x_0, y_0, t) \approx \iiint h_{pe}(x - x_0, y - y_0, z, t) f(x, y, z) dx dy dz \quad (2.23)$$

This equation presents the tissue reflectivity function filtered with a linear filter laterally and elevationally shift invariant but axially variant [NPK⁺06]. This description guides to representing the

RF image as a spatial convolution between PSF and the TRF [BD80]. From the image processing perspective, and based on the equation (2.23), the US image can thus be expressed in a linear model as a convolution between the PSF and the scatterer field called tissue reflectivity function (TRF). The TRF represents the information to be restored after mitigating the PSF effect. Further details about the US image model will be presented in Section. 2.4.2.

2.3 Pre-processing techniques

The limits of US imaging detailed previously had led to works devoted to the ultrasound field to compensate for known degradation due to tissue properties. The intuitive approach consists of improving the acquisition set-ups. In the following section we will quickly review the pre-processing approaches.

2.3.1 Modern beamforming techniques

Beamforming techniques have improved in order to generate ultrasound beams whose propagation is less affected by tissue inhomogeneities. These techniques have presented several advances yielding an increase the penetration without remarkable degradation of the resolution and with a reasonable, and sometimes higher frame rate.

2.3.1.1 Dynamic focusing

In the conventional US beamforming techniques, where the focal point is fixed in the transmission and reception phases, the resolution of the image is acceptable in the near fields. Nevertheless, the image loses its resolution in depth and become blurrier due to increased lateral beam bandwidth. In order to increase the depth of penetration and reduce side lobes, a dynamic focusing approach was proposed in the literature. Dynamic focusing can be applied during transmission and/or reception. During the transmission, the dynamic focusing can be done by sending series of pulses, where each pulse focuses on a point in depth. After that, a montage step can be applied where images obtained

with different transmission focal lengths are cut around the focus and mounted together. The main drawback of this technique is that, applying several transmissions leads to decreasing the frame rate. It is worth noting that dynamic focusing can be applied in the reception phase and in this case, the focal length is increased electronically with time. Thus, the focus is applied to different points in the imaging area. Technically, this method can be done offline and does not cause a decrease of the frame rate, and conserves a good lateral resolution [SVE94].

2.3.1.2 Synthetic aperture

Another approach, called synthetic aperture, was proposed in the literature to form high-resolution US images [CKDG80]. This technique was applied firstly in RADAR applications [CM91]. In this case, one transmitter/receiver exists, and the aperture is synthesized by moving the antenna on an airplane or satellite. In ultrasound, the transducer is fixed, and so are its elements. Therefore, the synthetic aperture techniques consist of activating one element of the transducer in transmission and activate all the elements in reception. Each transmission/reception step produces a low resolution image due to the unfocused beam generated during transmission by one element [JNGP06, TNL09]. A dynamic focusing is applied during reception. The resulted image is the mean of the focused low resolution images, which result in a high resolution image (see Figure 2.2). The latter method can improve resolution and frame rate, making it a suitable solution for motion estimation. Even though a dynamic focusing is applied in reception, the resulting image does not present a competitive penetration depth compared to conventional beamforming techniques.

2.3.1.3 Coded transmission and pulse compression

The coded transmission techniques were developed firstly in RADAR applications in order to improve the resolution and the signal-to-noise ratio (SNR) for long-range distances [Sie88]. The coded excitation operates a transmission of long pulses in which a code is embedded. After the reception, the echo signal is filtered by an autocorrelation-based filter to detect and eliminate the code. This process is called decoding or compression. The adaptation of this method in US imaging was intuitive and can be classified into two categories. The first method consists of modulating the phases of the

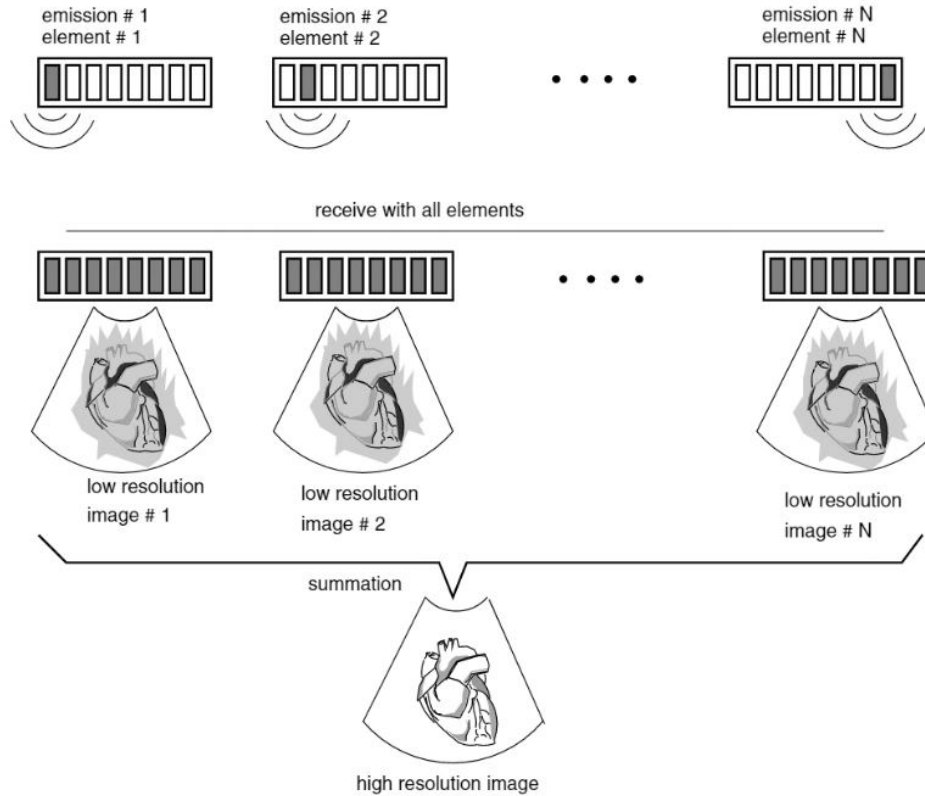


Figure 2.2: Basic principle of synthetic aperture method [Nik02].

excitation with a constant frequency [Tak79, PHL06]. The second method aims to modulate the frequency with a constant phase. In this case, a chirp is sent with ascending or descending frequency. This method had presented since the first applications in the 90's an improvement in the SNR in depth, and consequently, an improvement in the resolution [O'D92, HLT98] without increasing the transmitted pressure. The compression of pulse was applied for a classic probe [MGJ⁺00], intravascular probe [MJR⁺12] and for contrast agent imaging [BCB⁺05]. The main drawback of chirp imaging is the presence of important side lobes that can reach 13 dB [CH05] in the axial direction due to the chirp compression. Hereafter, several methods of filtering and coded excitation have been proposed in order to reduce the level of side lobes and reach -45 dB [HLT98, O'D92, CH05]. One of the most used approaches to reduce the level of side lobes, so-called resolution enhancement compression

(REC) [Oel07], consists of sending two different impulses with different bandwidths and convolving them with two different chirps (see Figure 2.3). The latter method helps to produce an equivalent wave with the ability to increase the bandwidth and consequently improving the resolution while reserving a good depth of penetration.

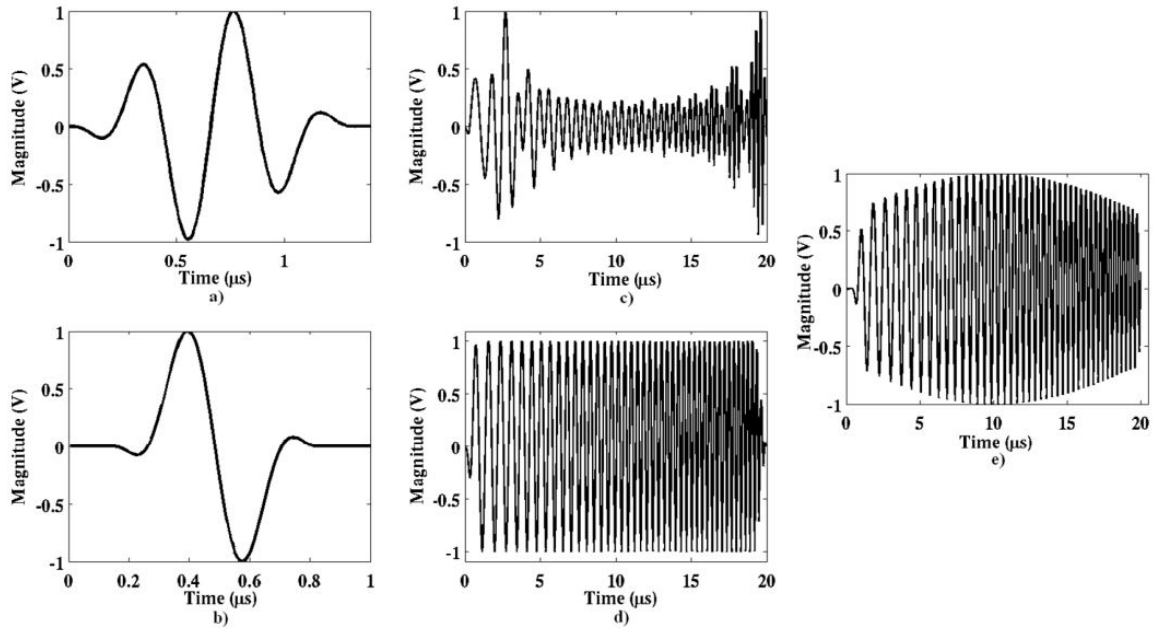


Figure 2.3: Simulated impulse responses, chirps, and convolutions. (a) Pulse with approximately 48 % 3 dB pulse/echo bandwidth. (b) Pulse with approximately 97 % 3 dB pulse/echo bandwidth. (c) Modified chirp used to excite the 48% bandwidth source. (d) Linear chirp used to excite the 97% bandwidth source. (e) Convolution of the pulses with their respective chirps sequences. [Oel07].

2.3.2 Compounding

Compounding methods were investigated in order to reduce the speckle in the US images at the beginning of the 1980s. These methods consist on combining series of images acquired using different angles, apertures, or multiple frequencies. The speckle can be reduced by \sqrt{N} by combining N images where the images are statistically not correlated [Bur78]. However, the reduction of speckle is less than \sqrt{N} where the obtained images are correlated or partially correlated. One can classify

these methods into two categories: Spatial and frequency compounding. The spatial compounding consists of acquiring several images with different angles. The series of images with different angles can be obtained by electronically steering the beam in different angles [TSVR86, OMF10, EPS⁺01]. It can also be done by moving laterally the transducer [VE08]. One can see in Figure 2.4. C and F, where the spatial compounding is applied, reduces speckle patterns in contrast to the conventional US images in Figure 2.4. B and C, respectively. In addition, the spatial compounding method overcomes impressively the acoustic shadowing artifact in the Figure 2.4. The main drawback of these methods is the significant reduction of the frame rate. Thus, in order to overcome the decrease of the frame rate, [BAF03] had proposed the use of three transducer place with different angles, where one of this transducer transmit the pulses, and three of them acquire the echoes. The main drawback of the latter method is the complexity of the application in terms of instrumentation and computation. An alternative practical approach in the same scope is frequency compounding. The latter approach consists of sending different pulses with different frequencies [TASVR86, MvRT82]. Another approach of frequency compounding consists of insonifying the medium with a broadband pulse. Then, the received RF signals are filtered with a bank of narrowband filters and combining the output images of all filters [NBSF82, DC07]. The main motivation of the compounding methods was the reduction of speckle in the US images, so-called despeckling. The improvement of the resolution was a secondary effect. However, in frequency compounding methods, by fixing a bandwidth, a reduction of axial resolution can occur [TASVR86]. Therefore, [DC07] adopts the use of a bank of 2D directive filters based on modified Gabor function. The latter method had proven a speckle reduction with relatively significant resolution enhancement. Another approach had proposed the combination of frequency compounding and REC methods [SO09]. In this case, the frequency compounding uses a larger bandwidth, and the axial resolution was doubled.

The compounding approach affects several characteristics of the image simultaneously (resolution, speckle distribution, etc...). However, in different applications, and especially motion estimation, the speckle distribution is the main parameter on which these methods rely. Thus, an improvement of resolution and contrast without despeckling is needed and will be presented through post-processing techniques that will be presented in the Section 2.4.

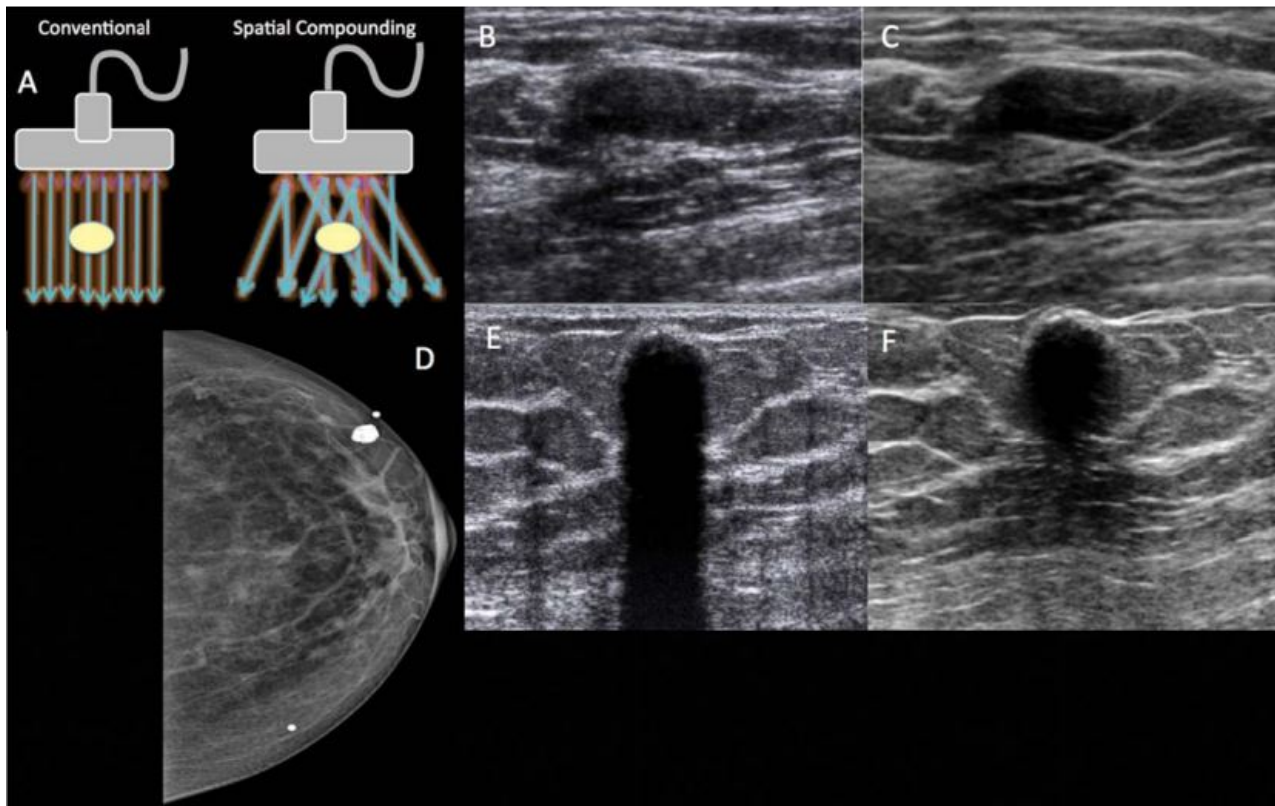


Figure 2.4: Spatial compounding. A, diagram of sound waves transmitted and received at multiple different angles in spatial compounding. B, conventional US image of a mass without spatial compounding. C, US image with spatial compounding of the same mass, which accentuates lesion boundaries and increased lesion conspicuity. D, left breast mammogram in the craniocaudal view showing a popcorn-like calcification in the outer breast. E, correlative conventional US image of the popcorn-like calcification showing posterior acoustic shadowing. F, Ultrasound image of the same calcification with spatial compounding showing complete loss of posterior acoustic features [CHS17].

2.3.3 Harmonic imaging

As previously detailed in Section 1.2.4.2, the US waves occur distortion during propagation. The nonlinear interactions, sources of harmonics in the echo signals, were first observed using contrast agents in the late 90's [Bur96]. For application related to blood perfusion measurements and lesion characterization, US contrast agents (UCA) are injected into the blood circulation, and due to

their high nonlinear coefficient, the energy of the harmonics frequencies in the backscattered waves is important [BCB⁺05, FBK⁺00]. UCA combined with second harmonic imaging and the Doppler technique has presented an improvement in perfusion imaging. The nonlinear interaction of the waves with the tissues themselves can be the origin of the harmonics. In this case, the technique is called tissue harmonic imaging (THI). The THI technique is applied for detecting abdominal disease, breast lesions, and it was validated clinically through different experiments [TGEP99, CGC⁺00, MHEK⁺07]. It is worth mentioning here that a transducer with large bandwidth allows acquiring an echo with spectral information around the fundamental and harmonic frequencies. Different images can be extracted from the same initial RF image:

- Broadband image or raw image where the entire spectrum is used to reconstruct the US image,
- Fundamental image where only the spectrum around the fundamental is used to form the so-called fundamental US image,
- Second harmonic image (named harmonic imaging) which consists of eliminating the spectrum around the fundamental and keeping only the second harmonic (see Figure 2.5)

In medical imaging, the fundamental and the broadband images are quite similar because of the low level of the second harmonic component and the broadband image is usually displayed on commercial scanner.

The classical method to do the separation is by applying a filter to extract the harmonic echoes. However, in broadband excitation, an overlap can occur between the fundamental and the harmonic bands. This could lead to a truncation of wanted information if the optimal parameters of the filter were not properly chosen. Thus, the separation can be done using beamforming techniques such as pulse inversion and phase cancellation (detailed in the next section). It can also be done using post-processing techniques such as system identification [HBK⁺18, PE03b], or linear filtering in the case of narrow band [VBTC13, TJ04].

Comparison of harmonic and fundamental images

Harmonic imaging increases the ability to see some invisible lesions and regions in the image. We present below a comparison between the characteristics of harmonic and fundamental US images:

1. An improvement in the lateral resolution in the harmonic images was remarkable due to the narrowing in the width of the US beam and reducing the side lobes [AFS15] (see Section 1.3.4.2).
2. An improvement in the axial resolution since the wavelength of the harmonic image is less than the fundamental (see Section 1.3.4.1) [TGEP99].
3. Harmonic images have a lower dynamic range than fundamental because the power of the harmonic signal is lower than that of the fundamental one by 10 dB or more [Sza04].
4. Due to the points 1,2,3, the image's contrast is improved, and the boundaries of the organs are better determined.
5. Since the attenuation is frequency dependant (see Section 1.2.7), the US harmonic images undergo a more significant attenuation in contrast with the fundamental image as the pulse propagates through the tissues [WBH97, SBBG86].
6. Harmonic imaging can reduce near field artifact and noise since harmonic waves are not produced in the superficial part. It can reduce other artifacts such as reverberation artifact, side lobes artifact, etc... [MFBS98, BTM⁺98]

Thus, one can see in Figure 2.6, the image of chronic cholecystitis, that the wall of the fallen bladder is better defined in the harmonic image. In addition, the harmonic image presents much more contrast and details.

2.3.4 Pulse inversion

An alternative to filtering, pulse inversion (PI), is one of the pre-processing techniques widely used nowadays [SCB99, SCL05, HUW⁺17]. PI consists of sending successively two pulses out of phase. Adding these two received echoes cancels the fundamental echoes and keeps the harmonic ones. Thus, PI suffers when applied on moving anatomical structures due to the time delay between the

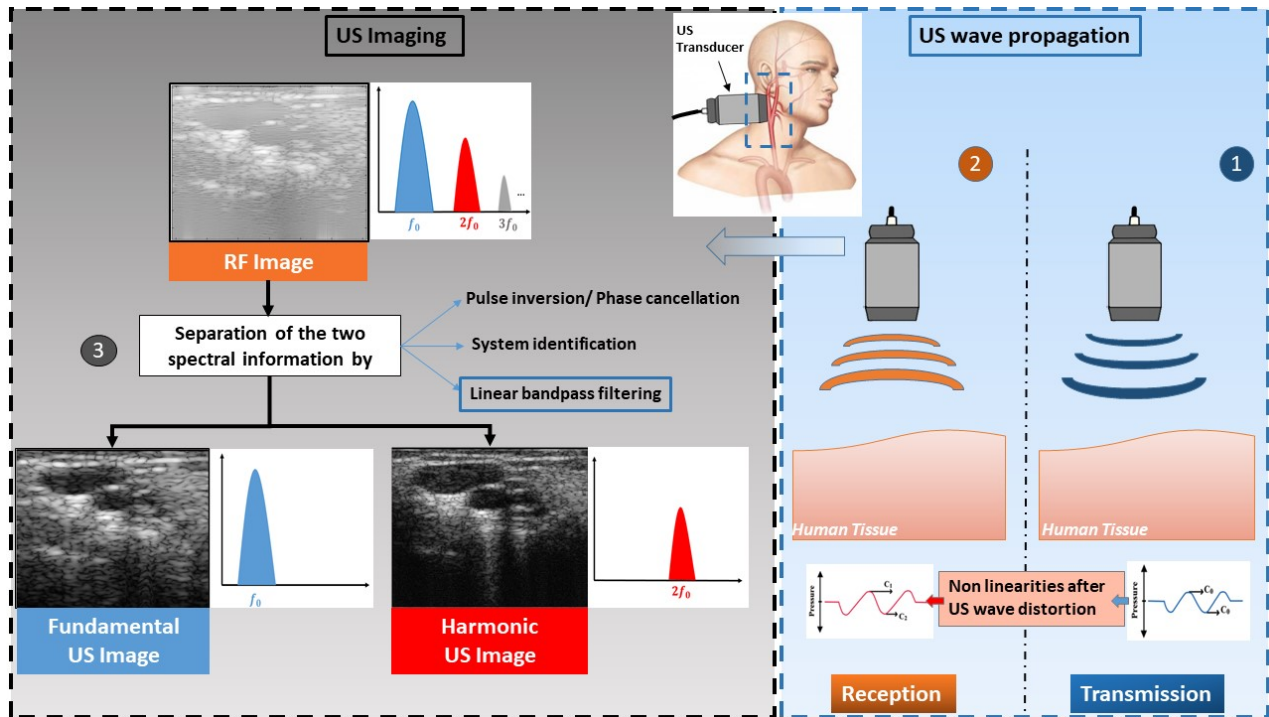


Figure 2.5: Representation of pressure pulse distortion at the origin of harmonic US imaging and examples of fundamental and harmonic US images.

two cycles. Thus, this technique eliminates the side lobes effect of linear filtering in the reconstruction of harmonic imaging.

2.4 Post processing techniques

As discussed previously, pre-processing methods show interesting ability to improve contrast, SNR, resolution, etc... However, their implementations remain complex and lack of flexibility. To overcome these drawbacks, many works have been devoted to post-processing.

2.4.1 Filtering

Two combined types of noise exist in the US images and can be modeled as a multiplicative noise (speckle) and an additive noise (thermal and electronic noise). In the first attempts, the non-adaptive

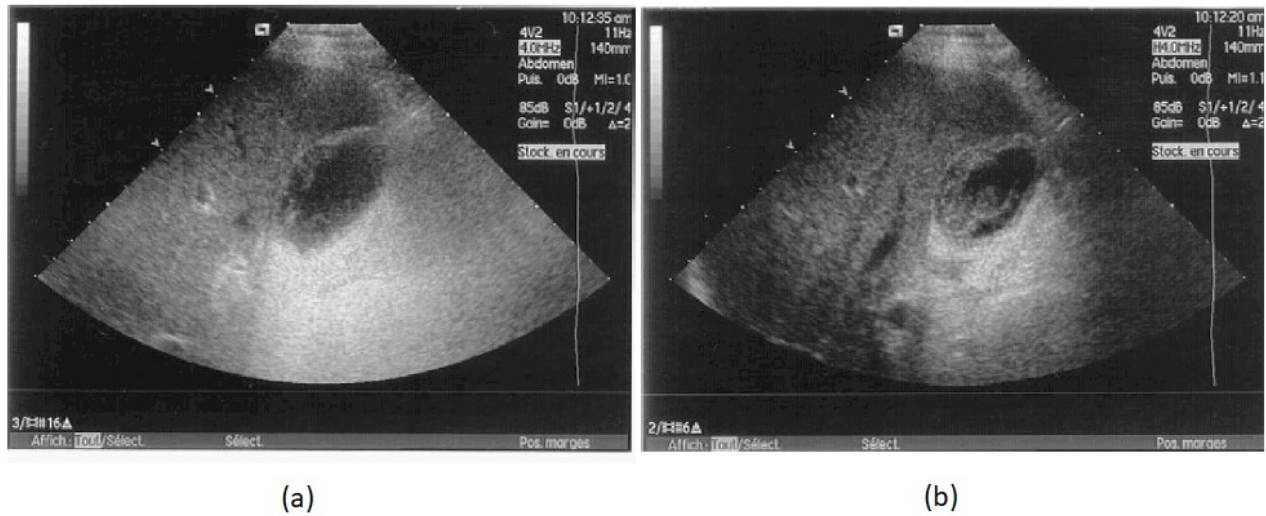


Figure 2.6: Images at (a) the fundamental and (b) second harmonic (bottom) of chronic cholecystitis [TGE99]

filters were presented using median and mean filters. However, the use of the latter filters has introduced a critical blurring effect that reduces the resolution on the edges of the anatomic structures and consequently obstructs the diagnostic process [BD86]. In addition, the statistics of speckle in the imaged medium are heavily dependant on the distribution of scatterers. Thus, the filtering procedure should be more robust and adjustable based on the variation of noise proprieties in the medium. The filtering techniques applied in US imaging can be classified into 3 groups: adaptive filtering, wavelets and, anisotropic diffusion.

Adaptive filters

Adaptive filters are commonly used in image processing to enhance or restore data by removing noise without significantly blurring the structures in the image. The adaptive filters developed in signal processing field were applied, in the 80's, to synthetic aperture radar (SAR) [FSSH82, LTN90]. Those filters were used later on US images [JSF04, Per16]. The adaptive filters rely on identifying regions with fully developed speckle based on a-priori information of speckle statistics. Therefore, the identified homogeneous regions are heavily smoothed using low pass (local mean) filter. The latter

approach was presented in [BD80] using local mean filters and quantitatively applied on cardiac US images in [MLSBG89]. However, the results had presented an increase of the cardiac chambers dimensions and affected the diagnostic values accordingly. Another approach was presented in [CYFB03] in which the presented solution consists of selecting a region size by estimating a homogeneity value for region growth. Then, selected regions are processed with an arithmetic mean filter, and edge pixels are filtered using a nonlinear median filter. Another application of adaptive filters was introduced in [PE03a]. This approach uses second-order Volterra filters in the least-squares approach to generate quadratic images after filtering the quadratic components from the linear components. The filters were applied to UCA images. The coefficients of the filters were estimated based on the contrast ratio between a selected region UCA region and another tissue region. Adaptive filters had presented a better performance than the non-adaptive approach [NLG⁺07].

Wavelet filters

Alternatively, the wavelet filters were applied in the context of noise suppression in US images. The wavelet transform is a method that decomposes a signal into a set of linear combinations of shifted and scaled versions of a mother wavelet. The wavelet filtering consists of setting zero the coefficients representing the noise while preserving the coefficient representing structure in the image and then applying the inverse wavelet transform. The modification of the wavelet coefficients is called wavelet shrinkage. Wavelet shrinkage is effective to reduce additive noise on images. However, in order to filter multiplicative noise, the wavelet shrinkage is applied on the logarithmic transform the image [GOL⁺94]. The latter approach was followed with several attempts in order to choose the optimal threshold level. One can cite [ZLG98], which applied soft thresholding on the logarithmic transformation of the image, followed with a nonlinear contrast stretching and then hard thresholding on the middle scales in order to remove small noise perturbations and preserve the image features. Another approach proposed by [GCS04] consists of modeling the wavelet coefficients in the sub-band as a generalized Gaussian distribution and then estimating the threshold by minimizing the Bayes risk function. On the other hand, [HGG99] proposed to combine adaptive filtering with wavelet approach.

Anisotropic diffusion

The last category of US image filters is anisotropic diffusion filters. Diffusion equation is a partial differential equation that describes particle movement from areas with high concentration to an area with low concentration. Therefore, the noise suppression while identifying edges is controlled by a diffusion coefficient within the differential equation. [PM90] considers that a space-variant filter is, in fact, isotropic but depends on the image content. It approximates an impulse function close to edges and other structures that should be preserved in the image over the different levels of the resulting scale space. Thus, [PM90] introduced a generalization of the partial differential equation, so-called anisotropic equation, where the diffusion coefficient can be a matrix value depending on the image position. The main goal was to preserve edges while smoothing the intra-regions. This method is also called the speckle reducing anisotropic diffusion method (SRAD). This work was followed by several ones considering the anisotropic diffusion in despeckling [YA02, SHTA04, LPC⁺05]. A combination between the anisotropic diffusion and the wavelet filters was proposed in [YCB⁺06] and nowadays presents one of the best candidates applied in cardiac image enhancement applications for example.

Limitations of filtering approaches

The filtering approach induces tuning parameters like the size of the filter or the threshold. These parameters are, in general, defined empirically. Thus, a wrong choice of the latter parameters may lead to erroneous results. In addition, logarithmic compression is applied to the images. Thus the multiplicative noise is assumed to be transformed after logarithmic compression to a Gaussian model or Rayleigh probability density. Therefore, this assumption is considered restrictive in a denoising approach. On the other hand, the filtering approach does not deal with US image artifacts as reverberation and shadowing. Another significant aspect of US image enhancement/restoration is deconvolution and will be presented in the following section.

2.4.2 Deconvolution

Under the first Born approximation, and consequently the assumption of linearity, the US image can be expressed as a convolution between the TRF and the PSF (see (2.26)). The deconvolution is a technique used to improve resolution in US images by counteracting the effect of the PSF. Since the

first proposition of the convolution model of US images [FK80], deconvolution has been widely applied in the US image enhancing. To do so, a linear US image model is adopted based on what was already presented in the Section 2.2. As a result, the US image model can be expressed as a convolution term with an additive white Gaussian noise (AWGN), which mimics the measurement noises. In the following, we will adopt the lexicographic notation of the images, which makes correspond to each matrix \mathbf{X} a vector \mathbf{x} corresponding to the vertical concatenation of the columns of \mathbf{X} . For example, if we note:

$$\mathbf{X} = \begin{bmatrix} x_{1,1} & x_{1,2} & \dots & x_{1,n_2} \\ \vdots & \vdots & & \vdots \\ x_{n_1,1} & x_{n_1,2} & \dots & x_{n_1,n_2} \end{bmatrix} = \begin{bmatrix} \mathbf{x}_1 & \mathbf{x}_2 & \dots & \mathbf{x}_{n_2} \end{bmatrix} \in \mathbb{R}^{n_1 \times n_2} \quad (2.24)$$

the corresponding lexicographical notation is then, with $N = n_1 \times n_2$

$$\mathbf{x} = \begin{bmatrix} \mathbf{x}_1^T & \mathbf{x}_2^T & \dots & \mathbf{x}_{n_2}^T \end{bmatrix}^T \in \mathbb{R}^N \quad (2.25)$$

Therefore, after a lexicographical ordering of the image pixels, the US image model can be written as follows:

$$\mathbf{y} = H\mathbf{x} + \mathbf{n}, \quad (2.26)$$

where $\{\mathbf{y}, \mathbf{x}\} \in \mathbb{R}^N$ represents the lexicographically ordered RF image after acquisition and the TRF image to be restored respectively, $H \in \mathbb{R}^{N \times N}$ is assumed to be Block circulant with circulant block (BCCB) matrix related to the 2D PSF and N is the number of pixels of the image. Although, considering a circular convolution is not mandatory in the model, the BCCB matrices are diagonalized in the Fourier domain, which can be very useful for practical computation. $\mathbf{n} \in \mathbb{R}^N$ is the AWGN with variance of σ^2 . The model in (2.26) was widely applied in the litterature of US deconvolution [Jen92, Ng07, TS01]. Based on the presented model, the deconvolution recovers \mathbf{x} from \mathbf{y} .

2.4.2.1 Point spread function (PSF)

In order to estimate the TRF, knowledge of the PSF is mandatory. If the PSF is not measured experimentally, which is generally the case, the PSF is estimated from the image itself. In addition,

the deconvolution process presents a high sensitivity to the estimated PSF [SPN⁺09]. Here one can define the supervised deconvolution (also called 'non-blind' deconvolution) as the case where the PSF is measured or known. In the case where the PSF is estimated, the deconvolution is called blind deconvolution. The PSF is none other than the response of the US imaging system to a single point object. We mention that the model in (2.26) is intrinsically non-stationary [NPK⁺06]. Indeed the PSF is spatially variant along the imaged medium. The spatial variation of the PSF comes from two main elements: the imaging system and the tissues themselves. The imaging system imposes a variation of the PSF related to the beamforming techniques and, in particular, the focusing and the apodization (see Figure 2.7). The dynamic focusing was introduced in order to reduce the variability of the PSF along the depths. However, even with the reduction of the variability, the PSF can still be considered spatially variant. Since the variation of the PSF is also considered tissue-dependent, one can not ignore the attenuation effect, and as a result, the acoustic pulses not only become smaller in amplitude as they propagate, but they also change shape, as one can see in Figure 2.8. The 2D convolution model may not be valid over the entire image because of the spatially variant PSF. However, [NPK⁺06] presented, starting from US propagation equation, that the PSF is shift variant along the axial direction due to the physical reasons (e.g., attenuation, scattering). This variation is considered in some studies solving the restoration problem of US images [FBKV18a, Mic17]. To further reduce the complexity of the restoration problem, most of the existing studies have addressed the restoration problem by dividing the image into several local regions along the axial direction. In each region, the local PSF is assumed shift-invariant [AV85, NO98, GCC⁺09, CBK16b]. The following sections will consider a spatially invariant and known PSF.

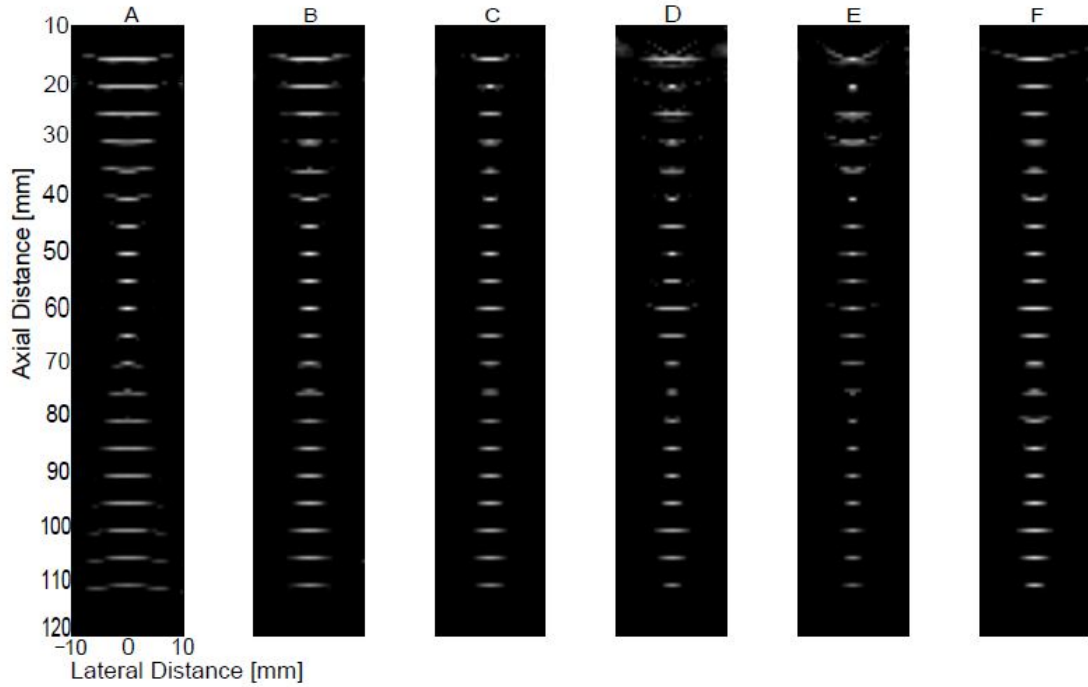


Figure 2.7: Point spread function phantom simulated using the Field II software [Jen53]. Different apodization and focalization are employed in each image.

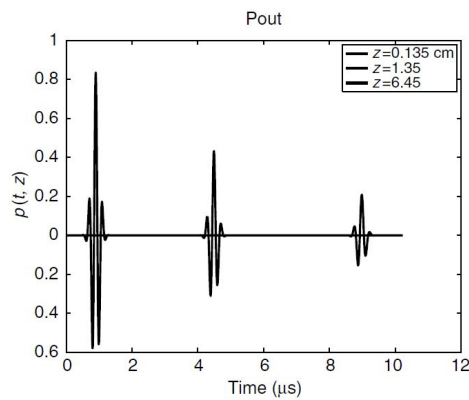


Figure 2.8: Variation in pressure-pulse shape of an initially Gaussian pulse propagating in a medium with a $1dB/MHz^{1.5} - cm$ absorption for three different increasing propagation distances (z) [Sza04].

2.4.2.2 Problem statement

Image deconvolution is often approached as a statistical inference problem. Hereby, the vectors \mathbf{y} , \mathbf{x} and \mathbf{n} are considered as single realizations of random process that follows an appropriate probability density function (PDF). Indeed, in order to estimate \mathbf{x} knowing \mathbf{y} and H , the common solution can be either the maximum likelihood (ML) by maximizing the *log-likelihood* $\log[p(y|x)]$ or by the maximum a Posteriori (MAP) by maximising the *log-posterior* $\log[p(x|y)]$. Assuming that the additive noise follows a Gaussian distribution with a zero mean and variance σ_N^2 :

$$p_n(\mathbf{n}) = \frac{1}{(2\pi\sigma_n^2)^N} \exp\left(-\frac{1}{2\sigma_n^2}\|\mathbf{n}\|_2^2\right), \quad (2.27)$$

and then the likelihood is expressed as follows:

$$p(\mathbf{y} | \mathbf{x}) = p_n(\mathbf{y} - \mathbf{H}\mathbf{x}) = \frac{1}{(2\pi\sigma_n^2)^N} \exp\left(-\frac{1}{2\sigma_n^2}\|\mathbf{y} - \mathbf{H}\mathbf{x}\|_2^2\right). \quad (2.28)$$

Maximizing the likelihood in (2.28) returns to minimizing the data fidelity term $\|\mathbf{y} - \mathbf{H}\mathbf{x}\|_2^2$. The matrix H is ill-conditioned and the simple solution proposed in this case with the pseudo-inverse amplifies the out-of-band noise. This makes the system ill-posed based on the definition of Hadamard that defines the well-posed problem as a problem having three main proprieties: the problem admits a solution, the solution should be unique and the solution changes only with the initial conditions. In order to prevent the ill-posedness, the inverse problem based on the (2.26) can be solved using MAP. In this case, MAP requires a *prior* information $p(x)$, so called the regularization and maximizes the posterior distribution of the TRF defined as:

$$p(\mathbf{x}|\mathbf{y}) \propto p(\mathbf{y}|\mathbf{x})p(\mathbf{x}), \quad (2.29)$$

where \propto means 'proportional to', $p(\mathbf{x})$ is the prior of \mathbf{x} and the likelihood functions $p(\mathbf{y}|\mathbf{x})$ follows the Gaussian distributions:

$$\mathbf{y}|\mathbf{x} \sim \mathcal{N}(\mathbf{H}\mathbf{x}, \sigma^2\mathbf{I}_N) \quad (2.30)$$

where \mathbf{I}_N is the $N \times N$ identity matrix, σ^2 is the noise variance, \mathcal{N} stands for the Gaussian distribution and the additive noise \mathbf{n}_f is assumed to be independent. The negative log-posterior of \mathbf{x} guides to

the estimate of x using MAP as follows:

$$-\log p(\mathbf{r}|\mathbf{y}, \mathbf{y}) \propto \frac{1}{2} \|\mathbf{y} - \mathbf{H}\mathbf{x}\|^2 + \log[p(\mathbf{x})], \quad (2.31)$$

where $p(\mathbf{x})$ represents the prior information about \mathbf{x} . The estimation of TRF can be expressed in the MAP framework as follows:

$$\hat{\mathbf{x}}_{MAP} = \min_{\mathbf{x}} \underbrace{\frac{1}{2} \|\mathbf{y} - \mathbf{H}\mathbf{x}\|^2}_{\text{data fidelity}} + \underbrace{g(\mathbf{x})}_{\text{regularization}}. \quad (2.32)$$

Different type of regularization were proposed and applied in US image deconvolution and will be presented in the following section.

2.4.2.3 Regularizations

- **Gaussian prior** In this case the prior of the TRF \mathbf{x} is considered Gaussian, and the cost function in (2.32) can be expressed as follows:

$$\min_{\mathbf{x}} \frac{1}{2} \|\mathbf{y} - \mathbf{H}\mathbf{x}\|_2^2 + \lambda \|\mathbf{x}\|_2^2, \quad (2.33)$$

where λ represents the regularization parameter which weights the importance between the data fidelity term ($\frac{1}{2} \|\mathbf{y} - \mathbf{H}\mathbf{x}\|_2^2$) and the regularization term $\lambda \|\mathbf{x}\|_2^2$. This problem is well known as Wiener filtering and it was one the first deconvolution techniques applied in US imaging [FK80, RW84, ZWZ98]. Considering a spatially invariant PSF, the matrix \mathbf{H} can be diagonalized in the Fourier domain and the restoration problem can be solved efficiently in the Fourier domain:

$$\hat{\mathbf{x}} = \frac{\mathbf{H}^T}{\mathbf{H}^T \mathbf{H} + \lambda I_N} \mathbf{y} = f(\mathbf{H}, \lambda) \mathbf{y} \quad (2.34)$$

where $f(\mathbf{H}, \lambda)$ represents the Wiener filter which is related to the PSF and the regularization parameter λ . λ can be estimated, or assumed to be the ratio between the squared spectrum of the noise and the squared spectrum of the signal [Tax95, TJ04]. In addition, [CBK15] presents a detailed comparison between several methods of estimation of the regularization parameter applied on simulation data. However, the main shortcoming of this method is Gibbs-like artifacts, which are usually produced by the filter near edge-shaped structures in the TRF \mathbf{x} .

Despite the computational efficiency and due to its linearity, the Wiener filter is not able to interpolate the information lost in the image formation process. Therefore, the Wiener solutions are over smoothed. Finally, the assumption that the reflectivity follows a Gaussian model may be unfair given the complexity of the natural tissues. Therefore, Laplacian prior, widely applied in US image deconvolution, could be an alternative.

- **Laplacian prior**

The prior $p(\mathbf{x})$ is assumed in several applications of US image deconvolution to follow the Laplacian distribution. In this case the regularization terms appears as an ℓ_1 -norm and the optimization problem in (2.32) becomes as follows:

$$\min_{\mathbf{x}} \frac{1}{2} \|\mathbf{y} - \mathbf{H}\mathbf{x}\|_2^2 + \lambda \|\mathbf{x}\|_1 \quad (2.35)$$

The latter convex function is not differentiable, thus the traditional gradient-based algorithms cannot be considered directly [BBV04]. Thus, the solution of the cost function in (2.35) can be solved applying the interior point methods [BTN01]. Yet, in the image deconvolution applications, the large scale of the matrices and theirs high density have lead to quickly discard the latter option because of the complexity of its adaptation to deal with millions of variables. These limitations have motivated the development of gradient descent algorithms, for which the computational cost is relatively cheap and dominated by vector-matrix multiplications involving H and H^T [FNW07]. In this category of first order methods, several algorithms were inspired by the iterative shrinkage (called soft thresholding): the iterative shrinkage-thresholding algorithm (ISTA) [DDDM04], gradient projection method (GSPR) [FNW07], (SPARSA) standing for sparse reconstruction by separable approximation [WNF09]. All the previous methods relies on a soft thresholding step that can be expressed as follows:

$$\mathbf{x}^{(k+1)} = \mathcal{T}_{\lambda t} \left(\mathbf{x}^{(k)} - 2t\mathbf{H}^T \left(\mathbf{H}\mathbf{x}^{(k)} - \mathbf{y} \right) \right), \quad (2.36)$$

where λt is the threshold, and $\mathcal{T}_{\lambda t}$ is the soft thresholding operator that can be expressed in a

scalar fashion as follows:

$$\mathcal{T}_\delta(\mathbf{x})(i) = \frac{x_i}{|x_i|} \max(|x_i| - \delta, 0) \quad (2.37)$$

The origin of the iterative shrinkage-thresholding method can be traced back to the iterative Forward-Backward methods [BJ77, Pas79] that circumvents this difficulty of non-smoothness of the ℓ_1 -norm if data fidelity term in (2.35) (or whatever other function) is differentiable with a Lipschitz-continuous gradient. This scheme consists in performing alternatively a gradient-descent (corresponding to an explicit step on the smooth function) followed by a proximal step (corresponding to an implicit step on the non-smooth function). The latter scheme belongs to the general framework of splitting methods (Chapter 12 in [FP07]) where one can cite another category of splitting methods: the Douglas-Rachford [EB92], *Bregman* method [GO09] that had presented solution to the ℓ_1 minimization. The Bregman iterations belongs to augmented Lagrangian (AL) scheme where the alternating direction method of multipliers (ADMM) [EB92] is widely used nowadays in the convex optimization problems. The split *Bregman* method is equivalent to the ADMM in certain conditions [Ess09]. However, a lot of researches have been established in order to improve and increase the convergence speed of ISTA methods: *two steps* IST (TwIST) in which each iterate depends on the two previous iterates or another fast IST algorithm (FISTA) [BT09] that is a variant of Nesterov's optimal gradient based algorithm for smooth problems [Nes83]. For the sake of completeness, one can also cite the recent methods based on AL scheme: split augmented Lagrangian shrinkage algorithm (SALSA) [ABDF10a], constrained Salsa for constrained problems (C-SALSA) [ABDF10b], and NESTA algorithm [BBC11].

- **Generalized Gaussian distribution**

Besides the traditional prior distribution (Gaussian and Laplacian) of the TRF, the reflectivity functions can be assumed as random sequences of i.i.d. random variables obeying the zero-mean, Generalized Gaussian distribution (GGD). This distribution had been adopted in several works for tissue characterization application [AMP⁺11] and for US image deconvolution [ZBKT14,

ZWB⁺16c, CZBK15]. The GGD PDF can be expressed as follows:

$$p(x_i) = a \exp\left(-\left|\frac{x_i}{b}\right|^p\right) \quad (2.38)$$

where $p > 0$ is the shape parameter, σ_x is the standard deviation, $b = \sigma_x \sqrt{\Gamma(1/p)/\Gamma(3/p)}$ is the scale parameter, $a = p/(2b\Gamma(1/p))$ is the normalization term and $\Gamma(\cdot)$ is the Gamma function. One can notice that with $p = 1$ and $p = 2$, the Laplacian and the Gaussian distribution can be obtained respectively, hence its name as GGD. The cost function is expressed as follows:

$$\min_{\mathbf{x}} \frac{1}{2} \|\mathbf{y} - \mathbf{H}\mathbf{x}\|_2^2 + \lambda \|\mathbf{x}\|_p^p \quad (2.39)$$

Different solutions were proposed in the literature in order to solve the latter ℓ_p regularized problem: iteratively reweighted least square (IRLS) [BT74], approximate message mapping (AMP) [DMM09] for compressed sensing applications, expectation maximization (EM) framework [AMP⁺11], and more recently with the rising popularity of proximal operators, the proximal forward backward (PFB) algorithms [PPC11]. In US restoration, other solutions were presented in the literature in the Bayesian framework [ZBKT14, ZBKT16, CZBK15]. Figure 2.9 presents the application of different norms in the deconvolution of US images.

- **Total variation prior** Indeed, total variation (TV) was widely used as prior for deconvolution problems. Thus, TV does not penalise the discontinuities in the image while imposing smoothness, and resulting a better edge-preserving. The regularization based on TV prior can be expressed as follows:

$$\|\mathbf{x}\|_{\text{TV}} = \sqrt{\|\partial_{\text{h}}\mathbf{x}\|^2 + \|\partial_{\text{v}}\mathbf{x}\|^2} = \sqrt{\|\mathbf{D}_{\text{h}}\mathbf{x}\|^2 + \|\mathbf{D}_{\text{v}}\mathbf{x}\|^2}, \quad (2.40)$$

where ∂_{h} and ∂_{v} correspond to the horizontal and vertical gradients. \mathbf{D}_{h} and \mathbf{D}_{v} are two matrices representing the gradient operator, and equivalent to the horizontal and vertical discrete differences of the image. Thus, the deconvolution problem can be written considering an AWGN noise as follows:

$$\min_{\mathbf{x}} \frac{1}{2} \|\mathbf{y} - \mathbf{H}\mathbf{x}\|_2^2 + \tau \|\mathbf{x}\|_{\text{TV}} \quad (2.41)$$

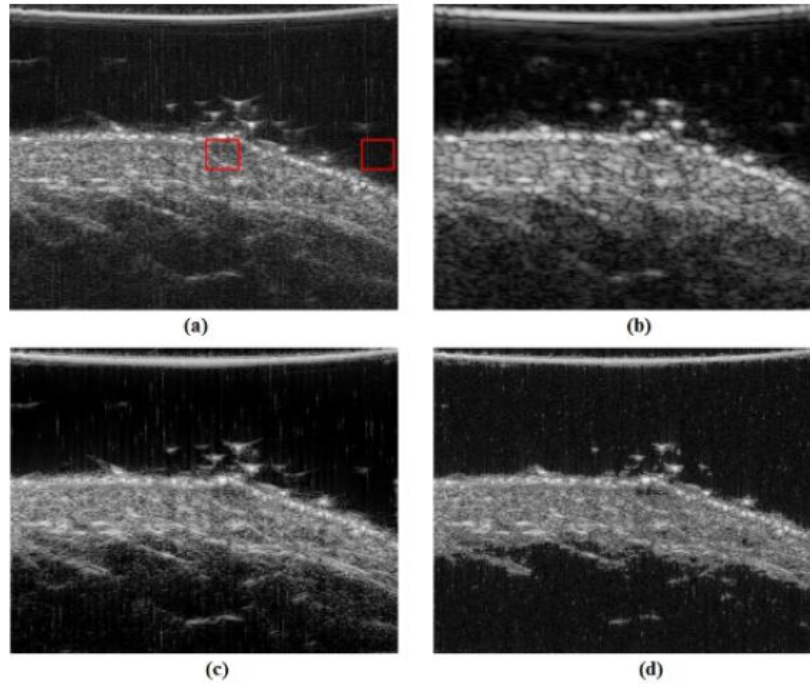


Figure 2.9: (a) Observed B-mode image, (b) restored B-mode images with ℓ_2 -norm, (c) ℓ_1 -norm and (d) ℓ_p -norm (results from [ZBKT16])

Thereby, several optimization algorithms have solved the latter problem such as FISTA [BT09], forward-backward algorithms [FP10], ADMM [ZWB⁺16a]. The application of TV regularization was investigated in [MBK12, MBBK13, NWY10] in a deconvolution and super-resolution applications on US images using ADMM algorithms.

2.5 Blind image deconvolution

The deconvolution solutions presented in the previous sections requires a known PSF. However, in real case, the PSF is rarely measured and an estimation of the PSF is mandatory step in the restoration procedure. Thus, two perspectives were presented in the literature in order to estimate the PSF. The first methods rely on estimating the PSF *a priori*, and followed by one of the 'non-blind' deconvolution approach presented in the previous section. This approach is called sequential

and so-called in the this thesis 'deconvolution with pre-estimated PSF'. The other approach is to estimate simultaneously the PSF and the TRF. The latter approach is called in this thesis: 'fully blind deconvolution'.

2.5.1 Deconvolution with pre-estimated PSF

The first attempts in the sequential approach were based on modeling the PSF as a deterministic or stochastic model. This approach relies on the estimation of the parameter of the model in order to estimate the PSF. *Autoregressive moving average* (ARMA) model was proposed in [JMGS93]. The latter approach was limited to 1D signals deconvolution along the axial direction but their extension to the 2D case was very quickly restricted from a computational point of view. A more efficient way to perform this estimation is based on a non-parametric approach. Here [APR95] had proposed a higher-order statistics (HOS) based approach that was shown to be less sensitive to noise. However, a drawback of this approach is that consistent estimates of higher order statistics require long stationary time realizations to be available. Moreover the extension to higher dimensional cases is not straightforward and may become fairly too computationally demanding. Thus, an alternative method of PSF estimation was proposed in the literature: homomorphic filtering.

The homomorphic methods is nowadays one of the most widely applied techniques [OBS01]. The idea is to transform the convolution model into a form where the PSF and the TRF are easily dissociated. More precisely, these methods use the classical cepstrum estimation of US images [JL94, Tax95] or its more complex versions [Tax97, TS01]. Ignoring the additive noise corrupting the measurements, the linear model (2.26) in the frequency domain is given by:

$$Y(\omega) = H(\omega)X(\omega) \quad (2.42)$$

where $Y(\omega)$, $X(\omega)$ and $H(\omega)$ are the Fourier transforms of $y(r)$, $x(r)$ and $h(r)$ respectively. r and ω represent the location of images in the spatial and frequency domain respectively. The log spectrum of the RF image y is applied, namely cepstrum, as follows:

$$\begin{aligned} \hat{Y}(\omega) &= \log |Y(\omega)| + i\angle Y(\omega) \\ &= \log |X(\omega)| + \log |H(\omega)| + i\{\angle X(\omega) + \angle H(\omega)\} \end{aligned} \quad (2.43)$$

where $|\cdot|$ and \angle represent the magnitude and phase of the complex signals respectively. It has been shown that the PSF energy is confined to the first few samples of the cepstrum domain, while the reflectivity function energy is distributed over the entire cepstrum domain. In other words, $\log |X(\omega)|$ and $\angle X$ are spiky noise-like sequences while $\log |H(\omega)|$ and $\angle H$ are smooth signals. Hereby, the estimation of the PSF's cepstrum is applied into two steps: the magnitude and the phase. In [JL94, TF99], it was shown that a low pass filtering can be applied in order to estimate the magnitude. This approach was extended to 3D in [Tax01]. However, estimating the phase represents a difficult problem to solve since the phase is wrapped [TJ04, STJ99]:

$$-\pi \leq \mathbf{W}\{\angle Y\} \leq \pi \quad (2.44)$$

The first attempts have considered a minimum phase approach [JL94]. Hereafter, the minimum phase approach was adopted in [APR95, Tax97], and has formed a base for a large contributions based on the cepstrum estimation [TJ04, JT06, MA05, MT07]. In this case, a simple Hilbert transform can be applied in order to estimate the phase. However, this assumption is far from realistic. Thus, several works have investigated the phase unwrapping of the cepstrum. A generalized homomorphic filtering technique was proposed in [MA05]. This technique had replaced the truncation of the cepstrum by projecting the real and imaginary components of the cepstrum on a reduced resolution space. It relies on the difference of smoothness properties between the PSF and the TRF [ILV89, Jen94, MA05, NPK⁺07]. Once the PSF is estimated in the sequential methodology, any 'non-blind' deconvolution method can be applied. [JMGS93] had considered a parametric model of the PSF and had applied a Wiener filtering. [HLL⁺01] had presented deconvolution method in the Bayesian framework based on Markov random field models. In the same perspective, authors in [ZBKT14] had presented a joint deconvolution-segmentation method applied on US images and based on Gaussian estimators based on GGD priors. Another non-parametric approach of PSF estimation was proposed by [MT07] based on inverse filtering. This work was lately outperformed by the generalized homomorphic filtering proposed in [MA05] due to the high sensitivity of the inverse filtering approach to the noise. Thus, a large number of applications had adopted the homomorphic filtering approach for the PSF estimation in a first step followed by a second step, the deconvolution step of US images in super-resolution

[ZWB⁺16b, MBK12], compressive sensing approaches [CBK16b] in an ADMM framework.

2.5.2 Fully blind deconvolution

In this case, the PSF is estimated concurrently with the TRF. The idea is that by estimating and updating the PSF estimation during the TRF estimation process, an enhancement is expected. [MBBK13] adopted the homomorphic estimation of the PSF with minimum phase as the prior information and had built a joint restoration problem that estimates the TRF and the coefficients of the PSF to reduce the inaccuracy due to the minimum phase assumption. In the same scope, [MBK19] had considered the magnitude of the PSF estimation done by homomorphic filtering as the prior information and had combined to the restoration problem, the estimation of the PSF phase. The phase of the latter is estimated jointly with the TRF in the restoration problem. [MT07] had taken the same prior information in the latter approach but considering an inverse filter in order to estimate the phase. [JT08] modeled the TRF as a white Gaussian signal and therefore solve the blind deconvolution by alternating Wiener deconvolution. Authors in [YZX12b] have presented a deconvolution problem based on the single-input multiple-output (SIMO) channel model, where the PSF is the single input, and the TRF signals are the multiple outputs. However, most of the methods in this scope had solved a problem similar to the following:

$$\min_{x \in \mathbb{R}^N, h \in \mathbb{R}^n} \alpha P(x) + \gamma P(h) + \|y - Hx\|_2^2 \quad (2.45)$$

where $P(x)$ and $P(h)$ are the regularization terms containing prior information about the TRF and the PSF, respectively. h represents the PSF with a support of size n . Another alternative solution is to give the PSF a closed-form model and replaces the PSF estimation by the estimation of its model's parameters [ZWB⁺16c]. However, this model risks being far from reality due to non-realistic assumptions.

2.6 Orientations

This chapter presented several works applied in the US image enhancement used in the pre-processing and post-processing approaches. Although the first category presents promising results, it suffers from

slow advances in the technological aspect. Thus, the second category had gained a lot of interest based on its ability to restore images after acquisition. On the other side, we have presented the edge of the harmonic images in terms of resolution. Although, it suffers from higher attenuation in contrast to the fundamental image, harmonic US image is still widely used in the medical application for diagnostic purposes. Comparing the fundamental and the harmonic images, we showed that the fundamental images keep a considerable edge over the harmonic images in terms of signal-to-noise ratio. Therefore, in the scope of post-processing, this thesis aims to apply a joint restoration of the fundamental and harmonic image. This restoration aims to present a better enhancement of the restored images with contrast to the conventional deconvolution solutions. The thesis aims to present a solution to restore the two US image modalities jointly in order to collect their advantages while trying to overcome the attenuation issue. This work was inspired by [TJ04] that proves the interest of the latter approach in terms of resolution enhancement. This manuscript will present in Chapter 3 the advantage of the proposed approach, and will solve the restoration problem considering spatial variability of the PSF and presenting a new method of the PSF estimation in the Chapter 4.

CHAPTER 3

Joint ultrasound image deconvolution

Part of this chapter has been adapted from the journal paper [HBKT21]

Contents

4.1	Introduction	100
4.2	Fully blind joint deconvolution	100
4.2.1	Problem reformulation	101
4.2.2	Optimization algorithm	101
4.2.2.1	TRF estimation	102
4.2.2.2	PSF estimation	102
4.2.3	Results	103
4.2.3.1	Simulated image	104
4.2.3.2	Phantom image	108
4.2.3.3	Carotid image	110
4.2.4	Discussion	112
4.3	Joint deconvolution with a spatially varying PSF	114
4.3.1	Block-wise joint deconvolution	115
4.3.2	Results	116
4.4	Conclusion	120

3.1 Introduction

US imaging is one of the leading imaging modalities due to its low cost, high frame rate, non-ionizing risk, and ease of use. However, the quality of the US images (in terms of resolution, contrast and SNR) imposes the application of enhancement techniques. Thereby, in the previous chapter, we presented the applied methods (pre-processing and post-processing methods) to improve the quality of US images. Although the post-processing techniques show promising results, the slow technological advances and the cost of the implementation are the significant limitations guiding to seek alternative solutions through post-processing techniques. This thesis presents a post-processing method of restoration of US images: deconvolution. The deconvolution is well established nowadays in the literature of restoration of US images.

On the other hand, we have presented the harmonic images as a US image modality in the previous chapter offering a distinctive edge over the fundamental image in terms of resolution and contrast. However, it always suffers from the frequency dependant attenuation and low signal-to-noise ratio. The raw US data contains both fundamental and harmonic components, which can be isolated to reconstruct fundamental or harmonic images (see Figure 2.5). This separation can be done using beamforming techniques such as pulse inversion and phase cancellation [SCB99]. It can also be done using post-processing techniques such as system identification [HBK⁺18, PE03b], or linear filtering. In this work, linear band-pass filters are used for this separation due to their simplicity and low-frequency overlap between the fundamental and harmonic components. Taxt and Jirik in [TJ04, JT08] have presented the interest of the deconvolution of harmonic US images. In addition, they have introduced a compounding step between the envelope of the restored fundamental and harmonic images. The latter approach has offered a remarkable enhancement in resolution and speckle reduction compared to the conventional deconvolution approach that uses one image modality in the restoration process. Encouraged by these results, the main contribution of this thesis follows the trend in [TJ04, JT08] by including the harmonic information in the restoration process. However, we will present an advanced approach by applying a joint deconvolution that employs fundamental and harmonic images simultaneously. In other words, instead of restoring the two images independently,

we propose in this work a joint deconvolution of fundamental and harmonic images through the minimization of an appropriate cost function. The data fidelity terms are constructed from the fundamental and harmonic image formation models using the unknown PSF. Existing algorithms for PSF estimation are based on parametric models [BRP⁺19a] or estimate the PSF directly from the RF data [MA05]. This chapter follows the trend of deconvolution with estimated PSF in a pre-processing step from the beamformed RF images followed by the estimation of the TRF. The proposed method can be used regardless of the acquisition scheme, which can be conventional focused or synthetic, i.e., with a plane or diverging wave imaging. The results reported in this chapter have been obtained using RF images beamformed with the classical delay and sum approach, which is applied to raw data acquired using the standard pulse-echo imaging sequence.

3.2 US image formation models

In the case of linear propagation, a US image model expresses the US RF signal as a convolution between a spatially varying PSF and the TRF. Interestingly, a similar model can also be considered in the case of nonlinear propagation with small nonlinearities (see [NPK⁺06] and [ZAI03]). Note that this assumption also holds in THI, given that the scattering of soft tissues is weak.

To further reduce the complexity of the restoration problem resulting from a spatially varying PSF [FBKV18a, Mic17], and to maintain realistic conditions, most of the existing studies have addressed the restoration problem with a spatially invariant PSF by restricting the process to small image segments [AV85, NO98, GCC⁺09, CBK16b]. The proposed work follows this trend by considering a spatially invariant PSF. However, in contrast to most of the existing works, linear and non-linear propagation models are jointly considered for TRF restoration. After forming the fundamental and harmonic images by filtering the beamformed RF image (more details about the filtering process are given in section 3.6.2), the following image formation models are considered:

$$\mathbf{y}_f = \mathbf{H}_f \mathbf{x} + \mathbf{n}_f, \quad (3.1)$$

$$\mathbf{y}_h = \mathbf{W} \mathbf{H}_h \mathbf{x} + \mathbf{n}_h, \quad (3.2)$$

where \mathbf{y}_f and $\mathbf{y}_h \in \mathbb{R}^N$ are the observed fundamental and harmonic RF images, N is the number of image pixels, $\mathbf{x} \in \mathbb{R}^N$ is the TRF to be estimated and \mathbf{n}_f and $\mathbf{n}_h \in \mathbb{R}^N$ are white Gaussian additive noises. Moreover, the matrices \mathbf{H}_f and $\mathbf{H}_h \in \mathbb{R}^{N \times N}$ are block circulant with circulant blocks (BCCB) matrices formed using the fundamental and harmonic PSFs \mathbf{h}_f and \mathbf{h}_h . The attenuation of the harmonic image with depth is considered in the second model by using a diagonal matrix $\mathbf{W} \in \mathbb{R}^{N \times N}$ that accounts for the level of attenuation at each depth. This attenuation can be adjusted using the ratio between the energies of the fundamental and first harmonic spectra. The choice of this matrix will be explained in the section devoted to simulation results. The proposed restoration problem consists in estimating the TRF \mathbf{x} from the measurements \mathbf{y}_f and \mathbf{y}_h . Note that the models in (3.1) and (3.2) also depend on the fundamental and harmonic PSFs, that are unknown in practical situations. The estimation of the TRF \mathbf{x} and the unknown PSFs \mathbf{H}_f and \mathbf{H}_h are detailed in the next section.

3.3 Problem reformulation

This section introduces the algorithm proposed to estimate the TRF from fundamental and harmonic RF images based on the direct models (3.1) and (3.2), for a known PSF and a known weight matrix \mathbf{W} . From a Bayesian perspective, the TRF can be estimated using the standard maximum a posteriori (MAP) estimator, which maximizes the posterior distribution of the TRF defined:

$$p(\mathbf{x}|\mathbf{y}_f, \mathbf{y}_h) \propto p(\mathbf{y}_f|\mathbf{x})p(\mathbf{y}_h|\mathbf{x})p(\mathbf{x}), \quad (3.3)$$

where \propto means 'proportional to', $p(\mathbf{x})$ is the prior of \mathbf{x} and the likelihood functions $p(\mathbf{y}_f|\mathbf{x})$ and $p(\mathbf{y}_h|\mathbf{x})$ are those of the following Gaussian distributions

$$\begin{aligned} \mathbf{y}_f|\mathbf{x} &\sim \mathcal{N}(\mathbf{H}_f\mathbf{x}, \sigma_f^2\mathbf{I}_N) \\ \mathbf{y}_h|\mathbf{x} &\sim \mathcal{N}(\mathbf{W}\mathbf{H}_h\mathbf{x}, \sigma_h^2\mathbf{I}_N), \end{aligned} \quad (3.4)$$

where \mathbf{I}_N is the $N \times N$ identity matrix, σ_f^2 and σ_h^2 are the noise variances, \mathcal{N} stands for the Gaussian distribution and the two additive noises \mathbf{n}_f and \mathbf{n}_h are assumed to be independent. The negative

log-posterior of \mathbf{r} is given by

$$\begin{aligned}
 -\log p(\mathbf{x}|\mathbf{y}_f, \mathbf{y}_h) \propto & \underbrace{\frac{1}{2}\|\mathbf{y}_f - \mathbf{H}_f\mathbf{x}\|_2^2}_{\text{Fundamental data fidelity term}} + \\
 & \underbrace{\frac{1}{2}\|\mathbf{y}_h - \mathbf{W}\mathbf{H}_h\mathbf{x}\|_2^2}_{\text{Harmonic data fidelity term}} + \underbrace{\log[p(\mathbf{x})]}_{\text{Regularization}}.
 \end{aligned} \tag{3.5}$$

In this work, we consider a Laplacian prior distribution $p(\mathbf{x})$, leading to an ℓ_1 -norm regularization term. This prior has been used successfully for US imaging e.g., in [YZX12b, MBBK13, CBK16b, MT07]. Finally, the TRF image \mathbf{x} is estimated by solving the following minimization problem:

$$\mathbf{x}^* = \arg \min_{\mathbf{x}} \frac{1}{2}\|\mathbf{y}_f - \mathbf{H}_f\mathbf{x}\|_2^2 + \frac{1}{2}\|\mathbf{y}_h - \mathbf{W}\mathbf{H}_h\mathbf{x}\|_2^2 + \mu\|\mathbf{x}\|_1, \tag{3.6}$$

where μ is a hyperparameter weighting the contribution of the sparse regularization with respect to the two data fidelity terms

3.4 Optimization

The cost function in (3.6) is convex but non-differentiable because of the ℓ_1 -norm, thus preventing the use of traditional gradient-based algorithms. As an alternative, variable splitting-based algorithms developed for non-differential problems such as the alternating direction method of multipliers (ADMM) [BPC⁺11], the forward-backward algorithm (FBA) [CP11] or the fast iterative shrinkage thresholding algorithm (FISTA) [BT09], can be used to solve (3.6). This paper proposes to estimate the TRF from fundamental and harmonic RF images using a dedicated algorithm based on ADMM [GM76, BPC⁺11]. The choice of ADMM was mainly based on the results in [FBDA09, ABDF10a]. Specifically, the latter presents a particular parametrization and solution in the Fourier domain aiming at improving the convergence properties of ADMM, shown to have better performance than FISTA. The parametrization adopted in the proposed algorithm follows this trend.

3.4.1 Basics of the Alternating Direction Method of Multipliers

In this section, we present the basics of ADMM before going into the details of implementation. The ADDM algorithm is well suited to distributed convex optimization, and in particular to large-scale

problems arising in statistics, machine learning, and related areas [BPC⁺11]. The main motivation for using ADMM is to split the optimization problem in (3.6) into several sub-problems that are easy to solve, as shown hereafter [FBDA09, ABDF10a]. ADMM is a general optimization framework adapted to solve the following problem:

$$\begin{aligned} \min_{\mathbf{u}, \mathbf{v}} \quad & f_1(\mathbf{u}) + f_2(\mathbf{v}) \\ \text{s.t.} \quad & \mathbf{A}\mathbf{u} + \mathbf{B}\mathbf{v} = \mathbf{c}, \end{aligned} \quad (3.7)$$

where f_1 and f_2 are closed convex and separable functions (depending on \mathbf{u} and \mathbf{v} respectively). The ADMM algorithm is based on the augmented Lagrangian \mathcal{L}_A defined as:

$$\mathcal{L}_A(\mathbf{u}, \mathbf{v}, \boldsymbol{\lambda}) = f_1(\mathbf{u}) + f_2(\mathbf{v}) + \frac{\beta}{2} \left\| \mathbf{A}\mathbf{u} + \mathbf{B}\mathbf{v} + \frac{\boldsymbol{\lambda}}{\beta} \right\|_2^2, \quad (3.8)$$

where β is a regularization parameter for the linear constraint and $\boldsymbol{\lambda}$ is the vector of Lagrangian multipliers. The vectors \mathbf{u} , \mathbf{v} and $\boldsymbol{\lambda}$ are then computed as follows [BPC⁺11]:

$$\begin{aligned} & \text{For } k = 0, \dots \\ & \begin{cases} \mathbf{u}^{k+1} = \arg \min_{\mathbf{u}} \mathcal{L}_A(\mathbf{u}, \mathbf{v}^{(k)}, \boldsymbol{\lambda}^{(k)}) \\ \mathbf{v}^{k+1} = \arg \min_{\mathbf{v}} \mathcal{L}_A(\mathbf{u}^{(k+1)}, \mathbf{v}, \boldsymbol{\lambda}^{(k)}) \\ \boldsymbol{\lambda}^{(k+1)} = \boldsymbol{\lambda}^{(k)} + \beta(\mathbf{A}\mathbf{u}^{(k+1)} + \mathbf{B}\mathbf{v}^{(k+1)} - \mathbf{c}). \end{cases} \end{aligned} \quad (3.9)$$

3.4.2 Proposed ADMM parametrization

In this subsection, we introduce the ADMM parametrization proposed to solve the (3.6). First, note that (3.6) can be rewritten as follows:

$$(\mathbf{u}^*, \mathbf{w}^*, \mathbf{z}^*) = \arg \min_{\mathbf{u}, \mathbf{w}, \mathbf{z}} \frac{1}{2} \|\mathbf{y}_f - \mathbf{H}_f \mathbf{u}\|_2^2 + \frac{1}{2} \|\mathbf{y}_h - \mathbf{W} \mathbf{z}\|_2^2 + \mu \|\mathbf{w}\|_1 \quad (3.10)$$

$$\text{with } \begin{cases} f_1(\mathbf{u}) = \frac{1}{2} \|\mathbf{y}_f - \mathbf{H}_f \mathbf{u}\|_2^2 \\ f_2(\mathbf{v}) = \frac{1}{2} \|\mathbf{y}_h - \mathbf{W} \mathbf{z}\|_2^2 + \mu \|\mathbf{w}\|_1 \\ \mathbf{z} = \mathbf{H}_h \mathbf{r}, \mathbf{w} = \mathbf{u} = \mathbf{r} \\ \mathbf{v} = \begin{bmatrix} \mathbf{w} \\ \mathbf{z} \end{bmatrix} \end{cases} \quad \text{and } \begin{cases} \mathbf{A} = \begin{bmatrix} I_N \\ \mathbf{H}_h \end{bmatrix} \\ \mathbf{B} = \begin{bmatrix} -I_N & 0 \\ 0 & -I_N \end{bmatrix} \\ \mathbf{c} = \mathbf{0}_{2N} \end{cases}$$

The main motivation behind the proposed parameterization, and in particular the use of the auxiliary variables \mathbf{u} and \mathbf{v} , is to separate the operators \mathbf{W} and \mathbf{H}_h . As it will be shown below, \mathbf{H}_h can be diagonalized in the Fourier domain due to its BCCB property, while \mathbf{W} is a diagonal matrix in the spatial domain. Separating \mathbf{H}_h and \mathbf{W} simplifies the optimization algorithm, which can be divided into two easier subproblems in the Fourier domain (for \mathbf{H}_h) and in the spatial domain (for \mathbf{W}), where these two matrices have diagonal representations.

3.4.3 Implementation details

The solution of (3.10) can be iteratively obtained in the ADMM framework as described in Algorithm 1 and further detailed in the following three main steps. Note that the algorithm is initialized by setting $\mathbf{u}^{(0)}$, $\mathbf{z}^{(0)}$ and $\mathbf{w}^{(0)}$ to the fundamental image and the Lagrangian multipliers $\boldsymbol{\lambda}^{(0)}$ to 0.

Step 1: Update \mathbf{u}

The vector \mathbf{u} can be updated using the analytical solution of the optimization problem in line 3 of Algorithm 1. Denoting as $\boldsymbol{\lambda} = \begin{bmatrix} \lambda_1 \\ \lambda_2 \end{bmatrix} \in \mathbb{R}^{2N}$ the vector of Lagrangian multipliers, the update of \mathbf{u} at iteration k is defined as:

$$\mathbf{u}^{k+1} = (\mathbf{H}_f^T \mathbf{H}_f + \beta \mathbf{H}_h^T \mathbf{H}_h + \beta \mathbf{I}_N)^{-1} (\mathbf{H}_f^T y_f + \beta \mathbf{H}_h^T \mathbf{z}^k - \boldsymbol{\lambda}_1^k - \mathbf{H}_h^T \boldsymbol{\lambda}_2^k + \beta \mathbf{w}^k). \quad (3.11)$$

Under the hypothesis of circular convolution, \mathbf{H}_f and \mathbf{H}_h are BCCB matrices having the spectral decompositions:

$$\mathbf{H}_f = \mathbf{F}^* \boldsymbol{\Lambda}_f \mathbf{F} \quad (3.12)$$

$$\mathbf{H}_h = \mathbf{F}^* \boldsymbol{\Lambda}_h \mathbf{F}, \quad (3.13)$$

Algorithm 1: ADMM algorithm for TRF estimation

Input: $\mathbf{y}_f, \mathbf{y}_h, \mathbf{H}_f, \mathbf{H}_h$.

1. Set $k = 0$, choose $\mu > 0, \beta > 0, \mathbf{u}^0, \mathbf{v}^0, \boldsymbol{\lambda}^0$
 2. Repeat until the relative cost function error $< \epsilon$
// Estimate \mathbf{u} (closed-form solution in the Fourier domain)
 3. $\mathbf{u}^{k+1} = \min_{\mathbf{u}} \frac{1}{2} \|\mathbf{y}_f - \mathbf{H}_f \mathbf{u}\|_2^2 + \frac{\beta}{2} \left\| \mathbf{A} \mathbf{u} + \mathbf{B} \mathbf{v}^k + \frac{\boldsymbol{\lambda}^k}{\beta} \right\|_2^2$
// Estimate $\mathbf{v} = \begin{bmatrix} \mathbf{w} \\ \mathbf{z} \end{bmatrix}$
// Estimate \mathbf{w} using soft thresholding
 4. $\mathbf{w}^{k+1} = \min_{\mathbf{w}} \mu \|\mathbf{w}\|_1 + \frac{\beta}{2} \left\| \mathbf{u}^{k+1} - \mathbf{w} + \frac{\boldsymbol{\lambda}_1^k}{\beta} \right\|_2^2$
// Estimate \mathbf{z} (closed-form solution in the Fourier domain)
 5. $\mathbf{z}^{k+1} = \min_{\mathbf{z}} \frac{1}{2} \|\mathbf{y}_h - \mathbf{W} \mathbf{z}\|_2^2 + \frac{\beta}{2} \left\| \mathbf{H}_h \mathbf{u}^{k+1} - \mathbf{z} + \frac{\boldsymbol{\lambda}_2^k}{\beta} \right\|_2^2$
// Update the Lagrangian multiplier
 6. $\boldsymbol{\lambda}^{k+1} = \boldsymbol{\lambda}^k + \beta(\mathbf{A} \mathbf{u}^{k+1} + \mathbf{B} \mathbf{v}^{k+1})$
-

where \mathbf{F} and \mathbf{F}^* are the 2D Fourier and inverse Fourier transform matrices, $\boldsymbol{\Lambda}_f = \text{diag}(\mathbf{F} \mathbf{h}_f)$ and $\boldsymbol{\Lambda}_h = \text{diag}(\mathbf{F} \mathbf{h}_h)$ are diagonal matrices whose diagonal elements are the Fourier coefficients of the first column of matrices \mathbf{H}_f and \mathbf{H}_h . The solution of (3.11) can finally be written as follows:

$$\mathbf{u}^{k+1} = \mathbf{F}^* (\boldsymbol{\Lambda}_f^* \boldsymbol{\Lambda}_f + \beta \boldsymbol{\Lambda}_h^* \boldsymbol{\Lambda}_h + \beta \mathbf{I}_N)^{-1} (\boldsymbol{\Lambda}_f^* \mathbf{F} \mathbf{y}_f + \beta \boldsymbol{\Lambda}_f^* \mathbf{F} \mathbf{z}^k - \mathbf{F} \boldsymbol{\lambda}_1^k - \boldsymbol{\Lambda}_f^* \mathbf{F} \boldsymbol{\lambda}_2^k + \beta \mathbf{F} \mathbf{w}^k). \quad (3.14)$$

The computational complexity of the solution is reduced from $\mathcal{O}(N^3)$ in (3.11) to $\mathcal{O}(N \log N)$ in (3.14) (using the decompositions in (3.12) and (3.13)). In (3.14), $\boldsymbol{\Lambda}_f^* \boldsymbol{\Lambda}_f$ and the Fourier operator can be computed with complexities of the order $\mathcal{O}(N)$ and $\mathcal{O}(N \log N)$.

Step 2: Update \mathbf{v}

$\mathbf{v} = \begin{bmatrix} \mathbf{w} \\ \mathbf{z} \end{bmatrix}$ is updated using two substeps:

Substep 2.1: Update \mathbf{w}

Update \mathbf{w} by minimizing the cost function in line 4 of Algorithm 1. The solution to this problem can be simply implemented by a soft-thresholding operator [CBK16a]:

$$\begin{aligned} \mathbf{t}^k &= \mathbf{u}^{k+1} + \boldsymbol{\lambda}_1^k / \beta \\ \mathbf{w}^{k+1} &= \text{soft}_{\frac{\mu}{\beta}}(\mathbf{t}^k) = \max \left\{ |\mathbf{t}^k| - \frac{\mu}{\beta}, 0 \right\} \text{sign}(\mathbf{t}^k). \end{aligned} \quad (3.15)$$

Substep 2.2: Update \mathbf{z}

The optimization problem in line 5 of Algorithm 1 has an analytical solution defined as:

$$\mathbf{z}^{k+1} = (\mathbf{W}^T \mathbf{W} + \beta \mathbf{I}_N)^{-1} (\mathbf{W}^T \mathbf{y}_h + \beta \mathbf{H}_h \mathbf{u}^{k+1} + \boldsymbol{\lambda}_2^k). \quad (3.16)$$

Step 3: Update λ

Update the Lagrange multiplier as suggested in [BPC+11]

$$\boldsymbol{\lambda}^{k+1} = \boldsymbol{\lambda}^k + \beta (\mathbf{A} \mathbf{u}^{k+1} + \mathbf{B} \mathbf{v}^{k+1}). \quad (3.17)$$

As shown in Algorithm 1, the proposed ADMM-based algorithm iterates the previous steps until a stopping criterion has been satisfied. The stopping criterion for all the results reported in this paper was the relative error between two consecutive values of the cost function in (3.10) defined as:

$$\frac{|F(\mathbf{x}^{k+1}) - F(\mathbf{x}^k)|}{F(\mathbf{x}^k)} < \epsilon \quad (3.18)$$

where F is the cost function and k is the iteration number. The tolerance parameter ϵ was set to 10^{-4} .

3.5 PSF estimation

The strategy of deconvolution in this chapter follows the trend of deconvolution with pre-estimated PSF. Thus, the TRF estimation algorithm proposed in the previous subsection imposes an estimation of the fundamental and harmonic PSFs in a first step. These PSFs can be estimated from the data, *i.e.*, from the beamformed RF images that are also used for TRF restoration. Several parametric

approaches have been investigated for this estimation, exploiting an *a priori* model of the PSF (see *e.g.* in [BRP⁺19a, MA05, RKB08]). To overcome the rigidity of parametric models, several non-parametric methods can be also found in the literature, among which one may cite the homomorphic technique [Opp65, Tax97, JL94]. The homomorphic method assumes that the PSF and the TRF have disjoint supports in the cepstrum domain, and thus estimate the amplitude of the PSF by low pass filtering. Application of the homomorphic filtering to US image restoration has been studied in [Tax95, MA05]. In this work, the adopted PSF estimation method is the one presented in [MA05] based on homomorphic filtering. The goal of the latter method is to discriminate the PSF and the TRF terms based on their smoothness properties. The PSF function is usually smooth in contrast to the reflectivity function that can be considered as noise. Thus, the PSF estimation, after homomorphic transformation, is divided into two main steps: estimation of the PSF-amplitude and estimation of the PSF phase. Based on the smoothness difference, the TRF can be considered as a white Gaussian noise. Therefore, in order to calculate the amplitude of the PSF, a de-noiser can be applied on the real part of the homomorphic transformation of the observation. The log spectrum of the TRF is approximated to be viewed as white Gaussian noise contaminated with spiky outliers (statistical demonstration is presented in [MA05, MA03]). The latter outliers may be considered as useful information by the de-noiser and falsify the desired result. So in order to accomplish the estimation of the amplitude of the PSF, an outlier removal step is applied [MA03] followed by the denoising step. The de-noiser by wavelet shrinkage was applied here as introduced in [Don95]. The latter de-noiser transform the signal into a wavelet orthogonal domain, then apply a soft-thresholding step with a threshold t , and finally apply in inverse mapping. The straightforward estimation based on the smoothness of the log-amplitude of the PSF can not be applied on the PSF phase. The main issue here is the phase are wrapped and a phase unwrapping step is considered essential in this case before the estimation based on the smoothness properties. To do so, a so-called 'smoothing integration' method is proposed. Thus, recovering the PSF phase can be done by applying a de-noiser on the partial derivatives of the PSF phase and then integrated the obtained result. Equivalently, the estimation is performed by integrating the measured partial derivatives of the RF-image phase over a predefined "smooth" subspace. For the same reason in the case of log amplitude of the spectrum,

an outlier removal should be applied on the derivative of the phase before integration. The threshold t of the de-noiser by wavelet shrinkage was set to 1 in our application. Finally, the estimation of the PSF was done from a region of interest (ROI) extracted around the transmission (TX) focal point, in order to benefit from optimal SNR conditions. Note that a detailed analysis of the sensitivity of ultrasound deconvolution to PSF parameters can be found in [SPN⁺09].

3.6 Data and evaluation metrics

In this section, we will present the several synthetic and real data used to test our approach and their acquisition setup as well. In the following, a spectral analysis of the experimental data and its relation with the attenuation matrix \mathbf{W} in (3.2) will be detailed. On the other hand, we will present the quantitative metrics used in this thesis to compare the results quantitatively.

3.6.1 Data simulation and acquisition

3.6.1.1 Synthetic data

- **Kidney phantom**

A controlled ground-truth TRF was computed from a kidney magnetic resonance image (MRI) slice, by generating 10^6 scatterers (*i.e.*, 30 scatterers per resolution cell) with random Gaussian amplitudes. The gray levels of the MRI image pixels were used to scale the variance of the Gaussian distribution. The size of the resulting TRF image is 1150×300 pixels. Fundamental (\mathbf{y}_f) and harmonic (\mathbf{y}_h) RF images were simulated by convolving this TRF with two spatially invariant PSFs \mathbf{h}_f and \mathbf{h}_h , with central frequencies $f_0 = 3.5$ MHz and $2f_0 = 7$ MHz. The two PSFs were generated based on a simple Gaussian window modulated by a sine function. The full width at half maximum (FWHM) of the fundamental PSF was 3 mm in the lateral direction and 1.1 mm in the axial direction. The FWHM of the harmonic PSF was 1 mm in the lateral direction and 0.5 mm in the axial direction. Both PSFs were generated using 6 sine cycles. The resulting images were contaminated by additive white Gaussian noise corresponding to a signal to noise ratio $\text{SNR} = 40$ dB. The harmonic image was finally generated by including

an attenuation matrix \mathbf{W} , accounting for the loss of wave amplitude due to absorption and scattering, to respect the direct model introduced in Section 3.2. More precisely, the simulation of \mathbf{W} was inspired by the exponential attenuation model used in US imaging defined by:

$$A(z) = A_0 e^{-\mu_A z}, \quad (3.19)$$

where $A(z)$ is the signal amplitude at a given depth z , A_0 is the initial signal amplitude and μ_A is the attenuation factor, fixed to 1.15 Nepers/cm. Note that this model assumes that the attenuation only depends on depth, and is thus constant with respect to the lateral direction.

- **Fetus image**

To further consider nonlinear propagation effects, a second synthetic RF image was generated using a non-linear ultrasound image simulator called CREANUIS [VBTC13]. The objective of this second simulated image was to account for more realistic simulations and to evaluate the interest of the proposed method for short excitation pulses. In particular, a linear probe with a 245 μm pitch and 30 μm kerf was simulated. In transmission, 64 elements were activated, focused at 30 mm depth, and apodized with a Hanning window. The TX signal was a 1-cycle sine burst at 3 MHz with Gaussian tapering. The TRF corresponded to the fetus example available in Field II [JM97]. The nonlinear coefficient B/A was fixed at 3.5.

3.6.1.2 Experimental images

The experimental data were acquired with a ULA-OP 256 research scanner connected to the wide-band 192-element linear array probe LA533 (Esaote S.p.A., Florence, Italy), with 110% bandwidth centered at 8 MHz and a 245 μm pitch. In transmission (TX), 64 elements were activated, focused at 33 mm depth, and apodized with a Hanning window with an F-number equal to 4. The TX excitation signal was a 10-cycle sine burst at 5 MHz with Hanning tapering and peak amplitude of 90 Vpp, for all the performed scans [MRTM86]. The size of the RF images is 384×4480 , i.e., there are 384 scanned RF lines and the number of samples covering the depth of 45 mm is 4480. The sampling frequency was 78.125 MHz. Two acquisitions were considered to test the proposed algorithms, as

described by hereafter.

- **Phantom image**

The first data was acquired on a tissue-mimicking phantom (model 404GS LE, Gammex Inc., Middleton, WI, USA) including both anechoic/hypoechoic cysts and wire targets, as shown in Figure 3.1. The simple structures in this phantom allowed us to objectively evaluate the resolution and the contrast gain enabled by the proposed method.

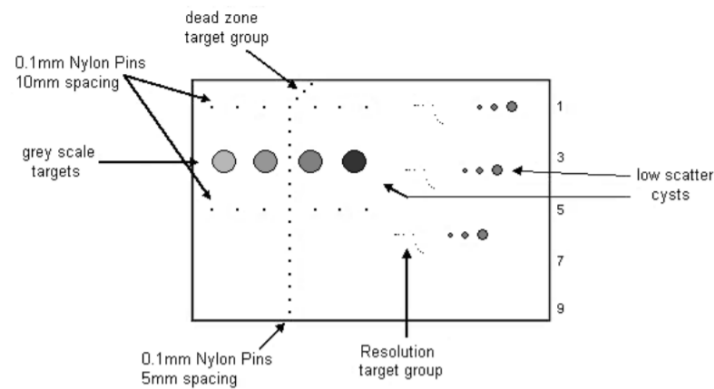


Figure 3.1: Phantom model 404GS LE, Gammex Inc.

- **Carotid image**

The second acquisition was done *in vivo* by scanning the carotid artery and jugular vein of a young healthy volunteer (see Figure 3.2). This image contains more complicated structures and represents a more difficult challenge than the previous phantom to prove the functionality of the proposed restoration procedure.

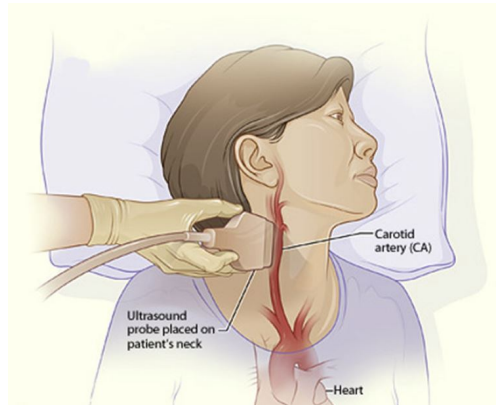


Figure 3.2: Position of the patient's neck during ultrasound carotid imaging [CAN⁺17].

3.6.2 Spectral analysis of the experimental data

This section provides an analysis of the experimental data in the Fourier domain. This analysis has mainly two objectives:

- Justify the separation of fundamental and harmonic images by linear filtering,
- Explain how the attenuation matrix \mathbf{W} was estimated from real data.

In order to obtain the fundamental and harmonic images, a bandpass FIR filter with a Hamming window was applied to the RF image. The filter bandwidths for the fundamental and harmonic images were set to [4MHz, 6MHz] (order 50) and [9MHz, 11MHz] (order 60) respectively. These bandwidths are in agreement with the fundamental and first harmonic frequencies of the transducer, i.e., $f_0 = 5$ MHz and $2f_0 = 10$ MHz. An example of the result obtained with this filtering procedure is shown in Figure 3.3 for a carotid image. Note that there is a reduced spectral overlap between the fundamental and first harmonic spectra, justifying the use of linear filtering for their separation. In the case of experimental images, the attenuation matrix \mathbf{W} was constructed directly from the observed data, without considering any *a priori* model. More precisely, we computed the ratios between the energies of the fundamental and harmonic components within sliding blocks extracted from the RF image at each depth [YCM⁺07]. An example of estimated weights obtained with this method is shown in Figure 3.4.

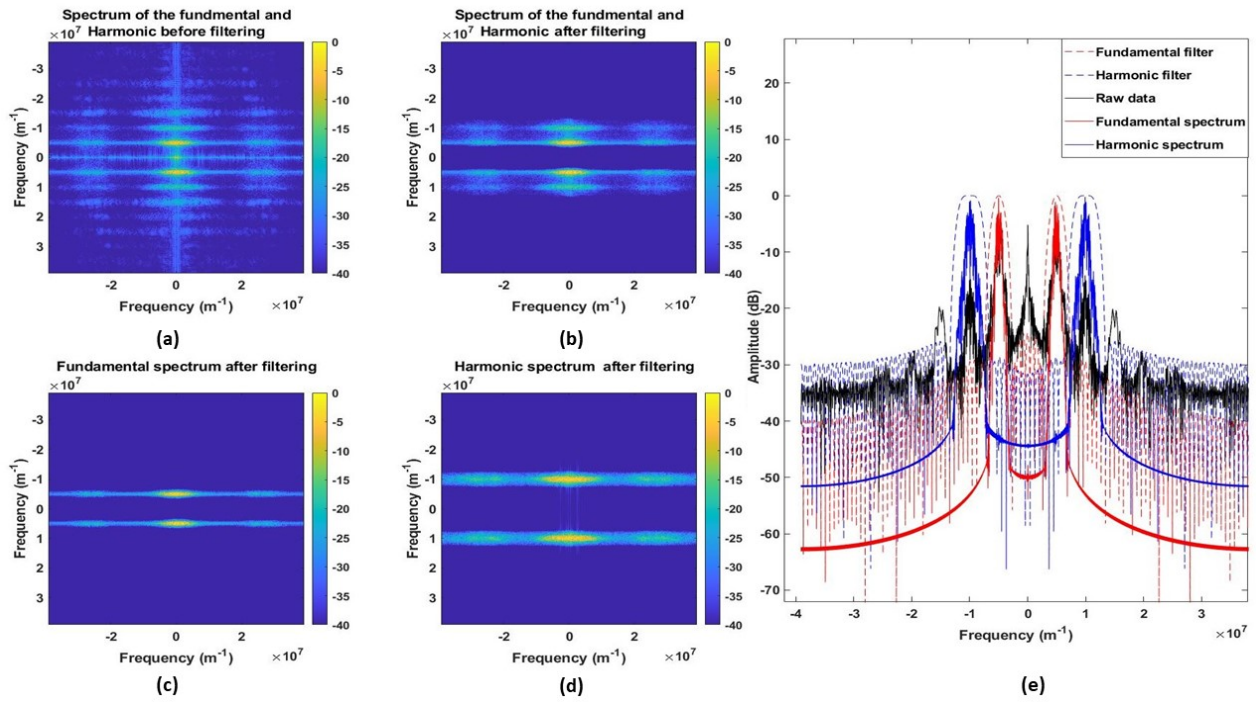


Figure 3.3: Carotid image: (a) Spectrum of the original RF image, (b) spectrum of the filtered RF image containing the mixed information from fundamental and harmonic data, (c) spectrum of the fundamental image \mathbf{y}_f after filtering, (d) spectrum of the harmonic image \mathbf{y}_h after filtering, (e) spectrum of one RF line highlighting the fundamental and first harmonic filtering.

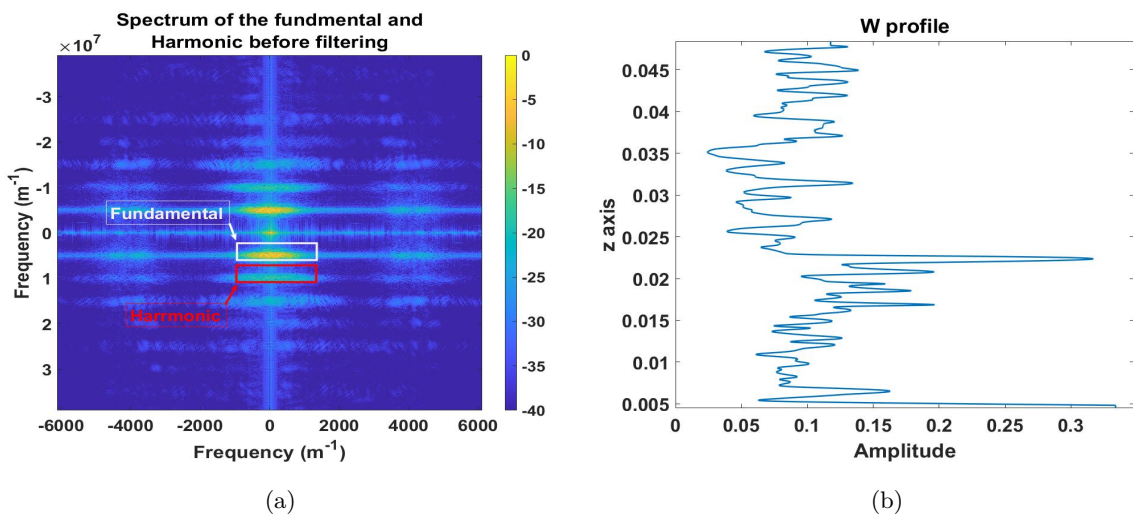


Figure 3.4: Example of weights for the carotid image: (a) Regions used to compute the energies of the fundamental (red) and harmonic (blue) spectra, (b) Diagonal elements of \mathbf{W} with respect to the axial direction.

3.6.3 Quantitative metrics

To evaluate quantitatively the accuracy of the deconvolution results, five metrics were employed. Two of these metrics are only applied to the simulated data because they require the knowledge of the ground truth TRF. The three other metrics are dedicated to experimental data, for which the true TRF is not available.

- **Structural Similarity (SSIM)**

The SSIM is an image quality measure taking into account human visual perception defined as [WBSS04]:

$$\text{SSIM} = \frac{(2\mu_x\mu_{\hat{x}} + c_1)(2\sigma_{x\hat{x}} + c_2)}{(\mu_x^2 + \mu_{\hat{x}}^2 + c_1)(\sigma_x^2 + \sigma_{\hat{x}}^2 + c_2)}, \quad (3.20)$$

where μ_x , $\mu_{\hat{x}}$, σ_x and $\sigma_{\hat{x}}$ are the means and standard deviations of the true image \mathbf{x} and its reconstruction $\hat{\mathbf{x}}$ (obtained using restoration or beamforming) and $\sigma_{x\hat{x}}$ is the covariance between \mathbf{x} and $\hat{\mathbf{x}}$. The values of c_1 and c_2 were set to the default values used in SSIM: $c_1 = (0.01 \times L)^2$ and $c_2 = (0.03 \times L)^2$, where L is the dynamic range.

- **The Root Mean Square Error (RMSE)** The root mean square error between a vectorized image \mathbf{x} and its reconstruction $\hat{\mathbf{x}}$ (obtained using restoration or beamforming) is defined as:

$$\text{RMSE} = \sqrt{\|\mathbf{x} - \hat{\mathbf{x}}\|_2^2}. \quad (3.21)$$

- **The Contrast-to-Noise Ratio (CNR)** The CNR defines the contrast level between two regions extracted from an image in dB:

$$\text{CNR} = 10 \log_{10} \left(\frac{|\mu_1 - \mu_2|}{\sqrt{\sigma_1^2 + \sigma_2^2}} \right), \quad (3.22)$$

where μ_1 and μ_2 are the means of pixels located in the two defined regions, and σ_1 and σ_2 are the standard deviations of these regions.

- **The Resolution Gain (RG)** The RG is measured based on the normalized autocorrelation function before and after deconvolution. The number of pixels of the normalized autocorrelation function having values higher than 0.75 (3dB) was counted in the original and the deconvolved images. The resolution gain is defined as the ratio between these two numbers, as suggested in [YZX12a].

3.7 Results and discussion

The accuracy of the proposed restoration algorithm was evaluated and compared to two existing state-of-the-art methods. The first method consists in restoring the TRF from the fundamental RF image only, without accounting for the first harmonic data. This approach (referred to as ‘‘LASSO-fundamental’’) estimates the TRF by minimizing the following LASSO-type cost function [ZAI03, TJ04]:

$$\min_r \frac{1}{2} \|\mathbf{y}_f - \mathbf{H}_f \mathbf{x}\|_2^2 + \mu \|\mathbf{x}\|_1. \quad (3.23)$$

Note that similarly to the proposed algorithms, the ℓ_1 -norm regularization is used in order to allow a fair comparison.

The second approach takes into consideration both fundamental and harmonic RF images as in [TJ04]. It sums the TRF estimated by (3.23) and the TRF estimated from the harmonic RF image using the following problem:

$$\min_{\mathbf{x}} \frac{1}{2} \|\mathbf{y}_h - \mathbf{H}_h \mathbf{x}\|_2^2 + \mu \|\mathbf{x}\|_1. \quad (3.24)$$

The final RF estimator (referred to as ‘‘LASSO-sum’’ in this work and as compounded estimator in [TJ04]) is obtained by pixel-wise summation of the two restored TRFs, normalized such that the pixels of the final TRF sums to 1. Finally, the proposed approach will be also compared to an estimator based on (3.24) only, referred to as ‘‘LASSO-harmonic’’, in order to appreciate the interest of the harmonic image. Note that the LASSO problem is very common and can be solved using several optimization algorithms, as suggested in the literature [BPC⁺11, KKL⁺07]. In order to obtain a fair comparison with the proposed algorithm, ADMM was also used to minimize the functions in (3.23) and (3.24).

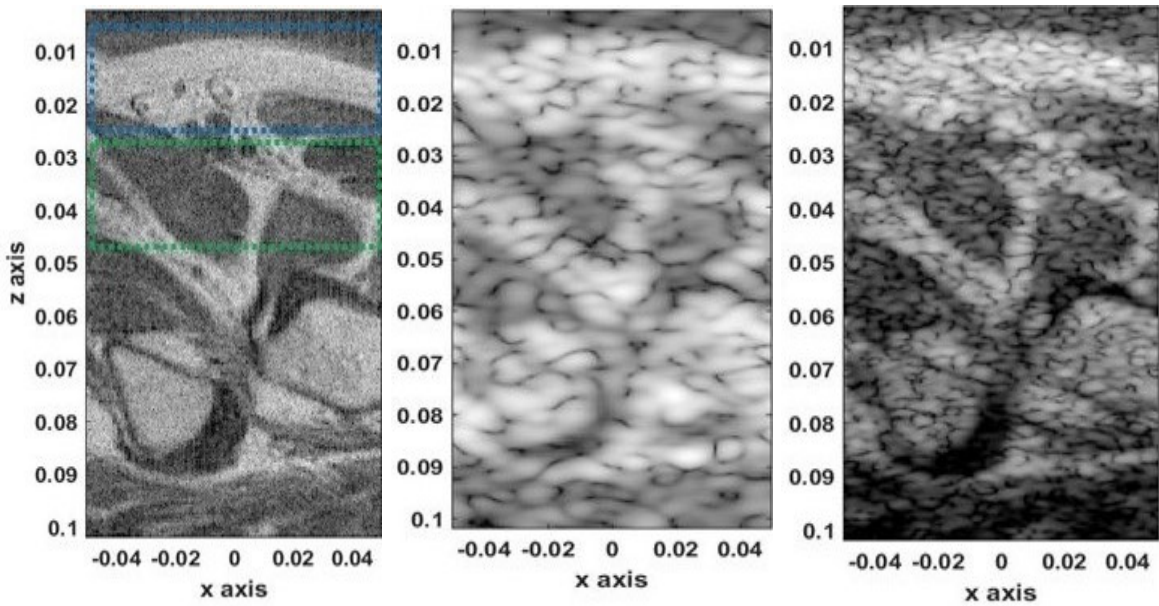
3.7.1 Results on synthetic data

Two kinds of results are presented in this section to compare the proposed method with LASSO-fundamental, LASSO-harmonic, and LASSO-sum. Firstly, results will be presented in a supervised approach where the same PSF is used for the generation and the restoration of the images. Secondly, the joint deconvolution with estimated PSF is adopted to mimic the practical cases where the PSF is estimated from the data before restoration.

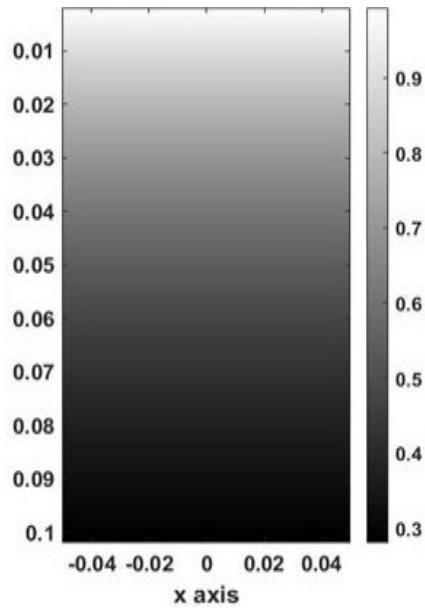
3.7.1.1 Supervised approach

The simulated TRF and the corresponding fundamental and harmonic images are shown in Figure 3.5 (a-c). Figure 3.5 (d) shows the exponential attenuation map W , used to simulate the harmonic image, which decays from 1 to 0.3 with the imaging depth following (3.19). The original and estimated TRFs obtained using the different methods are displayed in Figure 3.6. Zooms corresponding to the red rectangles are also displayed in Figure 3.6 for better visualization. The visual inspection of the TRF allows us to appreciate qualitatively the better accuracy of the proposed method in terms of contrast and resolution. A quantitative assessment is provided in Table 3.1 confirming the qualitative results.

Note that the resolution gain (RG) is computed both with respect to fundamental and harmonic images, defined as "RG/fund" and "RG/har". More specifically, the proposed method yields a good compromise between the fundamental image and the good spatial resolution of the harmonic image, with the ability of compensating the high harmonic attenuation with depth.

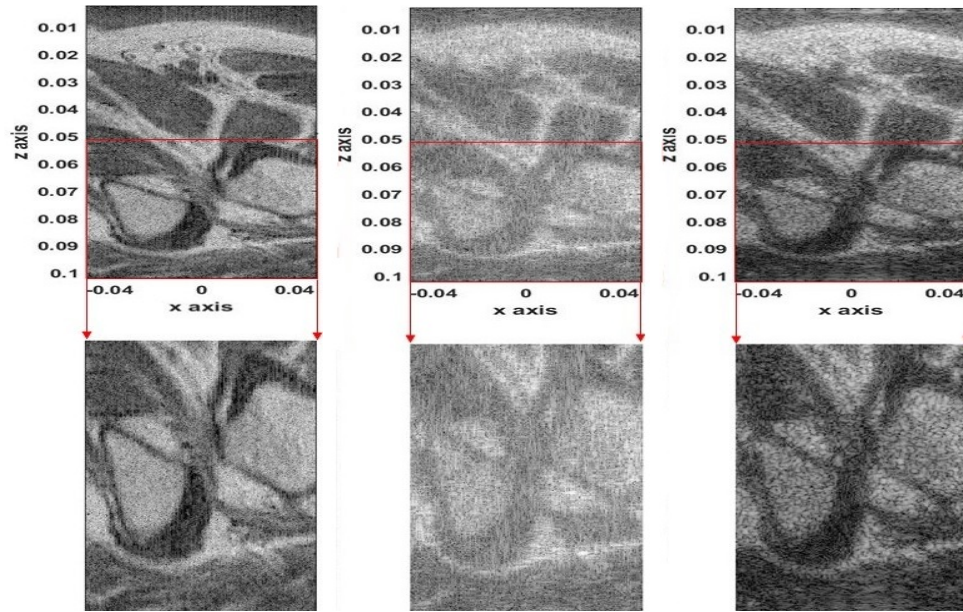


(a) Tissue reflectivity function (b) Fundamental B-mode image (c) Harmonic B-mode image

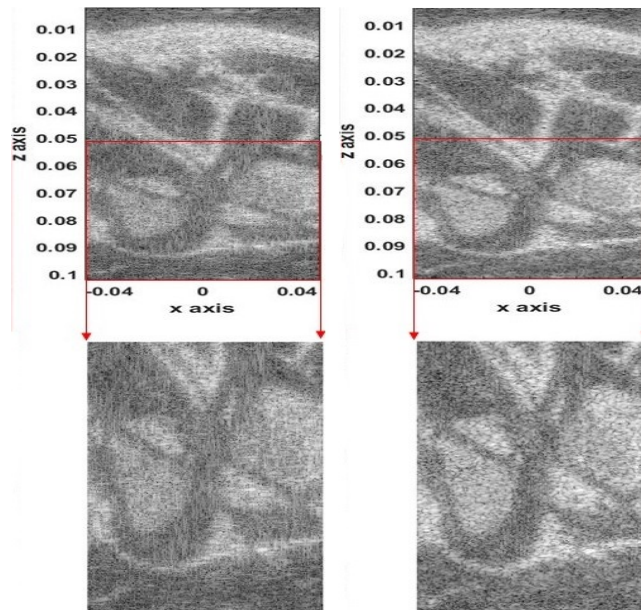


(d) Attenuation map

Figure 3.5: (a) TRF mimicking a human kidney (\mathbf{r} of size 1150×300 pixels), (b) simulated fundamental image \mathbf{y}_f , (c) simulated harmonic image \mathbf{y}_h , (d) attenuation map used to simulate the harmonic image in (b), whose values are equal to 1 (no attenuation) close to the probe and to 0.3 (high attenuation) at the bottom of the image. Note that all the images are shown in B-mode for better visualisation and with 60 dB dynamic range.



(a) Tissue reflectivity function (b) LASSO fundamental (c) LASSO harmonic



(d) LASSO sum (e) Joint solution

Figure 3.6: (a) TRF mimicking a human kidney (\mathbf{r} of size 1150×300 pixels), TRF estimated by (b) LASSO-fundamental, (c) LASSO-harmonic, (d) LASSO-sum and (e) proposed method. All the estimated TRFs are obtained using a supervised approach, i.e., using the true PSF. Note that all the images are shown in B-mode for better visualisation and with 60 dB dynamic range.

	LASSO Fundamental	LASSO Harmonic	LASSO Sum	Proposed method
CNR (dB)	-0.931	-5.874	-0.857	1.859
SSIM (%)	47	53.2	55.35	57.9
RMSE	1.031	1.110	1.010	0.685
RG/fund	63	63	63	63
RG/har	25	25	25	25

Table 3.1: Quantitative results corresponding to the images Figure 3.6(b),(c),(d) and (e). The CNR is computed with respect to the rectangular regions shown in Figure 3.5.

3.7.1.2 Joint deconvolution with pre-estimated PSF approach

The proposed method is evaluated using two sets of synthetic data by estimating both PSFs and the TRF successively. This experiment estimates the PSFs using the fundamental and harmonic images through the homomorphic filtering detailed in [MA05]. This is performed prior to the TRF restoration process.

- Results on kidney phantom image:

The first set of data is obtained using the synthetic data of kidney phantom. The results are displayed in Figure 3.7. One can observe that the deconvolution is less accurate than in the supervised case because the PSFs are estimated and not set to their true values. However, the proposed method provides very competitive results compared to the state-of-the-art. Quantitative results corresponding to this experiment are provided in Table 3.2, confirming the interest of the proposed method: The proposed methods and LASSO harmonic present the highest score in resolution gain, which proves the impact of considering the harmonic images in the restoration in terms of resolution. In addition, the proposed method presents the highest scores in terms of CNR, SSIM and RMSE.

In order to investigate the efficiency of PSF estimation, the true fundamental and harmonic PSF,

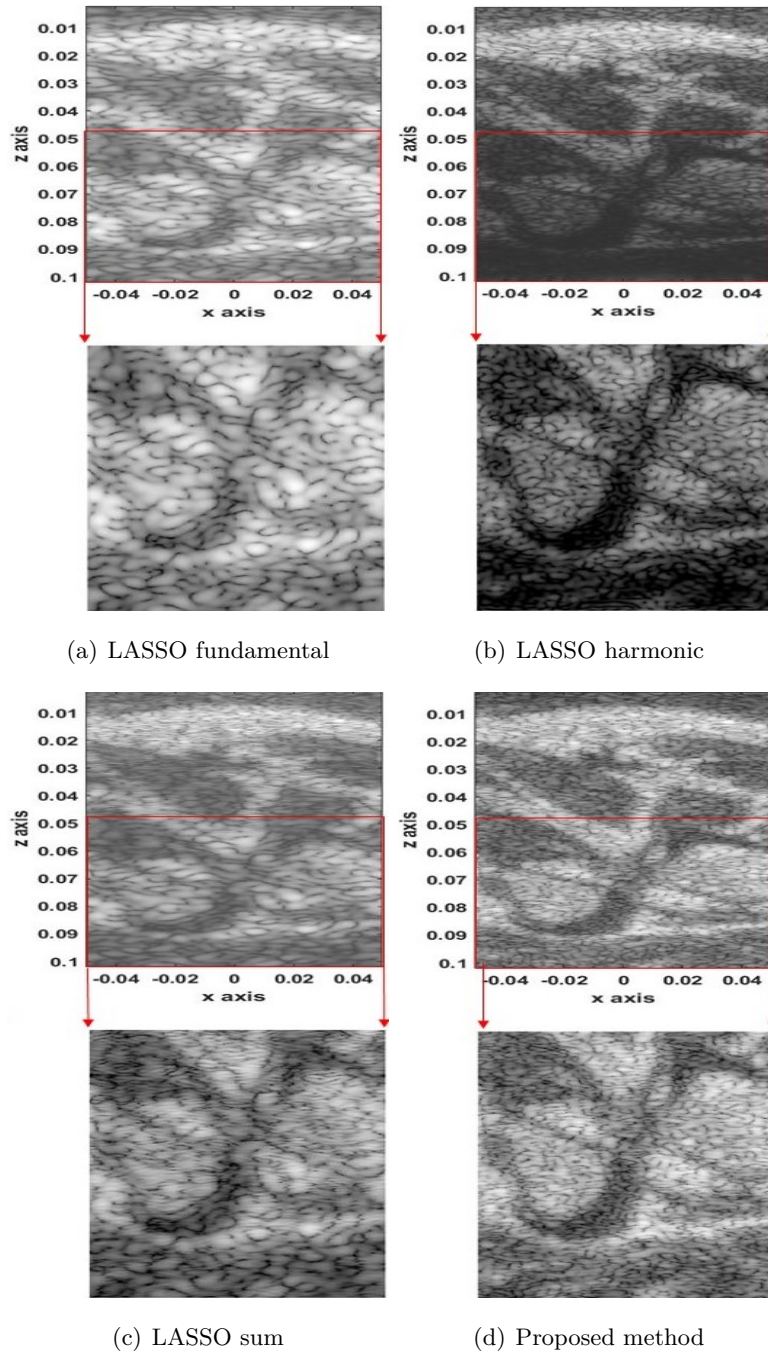


Figure 3.7: Estimated TRF using the joint deconvolution with pre-estimated PSF: (a) LASSO-fundamental estimated from the fundamental image in Figure 3.5 (b), (b) LASSO-harmonic estimated from the harmonic image in Figure 3.5(c), (c) LASSO-sum and (d) proposed method. All the TRF were estimated using PSF pre-estimated by homomorphic filtering of the RF images. Note that all the images are shown in B-mode for better visualisation and with 60 dB dynamic range.

	LASSO Fundamental	LASSO Harmonic	LASSO Sum	Proposed method
CNR	3.067	3.061	3.231	5.254
SSIM (%)	43.63	44.15	40.05	49.79
RMSE	1.334	0.911	0.1309	0.0783
RG/fund	2.739	9	3.571	9
RG/har	1.087	3.571	2.027	3.571

Table 3.2: Quantitative results corresponding to the images of Figure 3.7.

and the estimates obtained by the pre-processing (homomorphic filtering) step are shown in Figure 3.8. Besides the visual assessment, Table 3.3 confirms a good similarity, in the sense of RMSE, between the actual PSF and its estimate.

	PSF in Figure 3.8(c)	PSF in Figure 3.8(d)
SSIM	0.9976	0.9981
RMSE	0.1511	0.2022

Table 3.3: Quantitative assessment of the estimated PSF with respect to the true PSF.

- Results on the fetus image:

The interest of the proposed method for short excitation pulses and in the presence of non-linear propagation affects can be appreciated in Figure 3.9 for a fetus image simulated with CREANUIS [VBTC13]. Results reported in Table 3.4, confirm the visual interpretation: the proposed method yields the highest resolution gain among all the restoration methods and the second best CNR after LASSO-harmonic, which misses however the information in depth because of attenuation.

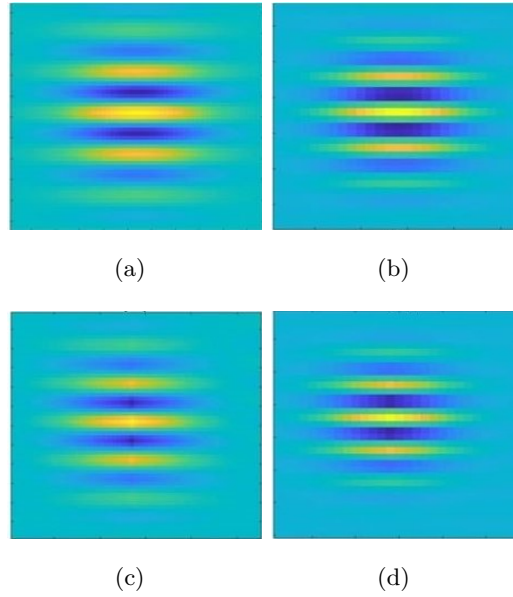


Figure 3.8: Left column shows the fundamental PSF: (a) true, (c) estimated by homomorphic filtering. Right column shows the harmonic PSF: (b) true, (d) estimated by homomorphic filtering.

	LASSO Fundamental	LASSO Harmonic	LASSO Sum	Proposed method
CNR	12.162	12.928	12.388	12.617
RG/fund	1.235	2.333	1.909	3
RG/har	0.629	1.101	0.818	1.286

Table 3.4: Quantitative results corresponding to the images of Figure 3.9.

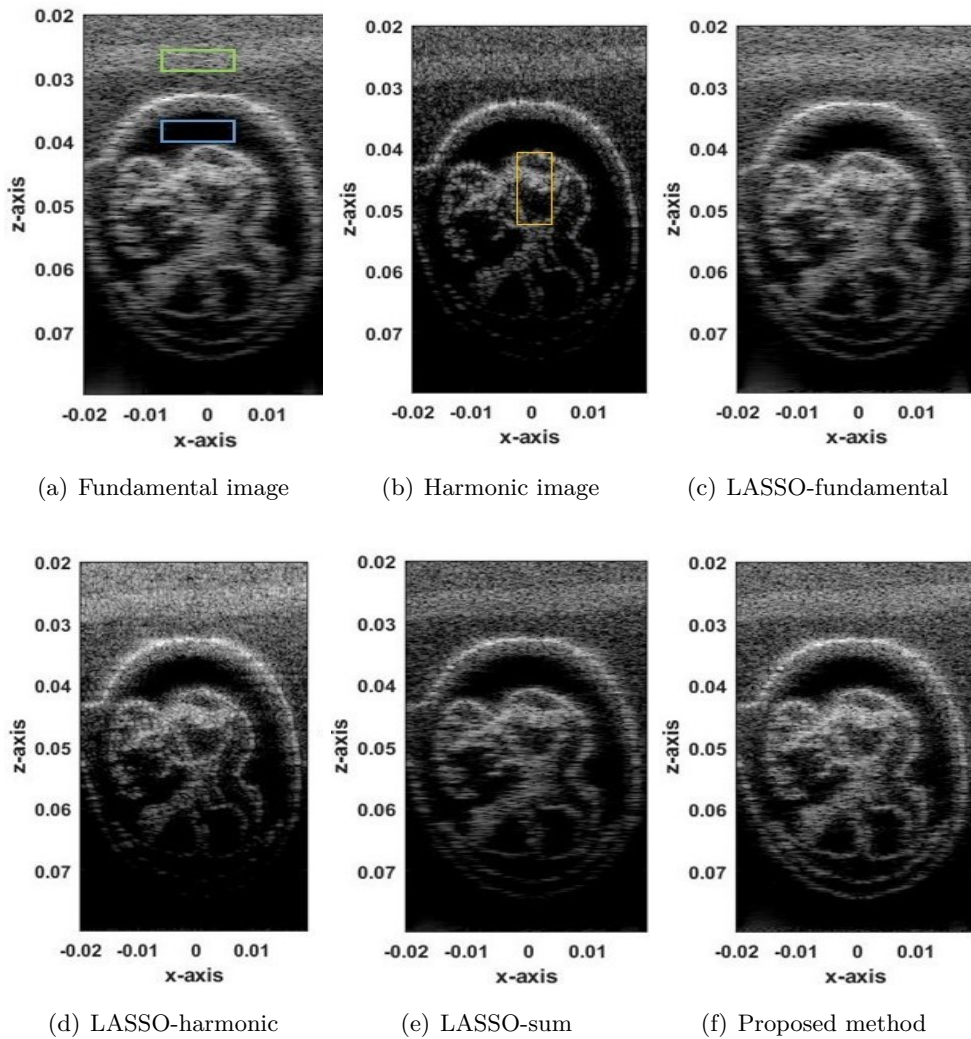


Figure 3.9: Results on data simulated with CREANUIS: (a) Fundamental image (blue and green regions are used to compute the CNR), (b) harmonic image (yellow region is used to compute the RG), TRF estimated by (c) LASSO-fundamental, (d) LASSO-harmonic, (e) LASSO-sum, and (f) the proposed method. All the TRF were restored using a PSF pre-estimated by homomorphic filtering. Note that all the images are shown in B-mode for better visualisation and with 60 dB dynamic range.

3.7.2 Results on phantom and real images

This subsection analyzes some results obtained using phantom and real carotid data. In contrast to the simulated data, the system PSFs are unknown in these scenarios and have to be estimated. Therefore, we investigate a PSF pre-estimation using homomorphic filtering followed by a TRF deconvolution.

3.7.2.1 Phantom image

The fundamental and harmonic images associated with the considered phantom are shown in Figure 3.10 (a, b). The better spatial resolution enabled by harmonic images can be clearly observed by the wire responses. The attenuation of harmonic echoes is very low for this example. For this reason, the matrix \mathbf{W} accounting for attenuation in the harmonic direct model was set to the identity matrix. The results using the proposed approach and the different restoration methods are shown in Figure 3.10 (c-f). In general, all the restoration methods that consider the harmonic data (LASSO-harmonic, LASSO-sum, and proposed method) exhibit good spatial resolution. Furthermore, LASSO-sum and the proposed algorithm compensate the harmonic attenuation at high depths by including information from the fundamental image, as shown in the zooms of Figure 3.10. Cysts are also better defined in the restored images compared to the noisy images. To confirm these remarks, a plot extracted from the estimated TRF is shown in Figure 3.11. The proposed method provides images with good spatial resolution, *i.e.*, with a similar or better full width at half maximum of the wire echo compared to harmonic and fundamental images.

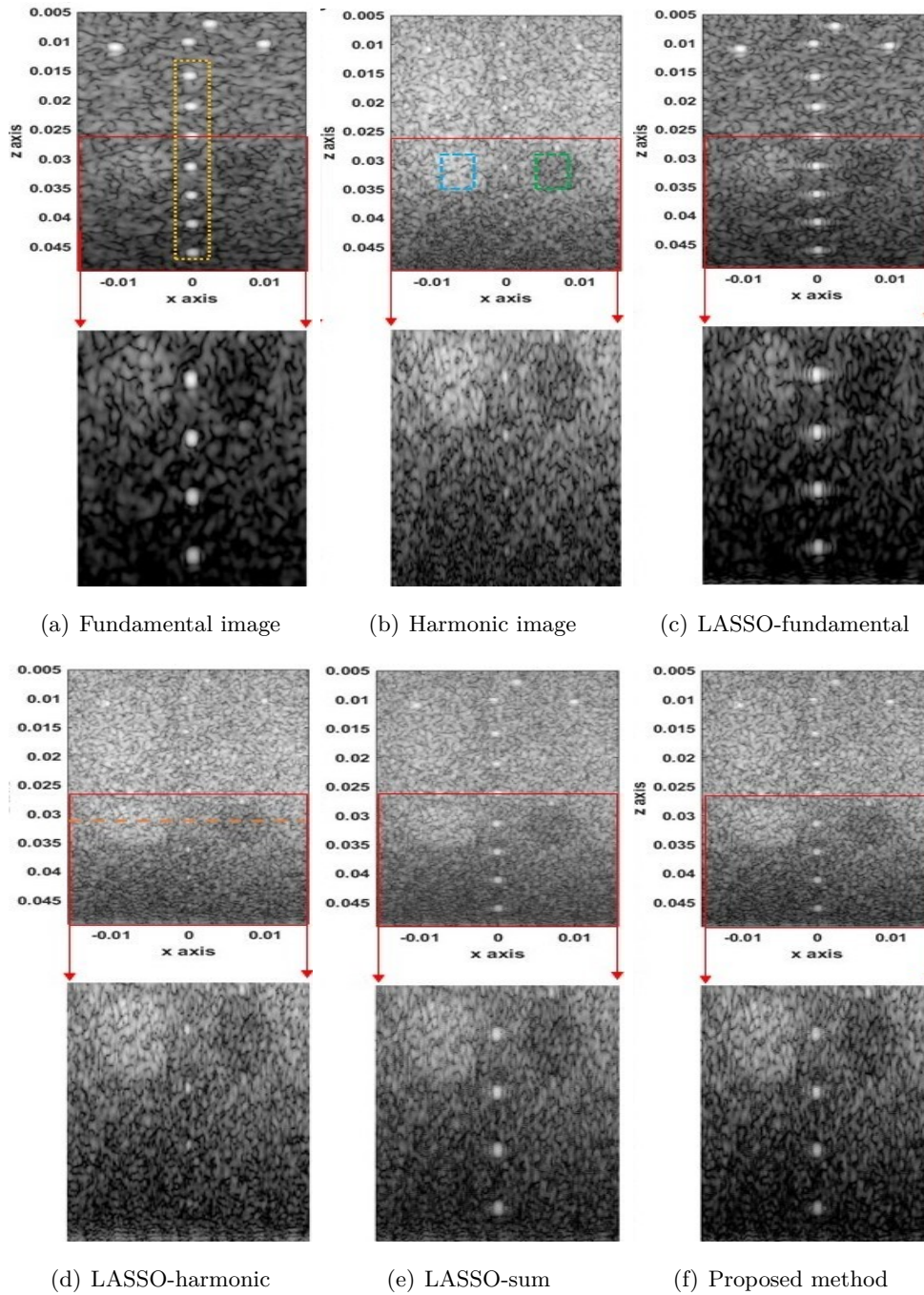


Figure 3.10: Results on phantom data: (a) Fundamental image (yellow region is used to compute the RG), (b) harmonic image (blue and green regions are used to compute the CNR), TRF estimated by (c) LASSO-fundamental, (d) LASSO-harmonic, (e) LASSO-sum, and (f) proposed method. All the TRF were restored using a PSF pre-estimated by homomorphic filtering. Note that all the images are shown in B-mode for better visualisation and with 60 dB dynamic range.

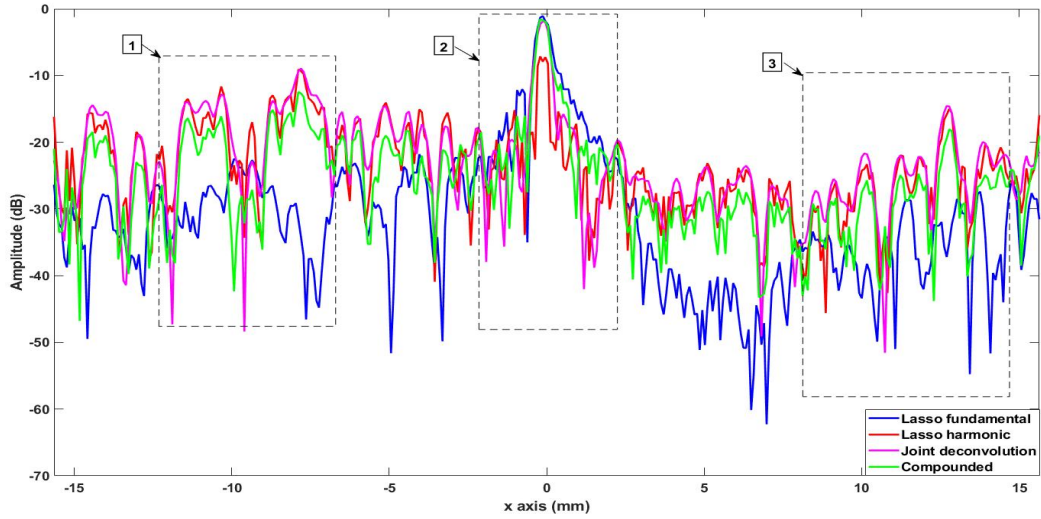


Figure 3.11: Horizontal profile passing by the two cysts (regions 1 and 3) and the wire in between (region 2), the orange line in Figure 3.10.(d).

Quantitative results are provided in Table 3.5. They show on one hand the competitiveness of the proposed method both in terms of contrast and spatial resolution, and on the other hand that slightly better results are obtained, for all the methods, with the PSF estimated in a pre-processing step.

	LASSO Fundamental	LASSO Harmonic	LASSO Sum	Proposed method
CNR	0.469	1.686	1.494	2.417
RG/fund	2.778	3.154	3.545	6.231
RG/har	2.231	2.333	2.231	2.636

Table 3.5: Quantitative results computed from the images of Figure 3.10.

3.7.2.2 Carotid results

The fundamental and harmonic carotid images are shown in Figure 3.12 (a, b). From these images, one can clearly observe the better spatial resolution of the harmonic image, at the cost of higher attenuation with depth compared to the fundamental image. In contrast to the phantom experiment, the attenuation matrix \mathbf{W} was estimated as explained in Section 3.6.2. This matrix has a crucial role for this dataset, due to its ability to balance fundamental and harmonic information. The experiments on carotid are following the same scheme as for the phantom. Results displayed in Figure 3.12 allow us to conclude that LASSO-sum and the proposed method, which use both fundamental and harmonic images, are able to gather useful information from both observations. In particular, they provide a spatial resolution similar to that of the harmonic image. However, harmonic images are highly attenuated with depth, and more generally can be attenuated in any region corresponding to tissues with a high harmonic response. For those particular regions, the fundamental image plays an important role in order to compensate for this lack of information in the harmonic image. This effect can be appreciated in the zoomed regions shown in Figure 3.12. Figure 3.13 shows profiles extracted from the TRF confirming these observations. Quantitative results are provided in Table 3.6, which highlights the interest of combining information from both fundamental and harmonic RF images. For this particular carotid experiment, one can observe that the harmonic image has a relatively strong amplitude for small depths, thus providing a very good spatial resolution and contrast, except for high depths. In particular, the CNR measured from the harmonic image is very high. However, one can observe that all the deconvolution methods allow spatial resolution to be increased, highlighted by RG values always higher than 1 in Table 3.6. The proposed method reaches a compromise between spatial resolution (best compared to fundamental image and second best, hence very close to the best, compared to the harmonic image) and contrast (best CNR among all the deconvolution methods and close to the harmonic image).

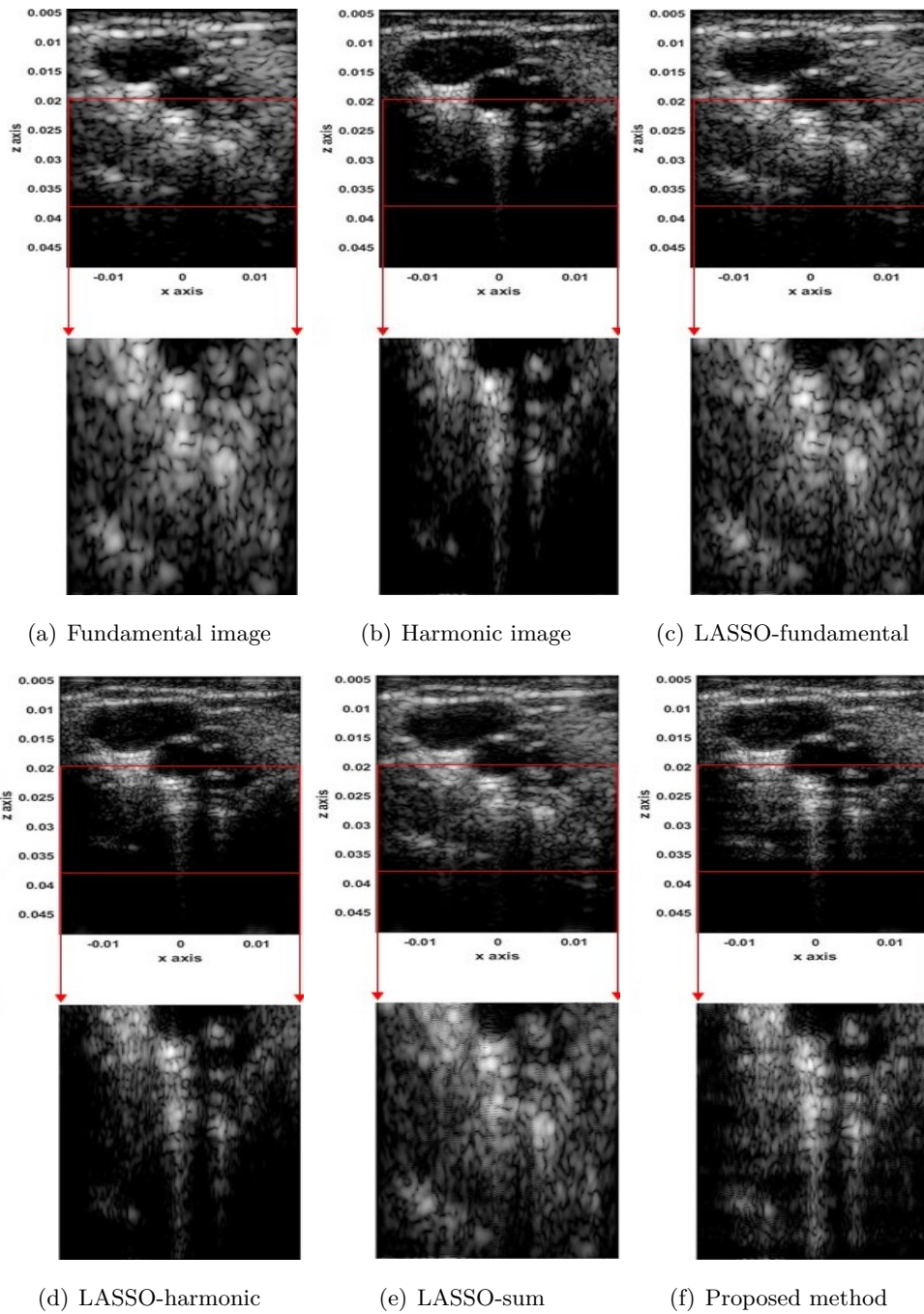


Figure 3.12: Results on carotid data: (a) Fundamental image (green region is used to compute the RG), (b) harmonic image (blue regions are used to compute the CNR), TRF estimated by (c) LASSO-fundamental, (d) LASSO-harmonic, (e) LASSO-sum, and (f) proposed method. All the TRF were restored using PSF pre-estimated by homomorphic filtering. Note that all the images are shown in B-mode for better visualisation and with 60 dB dynamic range

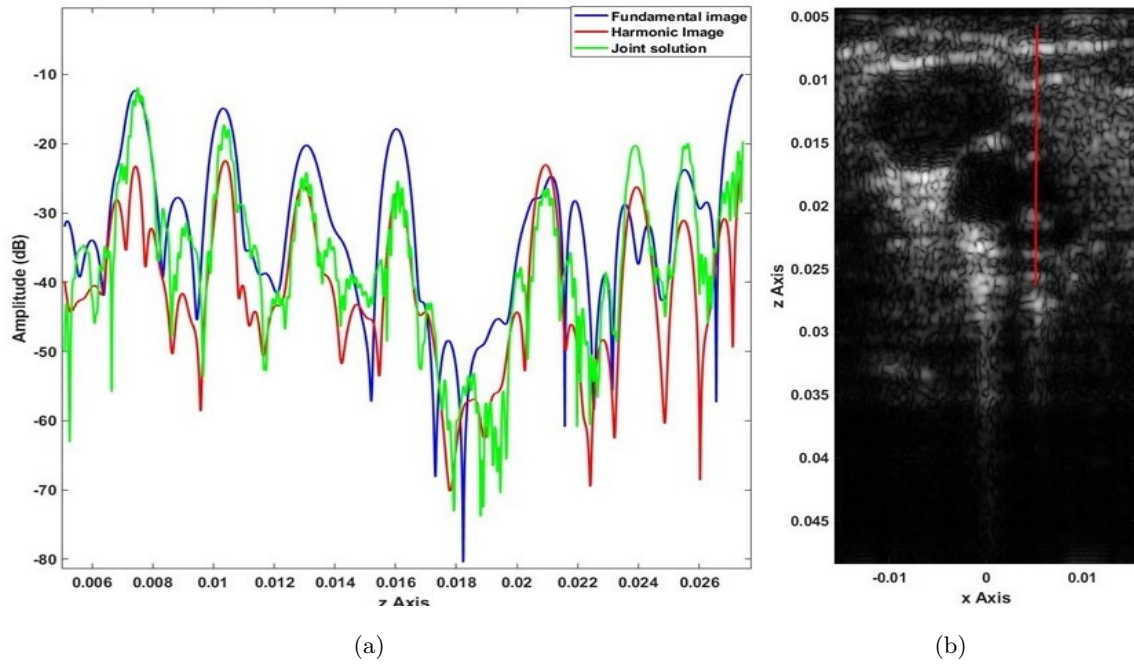


Figure 3.13: (a) TRF profiles corresponding to the red line in (b).

	LASSO Fundamental	LASSO Harmonic	LASSO sum	Proposed method
CNR	9.832	13.438	8.38	12.069
RG/fund	2.226	5.308	8.513	9.857
RG/har	1.194	2.846	5.882	5.286

Table 3.6: Quantitative results computed from the images in Figure 3.12.

3.8 Discussion

The models used in this chapter for fundamental and harmonic components were linear based on the first order Born approximation. If this assumption is valid for fundamental images in most practical applications, it is only valid for harmonic images acquired from mediums with low nonlinearities. To extend the proposed work to other applications than THI, such as perfusion techniques, non-linear models should be considered to better fit the harmonic image formation model. The imaging formation models could be also improved by including spatially-variant PSFs, adapted to various imaging strategies such as the classical focus scheme used in this work or synthetic strategies based on plane or diverging waves. These more sophisticated models would certainly help to increase the accuracy of the image restoration process, e.g., by reducing the reverberation in the restored TRF images.

The blind deconvolution problem investigated in this work assumed that the noises of the fundamental and harmonic images are independent. Since the cross-correlation coefficient between the anechoic regions in the real data between the fundamental and harmonic images is close to zero, the latter assumption is considered fair enough in our application. Inverting the proposed image formation models for the fundamental and harmonic images is an ill-posed inverse problem that requires regularization to stabilize the solution. In the present work, the regularization term was based on an ℓ_1 -norm motivated by the assumption of a Laplacian-distributed TRF. However, other statistical models might be considered, e.g., using a generalized Gaussian distribution, which is more general than the Laplace distribution and was already shown to be a good candidate for US image restoration [ZBKT14, AMP⁺11]. Hence, this generality comes with an additional challenge of the appropriate choice of the shape parameter, or in other words of the choice of p in the ℓ_p -norm that replaces the ℓ_1 -norm in the Laplacian case. Hereafter, we provide a simulation result, in Figure 3.14, and Table 3.7, that compares the ℓ_1 -norm to ℓ_p -norm with $p = 3/2$ and $p = 4/3$ (that ensure analytical solutions for the proximal operator). One may remark that in this particular case the results are very similar, thus sustaining the choice of the ℓ_1 -norm in this work.

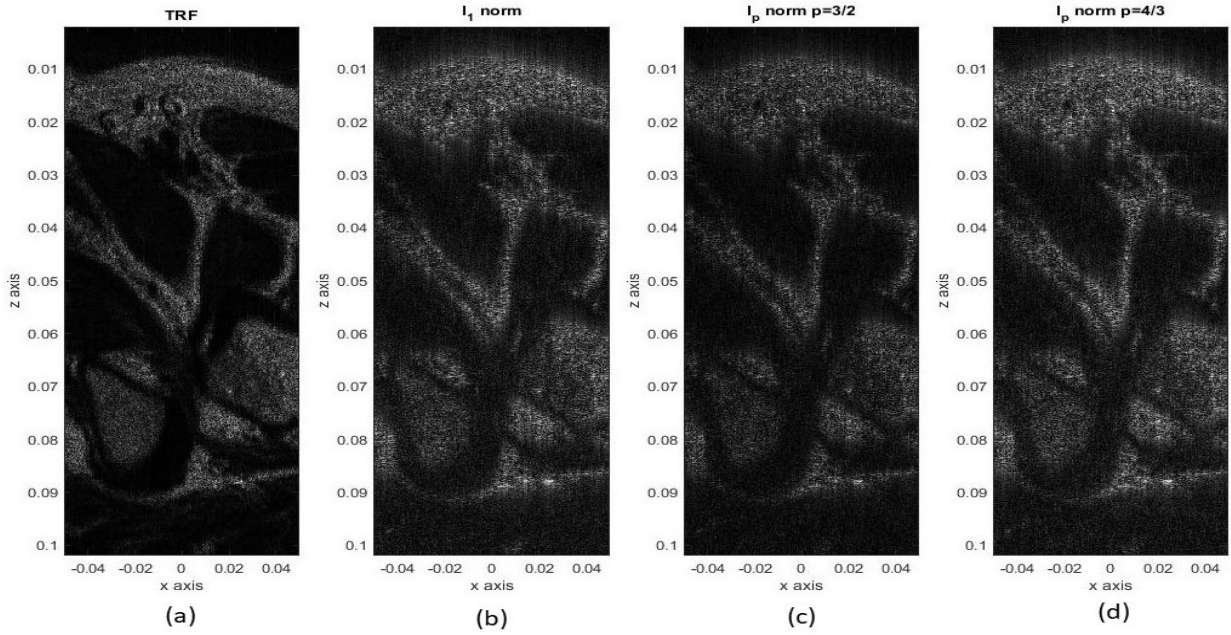


Figure 3.14: Simulation data (a) TRF, (b,c,d) joint solution with l_1 norm, l_p norm ($p=3/2$), l_p norm ($p=4/3$).

	l_1 norm	$l_{1.3}$ norm	$l_{1.5}$ norm
PSNR (dB)	21.22	18.48	20.11
RMSE	0.0868	0.1191	0.0987
SSIM (%)	58.1	38.8	51.2

Table 3.7: Quantitative results computed from the images in Figure 3.14 using SSIM, RMSE and PSNR.

It is interesting to mention here that the regularization parameters were fixed to their best values by cross-validation. Thus, the hyperparameter μ balances the weight between the data fidelity term and the l_1 -norm regularization promoting sparsity. The hyperparameter β is proper to ADMM and allows the convergence of the algorithm to be monitored. It balances the importance of the linear

constraint with respect to the data fidelity terms. Practically, the values of these hyperparameters were set to $\mu = 0.1$ and $\beta = 1$ for synthetic data (extracted from the cross-validation results in Figure 3.15 and 3.16 applied on the simulation data), and to $\mu = 0.05$ and $\beta = 0.5$ for the two real datasets (interestingly it was not necessary to change these values from one real dataset to another).

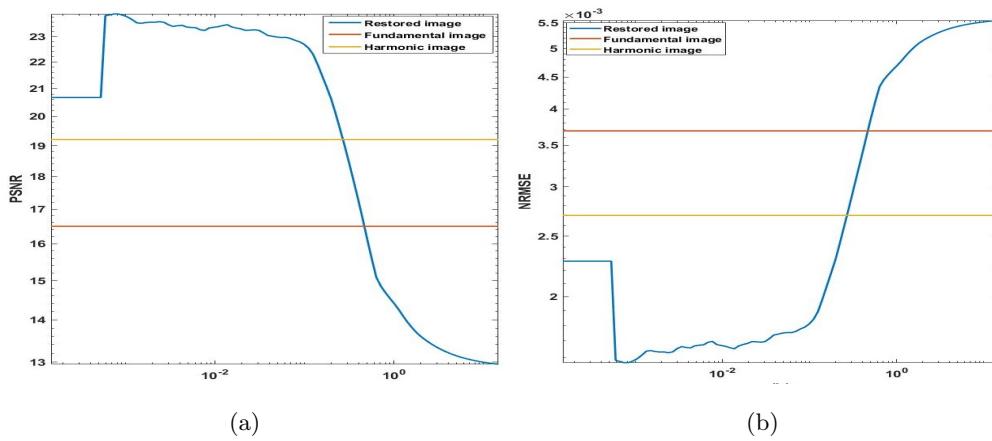


Figure 3.15: Illustration of the influence of the hyperparameter μ on the result in terms of (a) PSNR and (b) NRMSE.

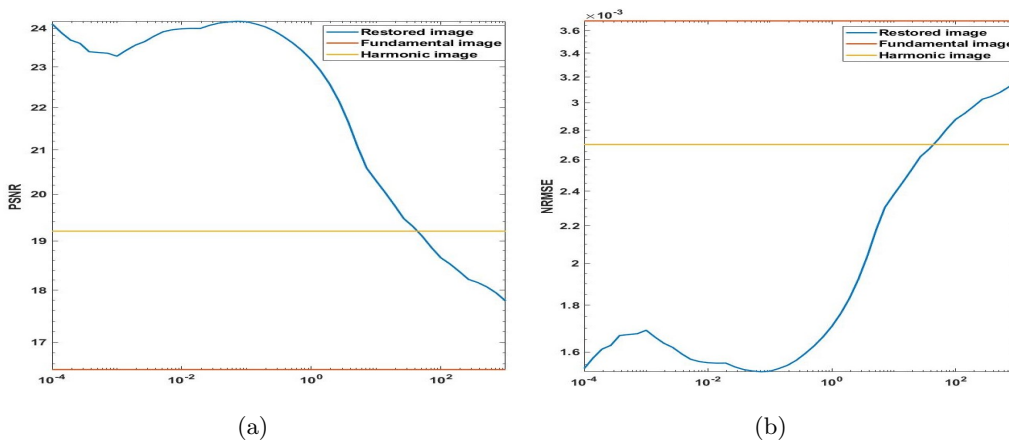


Figure 3.16: Illustration of the influence of the hyperparameter β on the result in terms of (a) PSNR and (b) NRMSE.

The execution time of the proposed deconvolution algorithm is about 1 minute for one ultrasound image, on a standard 3.6 GHz Intel Core i7 with a straightforward MATLAB implementation. The current implementation ¹ uses optimized ways of handling high dimensional operators, by computing some of the steps in the Fourier domain as explained previously.

3.9 Conclusion and perspectives

This chapter introduced a restoration method adapted to US imaging. Its main advantage compared to the state-of-the-art is to consider two image formation models for fundamental and harmonic images, that are used jointly in the restoration process. This strategy combines information from both RF images, in particular the good spatial resolution of harmonic data and the good SNR (especially for high depths) of fundamental data. An accurate knowledge of the PSF is an important prerequisite for any deconvolution method. In this chapter, the estimation of the PSFs was achieved in a pre-processing step, by homomorphic filtering. Considering a fully blind restoration will be presented in the following chapter. In order to simplify the problem, this chapter had considered a spatially invariant PSF. The spatial variability of the PSF will be considered in the following chapter. ADMM was adopted in the proposed work to minimize the cost function resulting from the US deconvolution process. Results on real and experimental medical ultrasound images confirmed the interest of the proposed approach.

¹The Matlab code is available at <https://www.irit.fr/~Adrian.Basarab/codes.html>.

CHAPTER 4

On the fully blind and block-wise joint restoration

Part of this chapter has been adapted from the conference proceedings [[HBM⁺20](#)], [[HBV⁺20](#)]

4.1 Introduction

In the previous chapter, a joint deconvolution algorithm using a pre-estimated PSF was introduced. Results on synthetic and real images were presented in order to prove the accuracy of the proposed algorithm and the interest of the PSF estimation and US deconvolution approach. Following these encouraging results, this chapter considers improving the previously proposed algorithm by taking into account two challenges related to the PSF. The first is its estimation from the data that was previously obtained within a pre-processing step. However, the estimation of the PSF and the deconvolved images are mutually dependent. Therefore, in this chapter, we introduce a deconvolution method that alternates between the estimation of the PSF and the deconvolved image, based on a recently proposed PSF estimation algorithm. The second challenge addressed is the spatial variability of the PSF. It is well known that the PSF in US imaging is spatially variant, especially in the US wave propagation direction. This variation represents an important issue for deconvolution algorithms accounting for spatially invariant PSF, as the one presented in the previous chapter. To mitigate this issue, we introduce in this chapter a block-wise restoration algorithm.

4.2 Fully blind joint deconvolution

After the solution presented in the previous chapter that considers the PSF estimation in a pre-processing step, this section proposes to estimate the PSF and TRF simultaneously. Some of the existing approaches have considered a parametric model that can reduce the computational complexity of the PSF estimation step. However, a further upgrade of the adopted PSF model is needed given the complexity of the PSF and its variations in real images. Most of the works around fully blind deconvolution approaches consider a non-parametric model for the PSF [YZX12a, JT08]. These methods require a prior information for the PSF. Following this trend, a recent hybrid method was proposed in the literature that considers the estimation of the amplitude of the PSF using homomorphic filtering, followed by an alternate estimation of the TRF and the phase of the PSF constrained by the estimated amplitude [MBK19]. This section follows another trend based on joint deconvolution of the fundamental and harmonic US images.

4.2.1 Problem reformulation

The objective here is to solve a blind restoration problem to estimate jointly the PSFs \mathbf{h}_f and \mathbf{h}_h and the TRF \mathbf{x} from the observed RF images \mathbf{y}_f and \mathbf{y}_h . Based on the model presented in (3.2) and (3.1), we express the joint blind deconvolution problem as the minimization of the following function:

$$\min_{\mathbf{x}, \mathbf{H}_f, \mathbf{H}_h} \frac{1}{2} \|\mathbf{y}_f - \mathbf{H}_f \mathbf{x}\|_2^2 + \frac{1}{2} \|\mathbf{y}_h - \mathbf{W} \mathbf{H}_h \mathbf{x}\|_2^2 + \mu \|\mathbf{x}\|_1, \quad (4.1)$$

where the first two terms represent the fundamental and harmonic image data fidelity terms, $\|\mathbf{x}\|_1$ is a regularization term and μ is a hyper-parameter controlling the weight of this regularization with respect to the two data fidelity terms. In this work, we consider a Laplacian prior distribution for the TRF, leading to an ℓ_1 -norm regularization in the function to minimize as in [MBBK13, CBK16b]. Moreover, \mathbf{H}_f and $\mathbf{H}_h \in \mathbb{R}^{N \times N}$ are BCCB matrices accounting for the fundamental and harmonic system PSFs reconstructed using the PSFs kernels \mathbf{h}_f and $\mathbf{h}_h \in \mathbb{R}^{p \times q}$ (see appendix A for more details about how to build a BCCB matrix from the associated PSF kernel).

4.2.2 Optimization algorithm

To solve the optimization problem in (4.1), we propose in this work an alternating minimization method that estimates sequentially the PSFs and the TRF (we recursively estimate one variable while the others are 'frozen' and this operation is conducted for all variables). However, the cost function in (4.1) is not jointly convex with respect to \mathbf{H}_f , \mathbf{H}_h and \mathbf{x} . To ensure the convergence towards a reliable solution, we add two constraints on the PSFs. Specifically, a partial information about the PSFs is added to constrain the problem: the magnitudes of the Fourier transform of \mathbf{h}_f and \mathbf{h}_h . Note that magnitudes of the PSFs can be easily estimated by denoising the cepstrum of the observed images [MA05]: The TRF function is assumed to be a white Gaussian noise in the cepstrum domain while the PSF is a regular smooth function. On the contrary, the estimation of the phase of the PSF cannot be performed easily [MA05]. Thus, in this work, we propose to estimate the phase of the Fourier transform of the PSFs as in [MBK19] while considering the amplitude of the Fourier transform of the fundamental and harmonic components of the PSFs as constraints. Taking into account these two constraints (for the fundamental and harmonic PSFs) the proposed optimization

algorithm alternates between sequential updates of the TRF and the PSFs as:

$$\mathbf{x} \in \min_{\mathbf{x}} \frac{1}{2} \|\mathbf{y}_f - \mathbf{H}_f \mathbf{x}\|_2^2 + \frac{1}{2} \|\mathbf{y}_h - \mathbf{W} \mathbf{H}_h \mathbf{x}\|_2^2 + \mu \|\mathbf{x}\|_1 \quad (4.2)$$

$$\mathbf{h}_f \in \min_{\mathbf{h}_f} \frac{1}{2} \|\mathbf{Y}_f - \mathbf{h}_f \circledast \mathbf{X}\|_2^2 \quad \text{s.t.} \quad |\mathcal{F}(\mathbf{h}_f)| = \widehat{\mathbf{h}}_f \quad (4.3)$$

$$\mathbf{h}_h \in \min_{\mathbf{h}_h} \frac{1}{2} \|\mathbf{Y}_h - \mathbf{h}_h \circledast \mathbf{X}\|_2^2 \quad \text{s.t.} \quad |\mathcal{F}(\mathbf{h}_h)| = \widehat{\mathbf{h}}_h. \quad (4.4)$$

where $\mathcal{F}(\cdot)$ is the 2D Fourier transform operator. Note that we keep the matrix-vector representation in (4.2) in order to keep the similarity with the representation in Chapter 3. The PSF estimations steps in (4.3) and (4.4) are expressed as a spatial convolution between the PSF kernels \mathbf{h}_f and $\mathbf{h}_h \in \mathbb{R}^{p \times q}$ with the TRF image $\mathbf{X} \in \mathbb{R}^{m \times n}$. We note that $\mathbf{x} \in \mathbb{R}^N$, $\mathbf{y}_f \in \mathbb{R}^N$ are the vectorized version of $\mathbf{X} \in \mathbb{R}^{m \times n}$ and $\mathbf{Y}_f \in \mathbb{R}^{m \times n}$ respectively (with $N = m \times n$, see Appendix A). In order to consider the attenuation in (4.4), $\mathbf{Y}_h \in \mathbb{R}^{m \times n}$ is considered as the resized version of the vector $\mathbf{W}^{-1} \mathbf{y}_h \in \mathbb{R}^N$. Finally, note that $\widehat{\mathbf{h}}_f$ and $\widehat{\mathbf{h}}_h$ are the Fourier transform magnitudes of the PSFs, which are estimated by denoising the cepstrum of \mathbf{Y}_f and \mathbf{Y}_h [MA05].

4.2.2.1 TRF estimation

The TRF estimation step (4.2) can be solved using the solution presented in Chapter 3 (see Algorithm 1).

4.2.2.2 PSF estimation

The minimization problems in (4.3) and (4.4) aim at estimating the phases of the PSFs. Therefore, the recently proposed method in [MBK19], inspired from [PS94] was adopted to estimate the PSF's phase. Applying Parseval theorem, (4.3) and (4.4) can be expressed as:

$$\min_{\mathcal{H}_f} \frac{1}{2} \|\mathcal{Y}_f - \mathcal{H}_f \cdot \mathcal{X}\|_2^2 \quad \text{s.t.} \quad |\mathcal{H}_f| = \widehat{\mathbf{h}}_f, \quad (4.5)$$

$$\min_{\mathcal{H}_h} \frac{1}{2} \|\mathcal{Y}_h - \mathcal{H}_h \cdot \mathcal{X}\|_2^2 \quad \text{s.t.} \quad |\mathcal{H}_h| = \widehat{\mathbf{h}}_h, \quad (4.6)$$

where (\cdot) denotes element wise multiplication, $\mathcal{X} = \mathcal{F}(\mathbf{x}^*)$, $\mathcal{H}_i = \mathcal{F}(\mathbf{h}_i)$, $\mathcal{Y}_f = \mathcal{F}(\mathbf{y}_f)$ and $\mathcal{Y}_h = \mathcal{F}(\mathbf{y}_h)$. Using $\mathcal{H}_i = \widehat{\mathbf{h}}_i \cdot e^{j\angle \mathcal{H}_i} = \widehat{\mathbf{h}}_i \cdot U_i$, the previous equations can be rewritten as follows:

$$\min_{U_f} \frac{1}{2} \|\mathcal{Y}_f - (\mathcal{X} \cdot \widehat{\mathbf{h}}_f) \cdot U_f\|_2^2 \quad (4.7)$$

$$\min_{U_h} \frac{1}{2} \|\mathcal{Y}_h - (\mathcal{X} \cdot \widehat{\mathbf{h}}_h) \cdot U_h\|_2^2. \quad (4.8)$$

Note that the minimizations in (4.7) and (4.8) are conducted with respect to the phase vectors U_f and U_h . This reformulation shows that the PSF estimation problems are reduced to estimating the optimal phases of the all-pass filters U_f and U_h . The reader may refer to [MBK19] for details about the algorithm able to solve the two problems above. The resulting alternating minimization proposed in this chapter is summarized in Algorithm 2 where in the first iteration, the estimation of the TRF is done with the zero-phase PSF, *i.e.*, the magnitude of the PSFs estimated by homomorphic filtering.

Algorithm 2: ADMM algorithm for blind restoration

Input: $\mathbf{y}_f, \mathbf{y}_h, \widehat{\mathbf{h}}_f, \widehat{\mathbf{h}}_h$

1. Set $k = 0$, choose $\mu > 0, \beta > 0, u^0, v^0$

2. Repeat until stopping criterion is satisfied

// Estimate \mathbf{x} using Algorithm 1

3. $\mathbf{x} \leftarrow \arg \min_{\mathbf{x}} \frac{1}{2} \|\mathbf{y}_f - \mathbf{H}_f \mathbf{x}\|_2^2 + \frac{1}{2} \|\mathbf{y}_h - \mathbf{W} \mathbf{H}_h \mathbf{x}\|_2^2 + \mu \|\mathbf{x}\|_1$

// Fundamental PSF estimation

4. $U_f \leftarrow \arg \min_{U_f} \frac{1}{2} \|\mathcal{Y}_f - (\mathcal{X} \cdot \widehat{\mathbf{h}}_f) \cdot U_f\|_2^2$

// Harmonic PSF estimation

5. $U_h \leftarrow \arg \min_{U_h} \frac{1}{2} \|\mathcal{Y}_h - (\mathcal{X} \cdot \widehat{\mathbf{h}}_h) \cdot U_h\|_2^2$

Output: $\mathbf{x}, \mathbf{h}_f = \mathcal{F}^{-1}(\widehat{\mathbf{h}}_f \cdot U_f), \mathbf{h}_h = \mathcal{F}^{-1}(\widehat{\mathbf{h}}_h \cdot U_h)$.

4.2.3 Results

Three series of results are presented in this section to compare the proposed method with the blind restoration method used for LASSO-fundamental, LASSO-harmonic and LASSO-sum (see Section

3.7). A further comparison with the joint blind deconvolution with pre-estimated PSF will be presented in the discussion section. We recall here that the LASSO-fundamental and LASSO-harmonic are TRF estimators based on one image modality (fundamental and harmonic image respectively). The LASSO-sum method, presented in [TJ04], applies a compounding solution by applying a pixel by pixel summation of the restored images for the previously cited modalities. Thus, the latter approach aims to improve the resolution of the restored image thanks to the harmonic image. We notice that all the presented results and the so-called proposed method are fully blind deconvolution approaches.

4.2.3.1 Simulated image

In this subsection, the proposed method is applied to a simulated kidney image. The ground truth as well as the fundamental, harmonic image and the attenuation map are shown in Figure 4.1. Results are presented in Figure 4.2 and assessed quantitatively in Table 4.1. One can see that the proposed method presents a good resolution and contrast while mitigating the attenuation of depth. Quantitatively, the proposed method presents the highest scores of SSIM, CNR and RMSE compared to the ground truth. Also, it presents the second highest score of resolution gain. In addition, one can see in the cropped area in Figure 4.2 (d) a good definition of the anatomical edges thanks to the previous cited enhancement, and mainly the ability of the proposed method to overcome the attenuation effect existing in the US harmonic image. This proves that this approach is able to reconstruct a US image with a good compromise between resolution, and contrast in one image. We notice here that the same regions used for computing the RG and CNR in the previous chapter were used. As explained previously, the main difference between the two blind approaches presented in this thesis is the strategy applied in order to estimate the PSFs from the RF images. The true fundamental and harmonic PSF, the pre-estimated ones following the method presented in Chapter 3 and the PSFs estimated by the proposed algorithm are shown in Figure 4.3. One can see that the PSFs estimated in a pre-processing step are slightly better than those estimated with the fully blind approach when compared to the ground truth PSFs (see Table 4.2). However, the scores of both approaches are considered satisfying (around 90 % of similarity with the ground truth). We can explain this difference by the fact that the simulated PSFs are not complicated in their structure

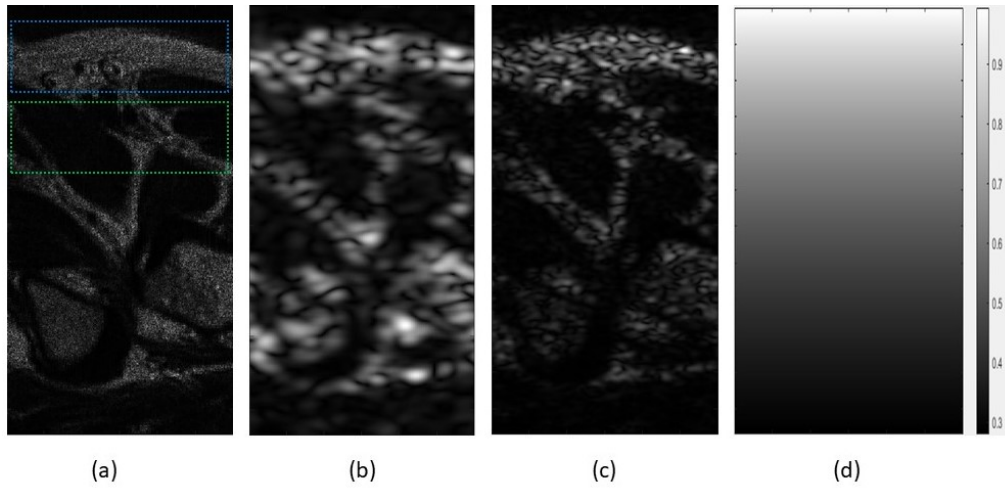


Figure 4.1: (a) TRF mimicking a human kidney (\mathbf{r} of size 1150×300 pixels), (b) simulated fundamental image \mathbf{y}_f , (c) simulated harmonic image \mathbf{y}_h , (d) attenuation map used to simulate the harmonic image in (b), whose values are equal to 1 (no attenuation) close to the probe and to 0.3 (high attenuation) at the bottom of the image. Note that all the images are shown in B-mode for better visualisation.

and their phase information is not important. To further test the proposed algorithm, results on real data will be presented in the following sections.

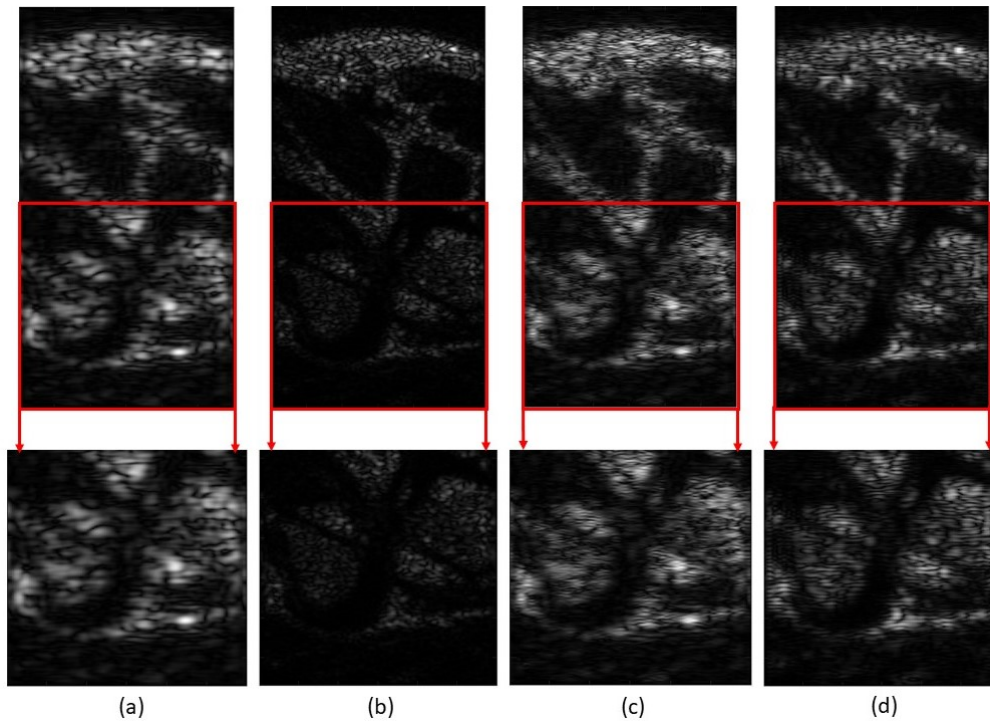


Figure 4.2: Estimated TRF using an alternating estimation approach with: (a) LASSO-fundamental estimated from the fundamental image, (b) LASSO-harmonic estimated from the harmonic image, (c) LASSO-sum and (d) proposed method. All the TRF were estimated by alternating the estimation of the PSF explained in Section 4.2.2 and the estimation of the TRF with one of the restoration techniques considered.

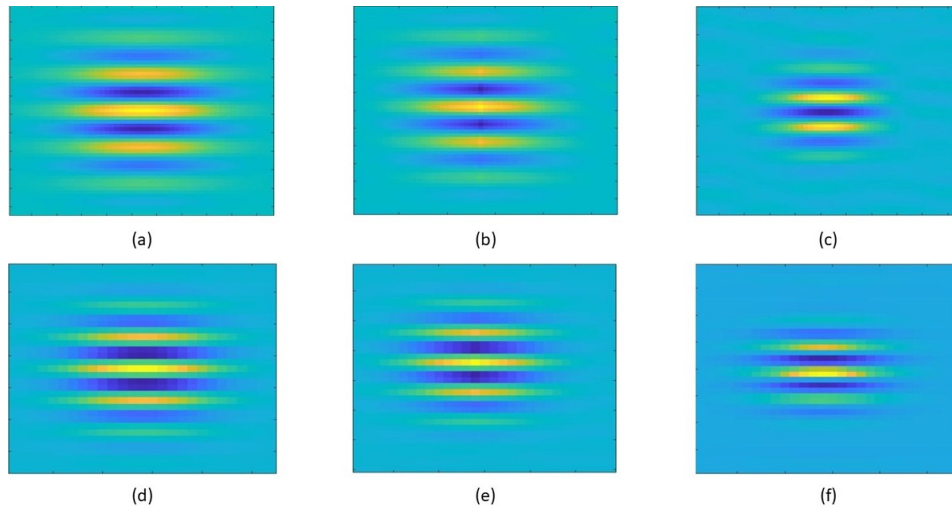


Figure 4.3: The upper row shows the fundamental PSF: (a) true, (b) estimated by homomorphic filtering and (c) estimated by alternative minimization. The lower row shows the harmonic PSF: (d) true, (e) estimated by homomorphic filtering and (f) estimated by alternative minimization.

	LASSO Fundamental	LASSO Harmonic	LASSO Sum	Proposed method
CNR	3.242	2.775	3.196	3.198
SSIM/refl (%)	18.41	14.97	19.06	24.47
RMSE/refl	1.136	1.138	1.368	1.107
RG/fund	2.034	6.008	5.727	5.732
RG/har	0.807	3.289	2.091	2.275

Table 4.1: Quantitative results corresponding to the images of Figure 4.2.

	PSF in Figure 4.3 (b)	PSF in Figure 4.3 (c)	PSF in Figure 4.3 (e)	PSF in Figure 4.3 (f)
SSIM	0.9976	0.9908	0.9981	0.9967
RMSE	0.1511	0.2960	0.2022	0.2668

Table 4.2: Quantitative assessment of the estimated PSF with respect to the true PSF.

4.2.3.2 Phantom image

This section considers a phantom image containing wires located in different part of the image as illustrated in Figure 4.4. The attenuation of harmonic echoes is very low for this example. For this reason, the matrix \mathbf{W} accounting for attenuation in the harmonic direct model was set to the identity matrix. The fundamental and harmonic images are presented in Figure 4.4 (a) and (b) whereas the deconvolution results are shown in Figure 4.5. In general, all the restoration methods that consider the harmonic data (LASSO harmonic, LASSO-sum and proposed) exhibit good spatial resolution. Furthermore, LASSO-sum and the proposed blind approach compensate the harmonic attenuation at high depths by including information from the fundamental image, as shown by the zooms in Figure 4.5. Cysts are also better defined on the restored images by the proposed method in contrast with the native ones. Quantitative results are provided in Table 4.3. They confirm on one hand the

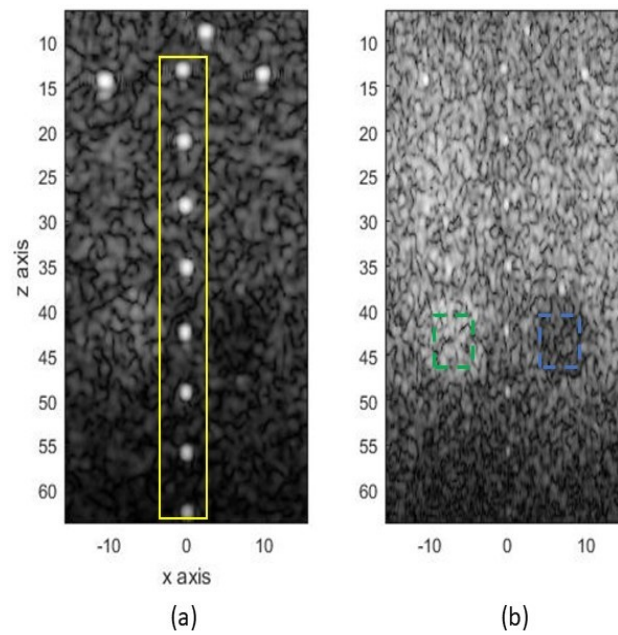


Figure 4.4: Wire phantom image: (a) Fundamental B-mode image, (b) Harmonic B-mode image.

superiority of the proposed method in terms of contrast compared to the other methods. In terms of resolution the harmonic restored images present the highest score, whereas the proposed method

comes second. However, the harmonic images lack of information of depth and deepest wires are less contrasted in contrast with the proposed method. Thus, the proposed method provides overall very competitive results with a good compromise between resolution and contrast.

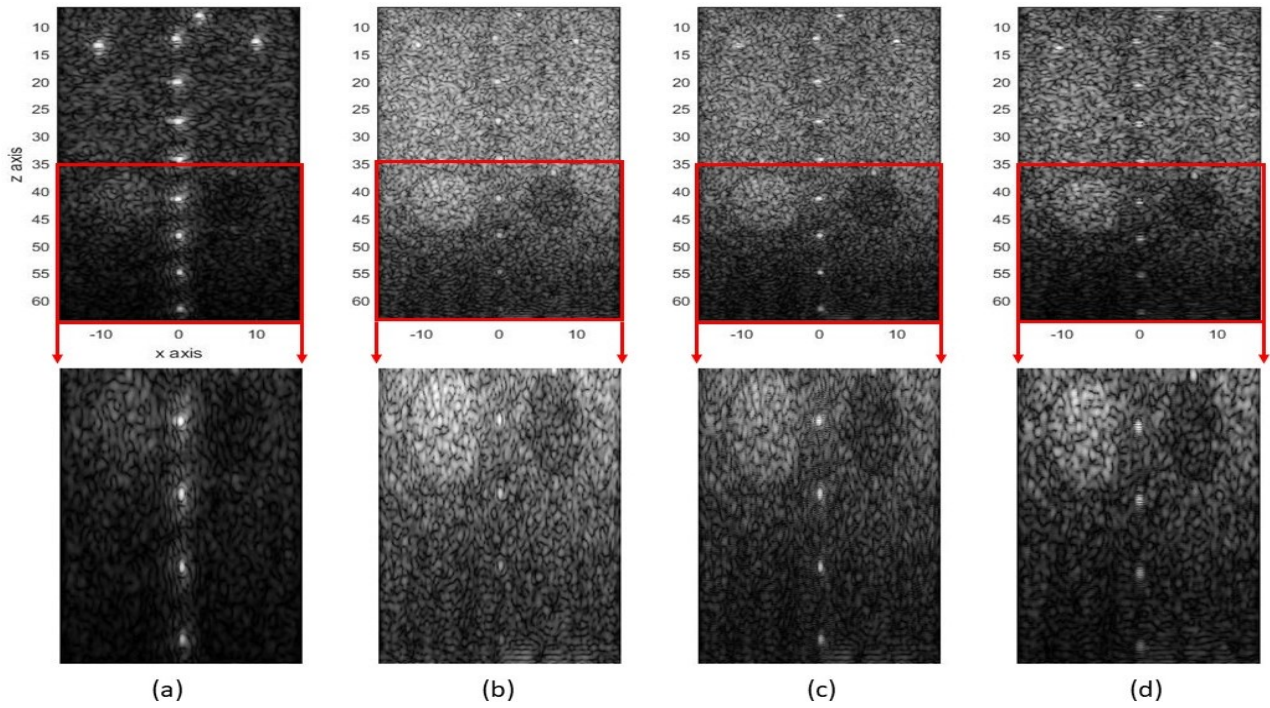


Figure 4.5: Results on phantom data: TRF estimated by (a) LASSO-fundamental, (b) LASSO-harmonic, (c) LASSO-sum, and (d) proposed method. All the TRF were restored using PSF estimated alternatively with the TRF.

	LASSO Fundamental	LASSO Harmonic	LASSO Sum	Proposed method
CNR	0.614	1.066	1.231	1.569
RG/fund	3.222	7.667	5.265	5.800
RG/har	1.074	3.133	2.765	2.933

Table 4.3: Quantitative results computed from the images of Figure 4.5.

4.2.3.3 Carotid image

This section considers a carotid image whose fundamental and harmonic B-mode images are displayed in Figure 4.6 (a) and (b) respectively. From these images, one can clearly observe the better spatial resolution of the harmonic image, at the cost of higher attenuation with depth compared to the fundamental image. In contrast to the phantom experiment, the attenuation matrix \mathbf{W} was estimated as explained in Section 3.6.2. This matrix has a crucial role for this dataset, due to its ability to balance between fundamental and harmonic information. The experiments on carotid are following the same scheme as for the phantom. The visual inspection of the results in Figure 4.7 allows us to conclude that LASSO-sum and the proposed methods, that repose on both fundamental and harmonic components, are able to gather useful information from both observations. In particular, they have the spatial resolution of the harmonic image and compensate for harmonic attenuation with information from the fundamental image. Quantitative results provided in Table. 4.4 confirm the interest of fusing information of both fundamental and harmonic RF images.

Figure 4.8 shows the estimated PSFs obtained with the proposed algorithm, by comparison to the

	LASSO Fundamental	LASSO Harmonic	LASSO Sum	Proposed method
CNR	5.84	7.813	11.864	12.620
RG/fund	2.448	3.736	3.035	3
RG/har	1.48	2.26	1	1.875

Table 4.4: Quantitative results computed from the images of Figure 4.7.

pre-estimated PSFs with zero phase using homomorphic filtering. The proposed blind deconvolution approach is able to estimate the unknown phases of the PSFs, which is very promising. We also compared quantitatively the estimated PSFs after convergence with the smoothing integration method proposed in [MA05]. The smoothing integration method has been widely applied to blind US image deconvolution [ZBKT14, Mor13, Che16] and adopted in Chapter 3. Since in real images there is no ground truth for the PSFs, in Table 4.5 we compare the estimated PSFs using the proposed method

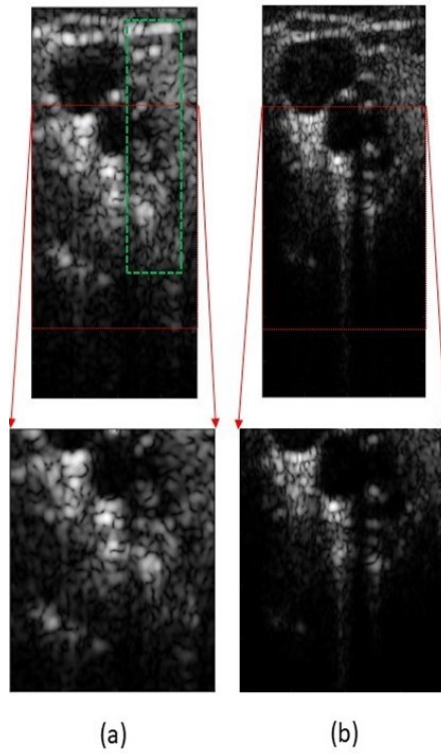


Figure 4.6: Carotid image: (a) Fundamental B-mode image, (b) Harmonic B-mode image.

with the estimated PSFs using the smoothing integration method. We can see a high similarity between the estimated PSFs with RMSE values around 10^{-4} and SSIM values around 99%.

	Fundamental PSF	Harmonic PSF
SSIM	99.84	99.72
RMSE ($\times 10^{-4}$)	4,71	9,82

Table 4.5: Quantitative results comparing the fundamental and harmonic PSFs estimated by the proposed method in contrast to the smoothing integration method.

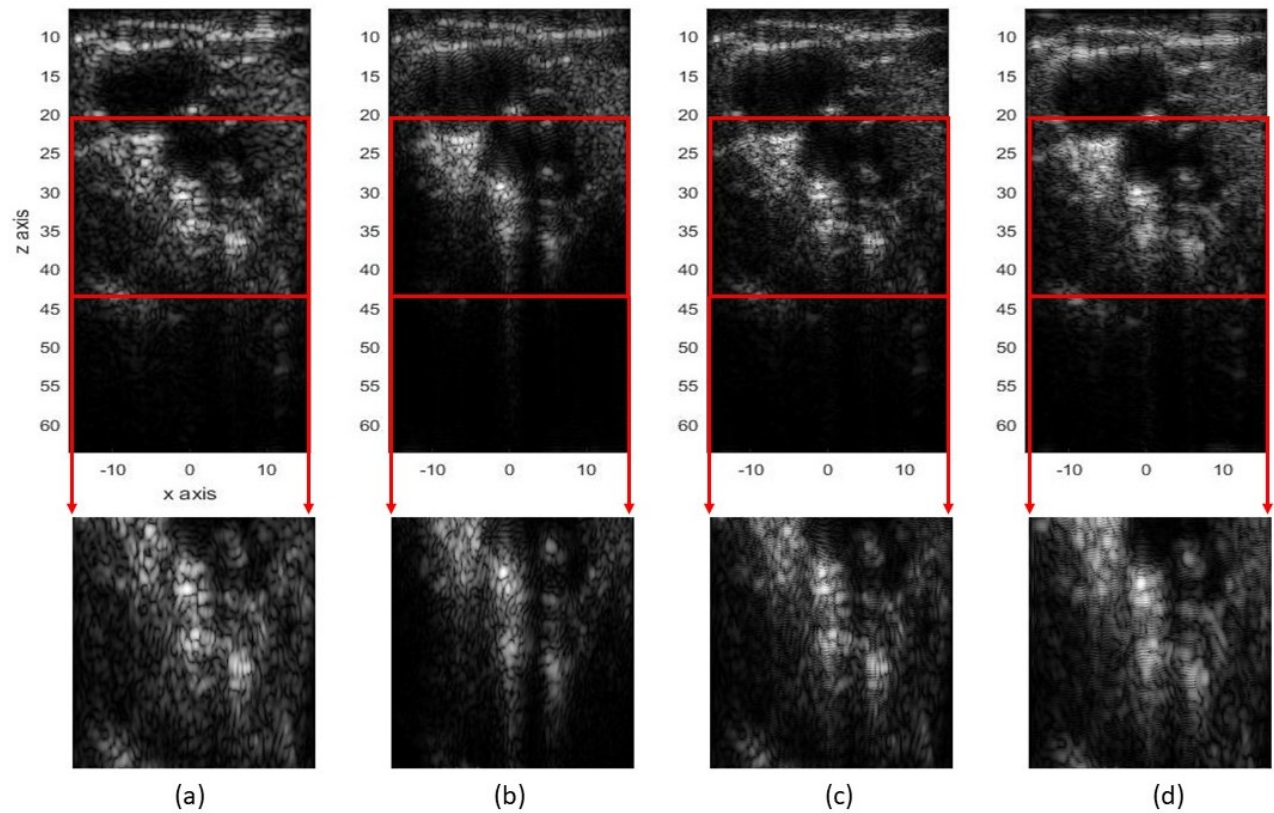


Figure 4.7: Results on carotid data: TRF estimated by (a) LASSO-fundamental, (b) LASSO-harmonic, (c) LASSO-sum, and (d) proposed method. All the TRF were restored using PSF estimated alternatively with the TRF.

4.2.4 Discussion

The regularization parameters were set as follows in all the experiments: $\mu = 0.02$ and $\beta = 1$. In addition, 10 iterations were sufficient to ensure the convergence of the algorithm, with a stopping criterion based on the relative error between two consecutive values of the cost function in (4.1). The tolerance of the relative error was set to 10^{-5} (see Equation (3.18)). To finish, we would like to provide some conclusions regarding the deconvolution methods of chapters 3 and 4. In terms of visual inspection, both approaches present satisfying results mitigating the PSF effect and collecting in one image a better version of the restored images using both fundamental and harmonic image. In

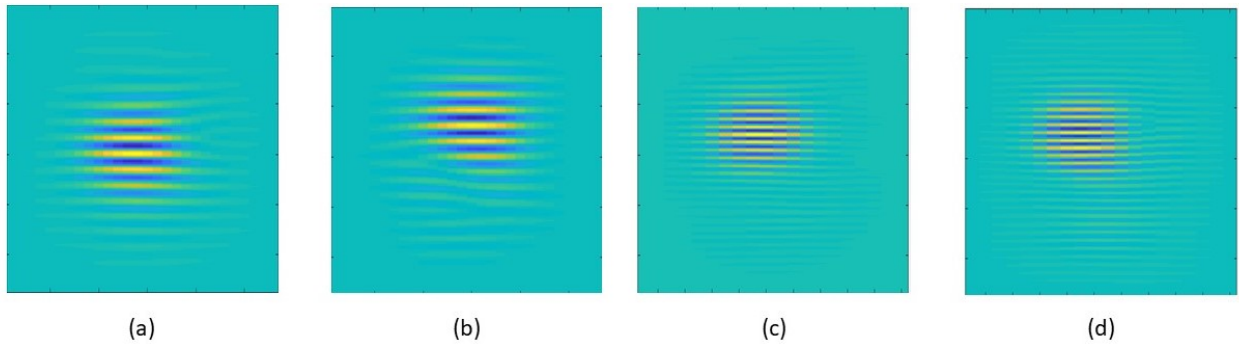


Figure 4.8: (a) Zero phase fundamental PSF $\hat{\mathbf{h}}_f$, (b) Estimated fundamental PSF h_f , (c) Zero phase harmonic PSF $\hat{\mathbf{h}}_h$, (d) Estimated harmonic PSF h_h .

addition, the interest of both proposed methods was clearly highlighted in contrast with LASSO-fund, LASSO-harmonic and LASSO-sum. Quantitatively, if we compare Tables 3.5 and 4.3 for the phantom image and Tables 3.6 and 4.4 for the carotid image, one can see that the deconvolution approach with pre-estimated PSF presents higher scores in contrast with the fully blind approach. However, the joint fully blind deconvolution method have a shorter computation time. Note that, in the blind deconvolution with pre-estimated PSF, the estimation time of the PSF should be considered. Here, we mention that the PSF estimation time in [MA05] depends on the size of the image (the bigger the size of the image, the longer the estimation time). The relation between the computation time of the PSF estimation and the size of the image comes from the fact that the approach presented in [MA05] segments the RF image into overlapped horizontal RF segments, and then chooses different RF-blocks in each segment and calculates the PSF estimation on each block. After all, the estimated PSFs of all the blocks are averaged. In addition, the phase estimation presented in [MA05] is computationally intensive. In order to decrease this estimation time, we have decided to estimate the PSF in the two steps method from the focal point region, where the lateral resolution is the highest. Indeed, the elapsed time of the estimation of the PSF from the whole image of carotid (size 384×4480) followed by the joint deconvolution is about 3 hours whereas it is about 6 minutes when the PSF estimation is restricted into the focal point region. On the other hand, the execution time of the fully blind method is around 3 minutes (see Table 4.6). Note that all the simulations were done on a

standard 3.6 GHz Intel Core i7 with a straightforward MATLAB implementation without GPU. The

	Blind deconvolution with pre-estimated PSF		Fully blind deconvolution
Computation time	PSF estimation 6 minutes	TRF estimation 10 seconds	142 seconds

Table 4.6: Comparison of the computation time of the blind deconvolution methods.

fully blind restoration considers only the calculation of the magnitude of the PSFs from the whole image by homomorphic filtering and then the phase estimation is calculated iteratively based on the phase difference between the observed image and the calculated TRF in the previous iteration. Thereby, the choice of the deconvolution method is a compromise between the computational time and the performance.

4.3 Joint deconvolution with a spatially varying PSF

The PSF of US images is spatially varying as discussed in the Section 2.2. Based on [NPK⁺06], the PSF can be supposed to be axially varying. The lateral variability of the PSF depends on the position of the target with respect to the central axis of the transducer. To compensate this variability, apodization is applied by dynamically weighting the aperture so the PSF does not change laterally on a given depth. In addition, the number of samples in the axial direction is much more higher than the lateral direction (few thousands samples in the axial direction while few hundreds in the lateral one). Thus, assuming that the PSF is only axial varying is considered fair in ultrasound imaging [ZAI03, NPK⁺06, MA05]. While few studies consider the spatial variation of the PSF [RSHB17, FBKV18b, Mic17], most of the existing approaches assume an invariant PSF to reduce the complexity of the restoration problem [Tax95, MA05, APR95, CBK16b]. In this case, image restoration is applied to image segments where the hypothesis of invariant PSF may hold. Consequently, stitching artifacts appear after merging the different restored segments in order to rebuild the whole restored

image [NO98]. The objective of this section is to propose a fast and efficient way to restore jointly fundamental and harmonic US images by solving an appropriate inverse problem using a block-wise approach allowing us to take into account that the PSF is spatially varying..

4.3.1 Block-wise joint deconvolution

The approach proposed in [VBA⁺16] considers different PSFs at different depths and then creates a sequence of images by convolution between the medium scattering map and the sequence of PSFs. Finally, a PSF weighting function is applied in order to build the final image. In the inverse solution considered in this work, a similar method is investigated, which can be summarized into two steps. First, n PSFs are estimated at n different depths from image segments extracted from the RF images using the method proposed in [MA05]. As a result, n RF restored images are obtained from the deconvolution of the fundamental and harmonic RF images with the n estimated PSFs (see Figure 4.9).

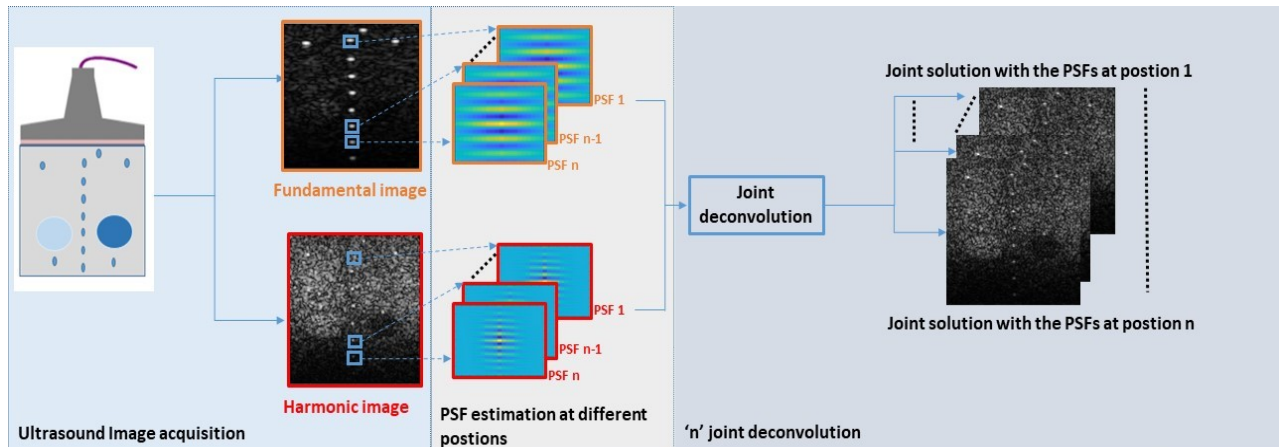


Figure 4.9: PSF estimation and image deconvolution using a sequence of estimated PSFs.

Note that n different weighting functions are created corresponding to the n PSFs. Each weighting function w_i reaches its maximum at the depth where the i th PSF is estimated. The amplitudes of the different weights w_i are defined using continuous windows along the z -axis illustrated in Figure

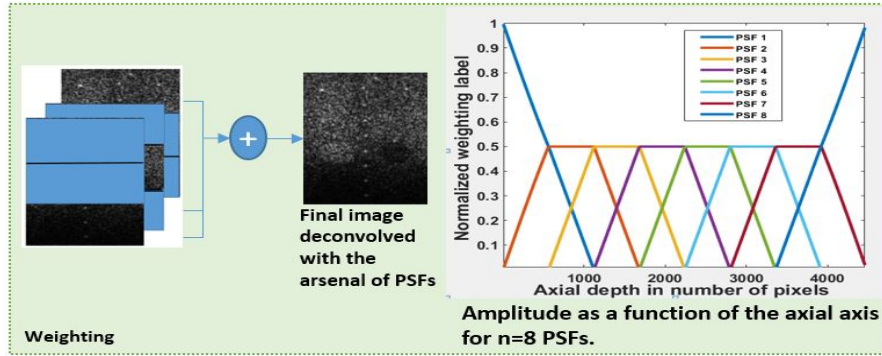


Figure 4.10: Principle of block weighting and weighting functions w_i corresponding to the different PSFs as a function of depth.

4.10 in the particular case of n PSFs and are normalized in order to obtain:

$$\forall z \in \mathbb{R}, \quad \sum_{i=1}^n w_i(z) = 1. \quad (4.9)$$

Finally, in order to obtain the final restored image Im , the n restored images are merged using a linear combination defined as:

$$\text{Im} = \sum_{i=1}^n w_i R_i \quad (4.10)$$

In other words, in the region of the i th PSF, the restored image R_i is weighted with an amplitude of 0.5 while R_{i-1} and R_{i+1} are weighted with values from the negative and positive slope respectively (between 0 and 0.5).

4.3.2 Results

Two acquisitions were considered to test the proposed method, as described hereafter.

Phantom image:

The first data was acquired on a tissue mimicking phantom (model 404GS LE, Gammex Inc., Middleton, WI, USA) including both anechoic/hypoechoic cysts and wire targets. The simple structures in this phantom allowed us to objectively evaluate the resolution gain and the restoration of the information in depth enabled by the proposed method.

Carotid image:

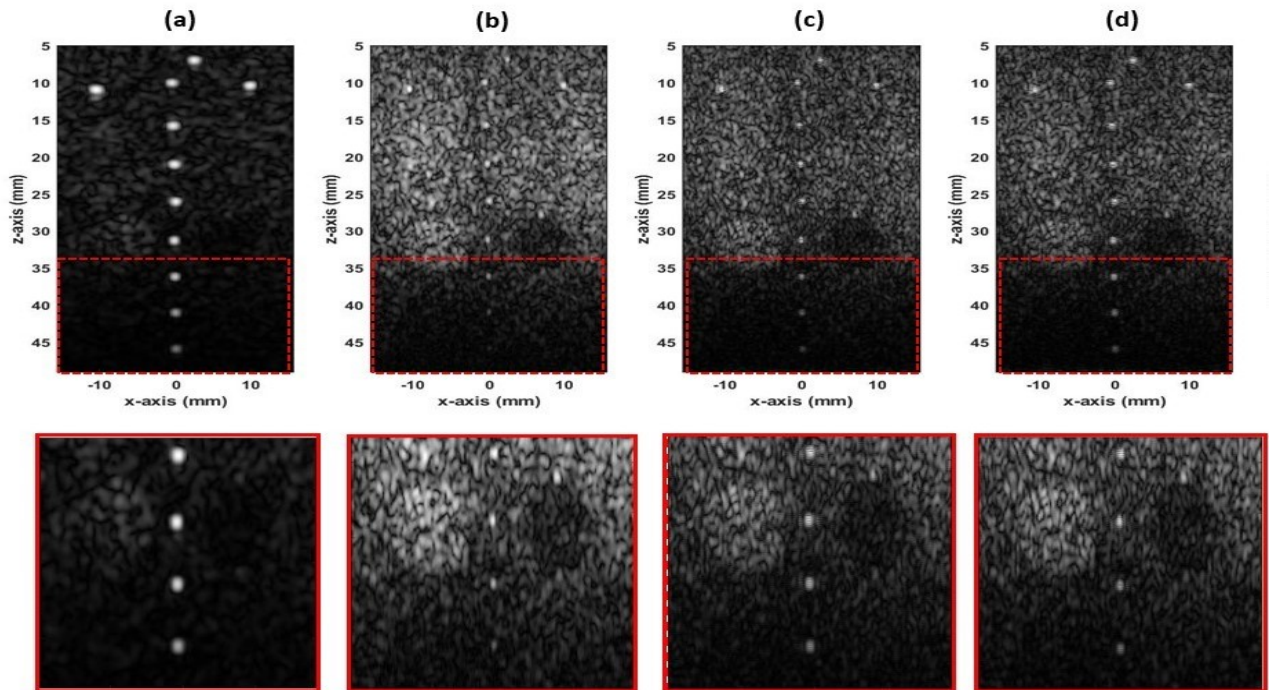


Figure 4.11: Phantom experiment: (a) fundamental image, (b) harmonic image, (c) deconvolution solution using a spatially invariant PSF, and (d) deconvolution solution using the proposed method. The second row shows a zoom corresponding to the rectangular region displayed in (a).

The second acquisition was done *in vivo* by scanning the carotid artery and jugular vein of a young healthy volunteer. This image contains more complicated structures and represents a more difficult challenge than the previous phantom to prove the functionality of the proposed restoration procedure. In both experiments, images were divided into eight segments for PSF estimation and block-wise image restoration. The proposed method is compared to the joint deconvolution technique of Chapter 3 that considers a spatially invariant PSF. In the phantom experiment, the full width at half maximum (FWHM) computed around the wire locations was calculated as a metric of spatial resolution. In the carotid experiment, the resolution gain [YZX12a] was calculated for both solutions obtained using spatially invariant and variant block-wise PSFs. The images corresponding to the phantom experiment are shown in Figure 4.11. The interest of image deconvolution can be appreciated in Figure 4.11 (c,d), in particular the improved spatial resolution compared to the fundamental image

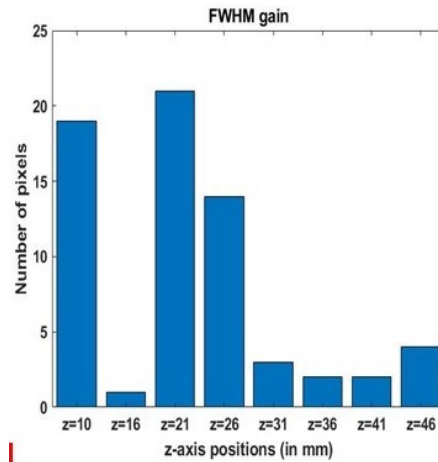


Figure 4.12: Phantom experiment: gains of FWHM for each wire at each depth in the proposed method and in the joint deconvolution with invariant PSF.

in Figure 4.11 (a) and the better signal to noise ratio at high depth compared to the harmonic image in Figure 4.11 (b). Indeed, one can see that the anechoic/hypoechoic regions are well defined in the Figure 4.11 (d) and the wires are thinner compared to the ones in the Figure 4.11 (c). Thus, the improved resolution obtained using a spatially-varying PSF can be clearly observed: a FWHM improvement is presented in Figure 4.12 at different depths confirming the advantage of the proposed method. The FWHM improvement is the difference between the FWHM of a wire in the joint solution considering spatially invariant PSFs and the FWHM of the corresponding wire in the result of the proposed method : This improvement highlights the advantage of considering a spatially varying PSF in order to obtain better resolution. The images corresponding to the carotid experiment are shown in Figure 4.13. One can observe that the proposed method eliminates the reverberation effect caused generally by the deconvolution, while preserving a good restoration result. In particular, an improvement of the resolution gain is obtained: with a RG of the proposed method with respect to the harmonic image equal to 7.97 where the RG of the deconvolution method using only one invariant PSF with respect to the harmonic image is 6.85 (an improvement of 1.12). We note here that the RG is calculated in the red dashed section in the Figure 4.13. The red arrows in 4.13 (c) point out reverberation effects caused by deconvolution with an invariant PSF where one can see the reduction

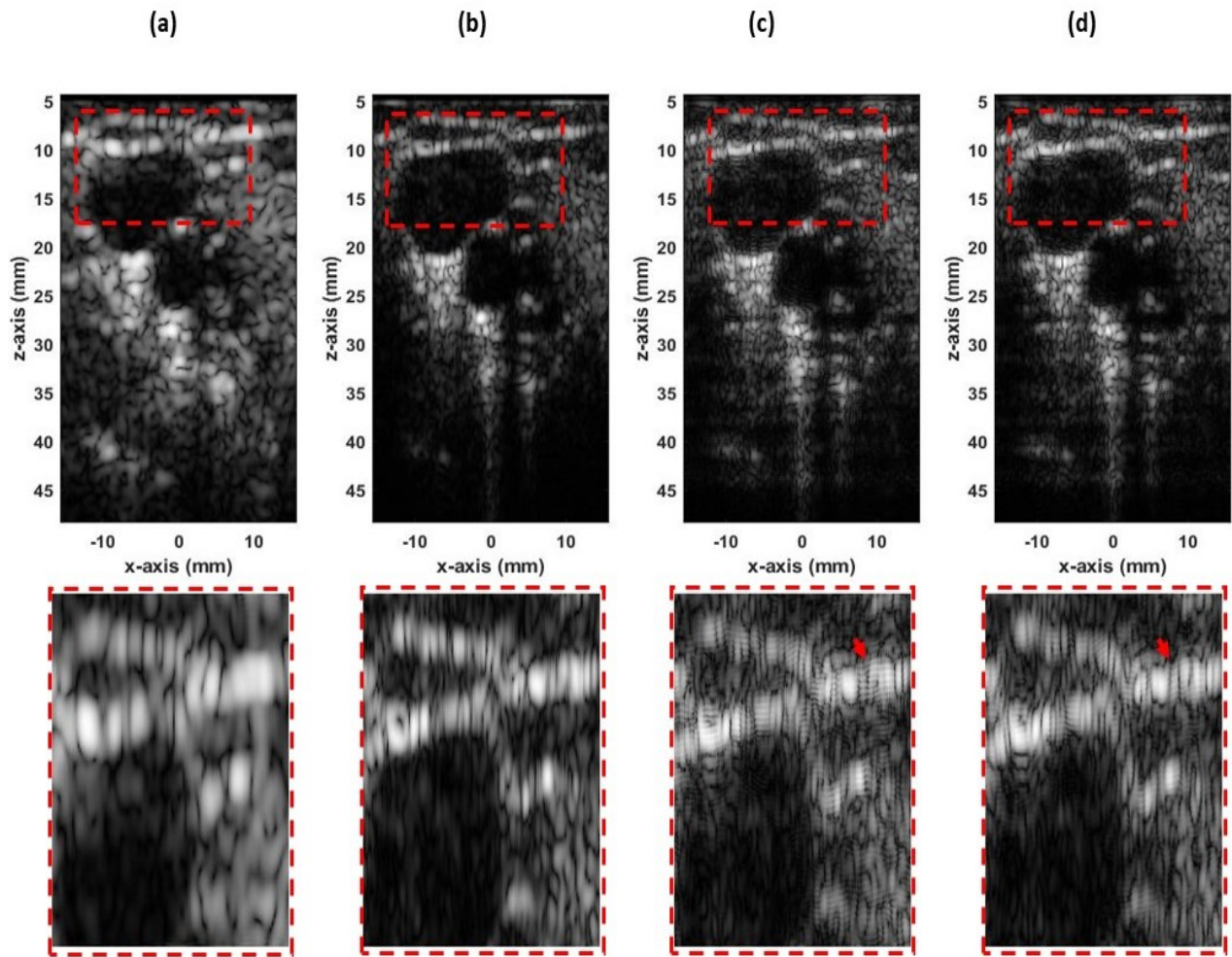


Figure 4.13: Carotid experiment: (a) fundamental image, (b) harmonic image, (c) deconvolution solution using an invariant PSF, and (d) deconvolution solution using the proposed method.

of this reverberation by considering the spatially varying PSF (see Figure 4.13 (d)). Finally, one can note that there is no boundary artifact between the several blocks thanks to the choice of the weighting functions.

4.4 Conclusion

After presenting the advantages of the joint deconvolution of fundamental and harmonic images in Chapter 3, the objective of this chapter was to introduce two strategies to improve the joint deconvolution by proposing two upgrades related to the PSF. The first approach considers an alternating PSF-TRF estimation. In this case the PSF is estimated simultaneously with the TRF. The results were promising and an improvement of the computation time compared to a restoration approach with a pre-estimated PSF. This result may push the joint deconvolution one step closer to be able to be integrated as a plug and play segment in US imaging systems. Another point addressed in this chapter is to exploit the fact that the PSF is spatially varying and to incorporate this knowledge into the restoration. While the majority of existing restoration methods considers an invariant PSF, we have considered an efficient block-wise restoration approach allowing the spatial variability of the PSF to be considered. The spatial variability of the PSF was considered in the axial direction, and neglected in the lateral direction. The latter assumption relies on the characteristics of the US image and its acquisition specification. The proposed method is easy to implement, does not present stitching artifacts, reduces the reverberation artifacts and can be coupled to any restoration solution. We think that it is a simple way of bypassing the problems related to a spatially varying PSF.

CHAPTER 5

Conclusions and perspectives

5.1 Conclusions

The objective of this research work was to improve the resolution of US images by investigating the deconvolution methods that take into consideration the non-linearity of US waves. US imaging has many advantages related to its use that have contributed to its popularity, despite its relatively low and variable image quality. Most of the work to improve the quality of US images has focused on instrumental specifications and beamforming techniques. In parallel, post-processing techniques had raised, and generally offered better flexibility. Chapter 1 of this manuscript is dedicated to US physics, imaging system. Chapter 2 presented the state-of-the-art of the existing techniques that improve the spatial resolution of US images through pre-processing and post-processing techniques. In addition, under the first Born approximation, the derivation of the linear US image model based on the US waves propagation equations was recalled in this chapter.

The main challenge of this thesis was to show the interest of integrating the non-linearity into the restoration process. In the first contributions presented in Chapter 3, a new joint deconvolution problem was established based on a US image model gathering the fundamental and the harmonic information. An attenuation matrix was integrated in the harmonic image model in order to consider the important attenuation in this image modality. For real images, the elements of this matrix were estimated based on a spectral analysis. Furthermore, a cost function was formulated considering the data fidelity term of fundamental and harmonic images and a Laplacian regularization. An ADMM algorithm was finally investigated to solve the resulting deconvolution problem. A cross-validation was applied in order to find the most optimal regularization parameters. In this chapter, the PSF was estimated in a pre-processing step and considered spatially invariant. Results obtained on simulated

and real images clearly showed the interest of combining the information contained in the two modes instead of restoring them independently.

Chapter 4 presented two contributions related to the PSF. The first consisted in estimating the PSF alternately with the TRF. An iterative alternating algorithm was applied in order to alternate between the TRF and PSF estimation steps. The magnitude of the PSF, estimated by homomorphic filtering, was designed as a constraint to the problem. Only the PSF phase was estimated in the alternating problem based on the difference of phase between the observed image and the estimated TRF in the previous estimation. The latter approach prevents an exhaustive and hard task: the PSF phase unwrapping. The results applied on real and simulated images were promising in particular from a perspective of complexity reduction compared to the pre-estimation approach of the PSF presented in the Chapter 3. The second part of this chapter considered the spatial variation of the PSF. The restoration was applied with estimated PSFs at different depths. A smooth interpolation weighted the restored images in order to prevent the stitching artifact and to consider mainly the spatial variability of the PSF in the axial direction. Results on real images showed a decrease of Gibbs artifacts due to the PSF spatial invariability assumption considered in the restoration problem.

5.2 Future work and perspectives

The open challenges and perspectives resulting from this thesis are listed in what follows:

- **Filtering:** These works require the extraction of the fundamental and harmonic images. In this work, linear band-pass filters were used due to the low spectrum overlap between the fundamental and harmonic components. However, imaging with short emitted pulse or in the presence of contrast agents may increase the overlapping and linear filtering will not be anymore a suitable solution. Applying beamforming techniques such as pulse inversion represents an interesting alternative to filtering. Alternatively, the application of blind source separation on the raw images may be considered a potential perspective [WSVS⁺20]. Alternatively, we proposed in a preliminary study a Hammerstein model in order to separate the fundamental and the harmonic images [HBK⁺18]. In the same perspective, [PE03a] considered a Volterra

model to separate the linear and quadratic components for contrast imaging applications.

- **Harmonic image observation model:** Under the first Born approximation, the harmonic image model is expressed as a convolution between the TRF and the PSF. However, the latter assumption can only be applied in the imaging of tissues with low non-linearity. In order to expand the application of the proposed algorithm to the contrast imaging, a nonlinear model of the harmonic image should be considered and consequently another framework that deals with non-smooth and non-convex problem should be adopted [BST14].
- **Fusion:** For simplicity the TRF was considered the same for fundamental and harmonic images. However, due to the non-linearity, some regions of the imaged tissues may have a relevant nonlinear response whereas the information around the fundamental frequency is less important (especially in contrast imaging). Thus, two data reflectivity functions should be considered in a future work where the relation between the fundamental and harmonic images should be investigated and integrated in the cost function in order to ensure the convergence of the fusion algorithm. A recent work was established on the fusion of US and MRI images address this task [EMVB⁺20].
- **Hyper-parameters:** As explained in Chapters 3 and 4, hyper-parameters play an important role in the image restoration process. The choice of hyper-parameters was done based on cross-validation. It would be interesting to investigate some fast methods to tune these hyper-parameters adaptively [XFG17, ACFBD19].
- **Optimization framework:** ADMM was adopted in the proposed work to minimize the cost function resulting from the US deconvolution process. Despite its flexibility and interesting convergence properties, other optimization algorithms could offer interesting perspectives as FISTA [BT09], and the proximal alternating linearized minimization (PALM) [BST14] especially when considering a nonlinear image models.
- **Spatial variability of the PSF:** In this work, the spatial variability of the PSF was considered in Chapter 4. The latter method consists in applying a interpolation after the restoration of the

US image with different PSFs on different depths. However, it could be interesting to integrate the spatial variability of the PSFs in the observation model and consider it into the resulting inverse problem [Mic17, FBKV18b, BRP⁺19b].

- **Deep learning:** Recently, deep learning has appeared as a powerful tool for number of US image enhancement tasks [VSCE19, LMG⁺20, YKHY18]. In addition, [KHY20] had presented an unsupervised deep learning approach to deal with the US restoration problem. All the latter research encourage to consider the artificial intelligence in a future work to deal with the joint deconvolution problem.

Appendices

APPENDIX A

Blurring operator in spatial and frequency domains

In this work, the image formation model considered is a 2D convolution between the PSF and the TRF and can be expressed as follows:

$$\mathbf{Y} = \mathbf{h} \circledast \mathbf{X}, \quad (\text{A.1})$$

where \mathbf{X} and $\mathbf{Y} \in \mathbb{R}^{m \times n}$ are the ground truth image and the observed image respectively (here we mention that the output of the convolution is \mathbf{Y} , which is cropped in order to have the same size of \mathbf{X}). $\mathbf{h} \in \mathbb{R}^{p \times q}$ is the PSF kernel (where $p < m$ and $q < n$ in our application). The image formation model in (A.1) can be expressed as a matrix/vector multiplication as follows:

$$\mathbf{y} = \mathbf{H}\mathbf{x}, \quad (\text{A.2})$$

where \mathbf{y} and $\mathbf{x} \in \mathbb{R}^{N \times 1}$ (where $N = m \times n$) are the stacked column vectors formed from \mathbf{Y} and \mathbf{X} by lexicographical ordering. The matrix $\mathbf{H} \in \mathbb{R}^{N \times N}$ is a block circulant with circulant blocks (BCCB) matrix when circular boundaries conditions are considered [HNO06]. Note that the consideration of circular convolution does not have any theoretical justification, but has a computational interest as it will be further shown in this appendix.

A.1 Block circulant matrix with circulant blocks

A BCCB matrix is a matrix that can be partitioned into blocks and each individual block is circulant. In order to present in details the construction of the BCCB matrix from the blurring kernel, let us consider the following example of the convolution of the ground truth image $\mathbf{X} \in \mathbb{R}^{6 \times 6}$ with the PSF

$\mathbf{h} \in \mathbb{R}^{3 \times 3}$ in order to create the observed (blurred) image $\mathbf{Y} \in \mathbb{R}^{6 \times 6}$:

$$\mathbf{X} = \begin{bmatrix} x_{11} & x_{12} & x_{13} & x_{14} & x_{15} & x_{16} \\ x_{21} & x_{22} & x_{23} & x_{24} & x_{25} & x_{26} \\ x_{31} & x_{32} & x_{33} & x_{34} & x_{35} & x_{36} \\ x_{41} & x_{42} & x_{43} & x_{44} & x_{45} & x_{46} \\ x_{51} & x_{52} & x_{53} & x_{54} & x_{55} & x_{56} \\ x_{61} & x_{62} & x_{63} & x_{64} & x_{65} & x_{66} \end{bmatrix}, \quad \mathbf{h} = \begin{bmatrix} h_{11} & h_{12} & h_{13} \\ h_{21} & h_{22} & h_{23} \\ h_{31} & h_{32} & h_{33} \end{bmatrix} \quad \text{and} \quad \mathbf{Y} = \begin{bmatrix} y_{11} & y_{12} & y_{13} & y_{14} & y_{15} & y_{16} \\ y_{21} & y_{22} & y_{23} & y_{24} & y_{25} & y_{26} \\ y_{31} & y_{32} & y_{33} & y_{34} & y_{35} & y_{36} \\ y_{41} & y_{42} & y_{43} & y_{44} & y_{45} & y_{46} \\ y_{51} & y_{52} & y_{53} & y_{54} & y_{55} & y_{56} \\ y_{61} & y_{62} & y_{63} & y_{64} & y_{65} & y_{66} \end{bmatrix}$$

The convolution mechanism consists in rotating the kernel \mathbf{h} around its center and afterwards the kernel is placed over each element of \mathbf{x} . Considering circular boundaries, an element by element multiplication and summation are applied in order to obtain the value of \mathbf{Y} at the associated position (see (A.3) and (A.4)). Afterwards, the previous procedure is repeated by moving the kernel over the different element of \mathbf{x} .

$$\begin{array}{|c|c|c|c|c|c|c|c|} \hline x_{66}h_{33} & x_{61}h_{32} & x_{62}h_{31} & x_{63} & x_{64} & x_{65} & x_{66} & x_{61} \\ \hline x_{16}h_{23} & x_{11}h_{22} & x_{12}h_{21} & x_{13} & x_{14} & x_{15} & x_{16} & x_{11} \\ \hline x_{26}h_{13} & x_{21}h_{12} & x_{22}h_{11} & x_{23} & x_{24} & x_{25} & x_{26} & x_{21} \\ \hline x_{36} & x_{31} & x_{32} & x_{33} & x_{34} & x_{35} & x_{36} & x_{31} \\ \hline x_{46} & x_{41} & x_{42} & x_{43} & x_{44} & x_{45} & x_{46} & x_{41} \\ \hline x_{56} & x_{51} & x_{52} & x_{53} & x_{54} & x_{55} & x_{56} & x_{51} \\ \hline x_{66} & x_{61} & x_{62} & x_{63} & x_{64} & x_{65} & x_{66} & x_{61} \\ \hline x_{16} & x_{11} & x_{12} & x_{13} & x_{14} & x_{15} & x_{16} & x_{11} \\ \hline \end{array} \quad (\text{A.3})$$

Thus we can express :

$$y_{11} = h_{33}x_{66} + h_{32}x_{61} + h_{31}x_{62} + h_{23}x_{16} + h_{22}x_{11} + h_{21}x_{12} + h_{13}x_{26} + h_{12}x_{21} + h_{11}x_{22} \quad (\text{A.4})$$

By way of analogy, the BCCB matrix $\mathbf{H} \in \mathbb{R}^{36 \times 36}$ can be expressed as follows:

$$\mathbf{H} = \begin{bmatrix} \mathbb{H}_2 & \mathbb{H}_1 & \circ & \circ & \circ & \mathbb{H}_3 \\ \mathbb{H}_3 & \mathbb{H}_2 & \mathbb{H}_1 & \circ & \circ & \circ \\ \circ & \mathbb{H}_3 & \mathbb{H}_2 & \mathbb{H}_1 & \circ & \circ \\ \circ & \circ & \mathbb{H}_3 & \mathbb{H}_2 & \mathbb{H}_1 & \circ \\ \circ & \circ & \circ & \mathbb{H}_3 & \mathbb{H}_2 & \mathbb{H}_1 \\ \mathbb{H}_1 & \circ & \circ & \circ & \mathbb{H}_3 & \mathbb{H}_2 \end{bmatrix} \quad (\text{A.5})$$

where $\circ \in \mathbb{R}^{6 \times 6}$ is a matrix of zeroes, and $\mathbb{H}_k \in \mathbb{R}^{6 \times 6}$ is defined as follows:

$$\mathbb{H}_k = \begin{bmatrix} h_{2k} & h_{1k} & 0 & 0 & 0 & h_{3k} \\ h_{3k} & h_{2k} & h_{1k} & 0 & 0 & 0 \\ 0 & h_{3k} & h_{2k} & h_{1k} & 0 & 0 \\ 0 & 0 & h_{3k} & h_{2k} & h_{1k} & 0 \\ 0 & 0 & 0 & h_{3k} & h_{2k} & h_{1k} \\ h_{1k} & 0 & 0 & 0 & h_{3k} & h_{2k} \end{bmatrix} \quad (\text{A.6})$$

A.2 Spectral decomposition of the BCCB matrix

The large size of \mathbf{H} matrix makes it difficult to use. However, the BCCB matrix, \mathbf{H} , is a normal matrix ¹ and admits a spectral decomposition as follows:

$$\mathbf{H} = \mathcal{F}^* \Lambda \mathcal{F}, \quad (\text{A.7})$$

where $\mathcal{F} \in \mathbb{C}^{N \times N}$ is the 2D unitary discrete Fourier transform (DFT) matrix, $*$ represents the conjugate transpose and the diagonal matrix $\Lambda = \text{diag}[\lambda_1, \dots, \lambda_N]$ contains the eigenvalues of $\mathbf{H} \in \mathbb{R}^{N \times N}$. Therefore, (A.2) can be expressed as follows:

$$\mathbf{y} = \mathbf{H}\mathbf{x} = \mathcal{F}^* \Lambda \mathcal{F}\mathbf{x} \quad (\text{A.8})$$

¹ \mathbf{H} is a normal matrix $\Rightarrow \mathbf{H}^* \mathbf{H} = \mathbf{H} \mathbf{H}^*$, where $(\cdot)^*$ is the conjugate operator

Note that $\mathcal{F}\mathbf{x}$, where \mathbf{x} is the vectorized version of the image of the image \mathbf{X} , represents the vectorized form of its 2D Fourier transform and can thus be obtained in a computationally efficient way by a 2D fast Fourier transform. The same remark applies to $\mathcal{F}^*\mathbf{x}$ that represents the inverse Fourier transform of \mathbf{X} and can thus be computed by the fast inverse Fourier transform. Using the fast Fourier transform, the computational complexity is reduced to $\mathcal{O}(N \log N)$ from $\mathcal{O}(N^2)$. Since the implicit matrix \mathcal{F} is a unitary matrix, we have the following relationship:

$$\mathbf{H} = \mathcal{F}^* \Lambda \mathcal{F} \Rightarrow \mathcal{F} \mathbf{H} = \Lambda \mathcal{F} \Rightarrow \mathcal{F} \mathbf{h}_1 = \Lambda f_1 = \boldsymbol{\lambda} / \sqrt{N}, \quad (\text{A.9})$$

where $\boldsymbol{\lambda} \in \mathcal{R}^{N \times 1}$ is a vector which contains all the eigenvalues of \mathbf{H} , f_1 is the first column of the matrix \mathcal{F} and is thus a vector of ones and \mathbf{h}_1 is the first column of the BCCB matrix \mathbf{H} . The eigenvalues of \mathbf{H} can be obtained by multiplying the first column of \mathbf{H} by $\sqrt{N} \mathcal{F}$. Equivalently, in order to compute the eigenvalues of \mathbf{H} , the DFT can be applied on a two dimensional array containing the elements of the first column of the PSF. Indeed, we can get this array, from the PSF kernel \mathbf{h} by shifting the latter around its center. Thus, the convolution model can be expressed as follows:

$$\mathbf{Y} = \text{ifft2}(S .* \text{fft2}(\mathbf{X})), \quad (\text{A.10})$$

where $.*$ represents an element-wise multiplication and S can be calculated from the kernel \mathbf{h} as follows:

$$S = \text{fft2}(\text{circshift}(\mathbf{h}, 1 - \text{center})). \quad (\text{A.11})$$

Note that S is an array (and not a vector), and the eigenvalues are not sorted and

$$\mathbf{h}_1 = \text{vec}(\text{circshift}(\mathbf{h}, 1 - \text{center})), \quad (\text{A.12})$$

where vec represents the vectorization step. In the case where the PSF array \mathbf{h} is 'smaller' than \mathbf{Y} and \mathbf{X} , a zero-padding of \mathbf{h} is applied to embed the $p \times q$ array in a larger array of size $m \times n$ and ensure that all arrays in (A.10) have the same size.

Bibliography

- [ABDF10a] Manya V Afonso, José M Bioucas-Dias, and Mário AT Figueiredo. An augmented lagrangian approach to the constrained optimization formulation of imaging inverse problems. *IEEE Trans. Im. Proc.*, 20(3):681–695, 2010.
- [ABDF10b] Manya V Afonso, José M Bioucas-Dias, and Mário AT Figueiredo. Fast image recovery using variable splitting and constrained optimization. *IEEE transactions on image processing*, 19(9):2345–2356, 2010.
- [ABTT84] Sigurd Ivar Aanonsen, Tor Barkve, Jacqueline Naze Tjo/tta, and Sigve Tjo/tta. Distortion and harmonic generation in the nearfield of a finite amplitude sound beam. *The Journal of the Acoustical Society of America*, 75(3):749–768, 1984.
- [ACFBD19] Setareh Ariaifar, Jaume Coll-Font, Dana H Brooks, and Jennifer G Dy. Admmbo: Bayesian optimization with unknown constraints using admm. *J. Mach. Learn. Res.*, 20(123):1–26, 2019.
- [AFS15] Arash Anvari, Flemming Forsberg, and Anthony E Samir. A primer on the physical principles of tissue harmonic imaging. *Radiographics*, 35(7):1955–1964, 2015.
- [AMP⁺11] Martino Alessandrini, Simona Maggio, Jonathan Porée, Luca De Marchi, Nicolo Speciale, Emilie Franceschini, Olivier Bernard, and Olivier Basset. A restoration framework for ultrasonic tissue characterization. *IEEE Trans. Ultrason. Ferroelectr. Freq. Control.*, 58(11):2344–2360, 2011.

- [APR95] Udantha R Abeyratne, Athina P Petropulu, and John M Reid. Higher order spectra based deconvolution of ultrasound images. *IEEE Trans. Ultrason. Ferroelectr. Freq. Control.*, 42(6):1064–1075, 1995.
- [AT00] Martin E Anderson and Gregg E Trahey. A seminar on k-space applied to medical ultrasound. *Department of Biomedical Engineering, Duke University*, 2000.
- [AV85] Jean-Pierre Ardouin and AN Venetsanopoulos. Modelling and restoration of ultrasonic phased-array b-scan images. *Ultrasonic imaging*, 7(4):321–344, 1985.
- [BAF03] Vera Behar, Dan Adam, and Zvi Friedman. A new method of spatial compounding imaging. *Ultrasonics*, 41(5):377–384, 2003.
- [Bas08] Adrian Basarab. *Estimation du mouvement dans des séquences d’images échographiques: application à l’élastographie ultrasonore de la thyroïde*. PhD thesis, INSA de Lyon, 2008.
- [BBC11] Stephen Becker, Jérôme Bobin, and Emmanuel J Candès. NESTA: A fast and accurate first-order method for sparse recovery. *SIAM Journal on Imaging Sciences*, 4(1):1–39, 2011.
- [BBV04] Stephen Boyd, Stephen P Boyd, and Lieven Vandenberghe. *Convex optimization*. Cambridge university press, 2004.
- [BCB⁺05] Jerome MG Borsboom, Chien Ting Chin, Ayache Bouakaz, Michel Versluis, and Nico de Jong. Harmonic chirp imaging method for ultrasound contrast agent. *IEEE Trans. Ultrason. Ferroelectr. Freq. Control.*, 52(2):241–249, 2005.
- [BD80] JC Bamber and RJ Dickinson. Ultrasonic b-scanning: a computer simulation. *Physics in Medicine & Biology*, 25(3):463, 1980.
- [BD86] JC Bamber and C Daft. Adaptive filtering for reduction of speckle in ultrasonic pulse-echo images. *Ultrasonics*, 24(1):41–44, 1986.

- [Bey60] Robert T Beyer. Parameter of nonlinearity in fluids. *The Journal of the Acoustical Society of America*, 32(6):719–721, 1960.
- [Bey74] RT Beyer. Nonlinear acoustics naval ship system command. *Department of the Navy*, pages 91–101, 1974.
- [BJ77] Ronald E Bruck Jr. On the weak convergence of an ergodic iteration for the solution of variational inequalities for monotone operators in hilbert space. *Journal of Mathematical Analysis and Applications*, 61(1):159–164, 1977.
- [BPC⁺11] Stephen Boyd, Neal Parikh, Eric Chu, Borja Peleato, and Jonathan Eckstein. Distributed optimization and statistical learning via the alternating direction method of multipliers. *Found. Trends Mach. Learn.*, 3(1):1–122, 2011.
- [BRP⁺19a] Adrien Besson, Lucien Roquette, Dimitris Perdios, Matthieu Simeoni, Marcel Arditi, Paul Hurley, Yves Wiaux, and Jean-Philippe Thiran. A physical model of nonstationary blur in ultrasound imaging. *IEEE Trans. Comp. Img.*, 5(3):381–394, 2019.
- [BRP⁺19b] Adrien Besson, Lucien Roquette, Dimitris Perdios, Matthieu Simeoni, Marcel Arditi, Paul Hurley, Yves Wiaux, and Jean-Philippe Thiran. A physical model of nonstationary blur in ultrasound imaging. *IEEE Trans. Comput. Imaging*, 5(3):381–394, 2019.
- [BST14] Jérôme Bolte, Shoham Sabach, and Marc Teboulle. Proximal alternating linearized minimization for nonconvex and nonsmooth problems. *Mathematical Programming*, 146(1):459–494, 2014.
- [BT74] Albert E Beaton and John W Tukey. The fitting of power series, meaning polynomials, illustrated on band-spectroscopic data. *Technometrics*, 16(2):147–185, 1974.
- [BT09] Amir Beck and Marc Teboulle. A fast iterative shrinkage-thresholding algorithm for linear inverse problems. *SIAM journal on imaging sciences*, 2(1):183–202, 2009.

- [BTM⁺98] Marek Belohlavek, Kazuaki Tanabe, Sharon L Mulvagh, David A Foley, James F Greenleaf, and James B Seward. Image enhancement by noncontrast harmonic echocardiography. part ii. quantitative assessment with use of contrast-to-speckle ratio. In *Mayo Clinic Proceedings*, volume 73, pages 1066–1070. Elsevier, 1998.
- [BTN01] Aharon Ben-Tal and Arkadi Nemirovski. *Lectures on modern convex optimization: analysis, algorithms, and engineering applications*. SIAM, 2001.
- [Bur78] Christoph B Burckhardt. Speckle in ultrasound b-mode scans. *IEEE Transactions on Sonics and ultrasonics*, 25(1):1–6, 1978.
- [Bur96] PN Burns. Harmonic imaging with ultrasound contrast agents. *Clinical radiology*, 51:50–55, 1996.
- [CAN⁺17] Diego D.B. Carvalho, Andres Mauricio Arias Lorza, Wiro J. Niessen, Marleen de Bruijne, and Stefan Klein. Automated registration of freehand b-mode ultrasound and magnetic resonance imaging of the carotid arteries based on geometric features. *Ultrasound in Medicine Biology*, 43(1):273–285, 2017.
- [CBK15] Zhouye Chen, Adrian Basarab, and Denis Kouamé. A simulation study on the choice of regularization parameter in l_2 -norm ultrasound image restoration. In *2015 37th Annual International Conference of the IEEE Engineering in Medicine and Biology Society (EMBC)*, pages 6346–6349. IEEE, 2015.
- [CBK16a] Z. Chen, A. Basarab, and D. Kouamé. Reconstruction of enhanced ultrasound images from compressed measurements using simultaneous direction method of multipliers. *IEEE Trans. Ultrason., Ferroelect., Freq. Control*, 63(10):1525–1534, Oct 2016.
- [CBK16b] Zhouye Chen, Adrian Basarab, and Denis Kouamé. Compressive deconvolution in medical ultrasound imaging. *IEEE Trans. Med. Imag.*, 35(3):728–737, 2016.
- [CGC⁺00] Sabina Choudhry, Brian Gorman, J William Charboneau, Donald J Tradup, Rebecca J

- Beck, James M Kofler, and Debra S Groth. Comparison of tissue harmonic imaging with conventional us in abdominal disease. *Radiographics*, 20(4):1127–1135, 2000.
- [CH05] Richard Y Chiao and Xiaohui Hao. Coded excitation for diagnostic ultrasound: A system developer’s perspective. *IEEE Trans. Ultrason. Ferroelectr. Freq. Control.*, 52(2):160–170, 2005.
- [Che16] Zhouye Chen. *Reconstruction of enhanced ultrasound images from compressed measurements*. PhD thesis, Université Paul Sabatier-Toulouse III, 2016.
- [CHS17] Bianca Carpentier, Jessica Hayward, and Lori Strachowski. Enhancing your acoustics: ultrasound image optimization of breast lesions. *Journal of Ultrasound in Medicine*, 36(7):1479–1485, 2017.
- [CKDG80] PD Corl, GS Kino, CS DeSilets, and PM Grant. A digital synthetic focus acoustic imaging system. In *Acoustical Imaging*, pages 39–53. Springer, 1980.
- [CM91] John C Curlander and Robert N McDonough. *Synthetic aperture radar*, volume 11. Wiley, New York, 1991.
- [CP11] Patrick L Combettes and Jean-Christophe Pesquet. Proximal splitting methods in signal processing. In *Fixed-point algorithms for inverse problems in science and engineering*, pages 185–212. Springer, 2011.
- [CYFB03] Yan Chen, Ruming Yin, Patrick Flynn, and Shira Broschat. Aggressive region growing for speckle reduction in ultrasound images. *Pattern Recognition Letters*, 24(4-5):677–691, 2003.
- [CZBK15] Zhouye Chen, Ningning Zhao, Adrian Basarab, and Denis Kouamé. Ultrasound compressive deconvolution with p-norm prior. In *2015 23rd European Signal Processing Conference (EUSIPCO)*, pages 2791–2795. IEEE, 2015.
- [DC07] Ricardo G Dantas and Eduardo T Costa. Ultrasound speckle reduction using modified gabor filters. *IEEE Trans. Ultrason. Ferroelectr. Freq. Control.*, 54(3):530–538, 2007.

- [DDDM04] Ingrid Daubechies, Michel Defrise, and Christine De Mol. An iterative thresholding algorithm for linear inverse problems with a sparsity constraint. *Communications on Pure and Applied Mathematics: A Journal Issued by the Courant Institute of Mathematical Sciences*, 57(11):1413–1457, 2004.
- [DMM09] David L Donoho, Arian Maleki, and Andrea Montanari. Message-passing algorithms for compressed sensing. *Proceedings of the National Academy of Sciences*, 106(45):18914–18919, 2009.
- [Don95] David L Donoho. De-noising by soft-thresholding. *IEEE Trans. Inf. Theory*, 41(3):613–627, 1995.
- [EB92] Jonathan Eckstein and Dimitri P Bertsekas. On the douglas—rachford splitting method and the proximal point algorithm for maximal monotone operators. *Mathematical Programming*, 55(1):293–318, 1992.
- [EMVB⁺20] Oumaima El Mansouri, Fabien Vidal, Adrian Basarab, Pierre Payoux, Denis Kouamé, and Jean-Yves Tournet. Fusion of magnetic resonance and ultrasound images for endometriosis detection. *IEEE Trans. on Imag. Process.*, 29:5324–5335, 2020.
- [EPS⁺01] Robert R Entekin, Bruce A Porter, Henrik H Sillesen, Anthony D Wong, Peter L Cooperberg, and Cathy H Fix. Real-time spatial compound imaging: application to breast, vascular, and musculoskeletal ultrasound. In *Seminars in Ultrasound, CT and MRI*, volume 22, pages 50–64. Elsevier, 2001.
- [Ess09] Ernie Esser. Applications of lagrangian-based alternating direction methods and connections to split bregman. *CAM report*, 9:31, 2009.
- [FBDA09] Mario AT Figueiredo, Jose M Bioucas-Dias, and Manya V Afonso. Fast frame-based image deconvolution using variable splitting and constrained optimization. In *2009 IEEE/SP 15th Workshop on Statistical Signal Processing*, pages 109–112. IEEE, 2009.

- [FBK⁺00] Peter JA Frinking, Ayache Bouakaz, Johan Kirkhorn, Folkert J Ten Cate, and Nico De Jong. Ultrasound contrast imaging: current and new potential methods. *Ultrasound in medicine & biology*, 26(6):965–975, 2000.
- [FBKV18a] Mihai I Florea, Adrian Basarab, Denis Kouamé, and Sergiy A Vorobyov. An axially variant kernel imaging model applied to ultrasound image reconstruction. *IEEE Signal Process. Lett.*, 25(7):961–965, 2018.
- [FBKV18b] Mihai I Florea, Adrian Basarab, Denis Kouamé, and Sergiy A Vorobyov. Restoration of ultrasound images using spatially-variant kernel deconvolution. In *Proc. IEEE Int. Conf Acoust. Speech Signal Process. (ICASSP)*, pages 796–800, Calgary, 2018.
- [FK80] Mostafa Fatemi and Avinash C Kak. Ultrasonic b-scan imaging: Theory of image formation and a technique for restoration. *Ultrasonic imaging*, 2(1):1–47, 1980.
- [FNW07] Mário AT Figueiredo, Robert D Nowak, and Stephen J Wright. Gradient projection for sparse reconstruction: Application to compressed sensing and other inverse problems. *IEEE Journal of selected topics in signal processing*, 1(4):586–597, 2007.
- [FP07] Francisco Facchinei and Jong-Shi Pang. *Finite-dimensional variational inequalities and complementarity problems*. Springer Science & Business Media, 2007.
- [FP10] Jalal M Fadili and Gabriel Peyré. Total variation projection with first order schemes. *IEEE Transactions on Image Processing*, 20(3):657–669, 2010.
- [FSSH82] Victor S Frost, Josephine Abbott Stiles, K Sam Shanmugan, and Julian C Holtzman. A model for radar images and its application to adaptive digital filtering of multiplicative noise. *IEEE Transactions on pattern analysis and machine intelligence*, (2):157–166, 1982.
- [FW54] FE Fox and WA Wallace. Absorption of finite amplitude sound waves. *The Journal of the Acoustical Society of America*, 26(6):994–1006, 1954.

- [GCC⁺09] Hang Gao, Hon Fai Choi, Piet Claus, Steven Boonen, Siegfried Jaecques, G Harry Van Lenthe, Georges Van der Perre, Walter Lauriks, and Jan D'hooge. A fast convolution-based methodology to simulate 2-D/3-D cardiac ultrasound images. *IEEE Trans. Ultrason. Ferroelectr. Freq. Control*, 56(2):404–409, 2009.
- [GCS04] Savita Gupta, RC Chauhan, and SC Sexana. Wavelet-based statistical approach for speckle reduction in medical ultrasound images. *Medical and Biological Engineering and computing*, 42(2):189–192, 2004.
- [GL77] JC Gore and S Leeman. Ultrasonic backscattering from human tissue: a realistic model. *Physics in Medicine & Biology*, 22(2):317, 1977.
- [GM76] Daniel Gabay and Bertrand Mercier. A dual algorithm for the solution of nonlinear variational problems via finite element approximation. *Computers & Mathematics with Applications*, 2(1):17–40, 1976.
- [GO09] Tom Goldstein and Stanley Osher. The split bregman method for l1-regularized problems. *SIAM journal on imaging sciences*, 2(2):323–343, 2009.
- [GOL⁺94] Haitao Guo, Jan E Odegard, Markus Lang, Ramesh A Gopinath, Ivan W Selesnick, and C Sidney Burrus. Wavelet based speckle reduction with application to sar based atd/r. In *Proceedings of 1st International Conference on Image Processing*, volume 1, pages 75–79. IEEE, 1994.
- [HB88] Mark F Hamilton and David T Blackstock. On the coefficient of nonlinearity β in nonlinear acoustics. *The Journal of the Acoustical Society of America*, 83(1):74–77, 1988.
- [HB⁺98] Mark F Hamilton, David T Blackstock, et al. *Nonlinear acoustics*, volume 237. Academic press San Diego, 1998.
- [HBK⁺18] Mohamad Hourani, Adrian Basarab, Denis Kouamé, Jean-Marc Girault, and Jean-Yves Tourneret. Restoration of ultrasonic images using non-linear system identification and

- deconvolution. In *Proc. IEEE Int. Symp. Biomed. Imaging (ISBI)*, pages 1166–1169, Washington D.C., USA, April 4-7, 2018.
- [HBKT19a] M. Hourani, A. Basarab, D. Kouamé, and J. Tourneret. Joint deconvolution of fundamental and harmonic ultrasound images. In *IEEE Proc. Int. Ultrason. Symp. (IUS)*, pages 2067–2070, Glasgow, UK, 2019.
- [HBKT19b] Mohamad Hourani, Adrian Basarab, Denis Kouamé, and Jean-Yves Tourneret. Tissue reflectivity function restoration from fundamental and harmonic ultrasound images. In *Workshop on Signal Processing with Adaptive Sparse Structured Representations (SPARS 2019)*, Toulouse, France, July 1-4, 2019.
- [HBKT21] Mohamad Hourani, Adrian Basarab, Denis Kouamé, and Jean-Yves Tourneret. Ultrasound image deconvolution using fundamental and harmonic images. *IEEE Trans. Ultrason. Ferroelectr. Freq. Control.*, vol. 68:pages 993–1006, 2021.
- [HBM⁺20] Mohamad Hourani, Adrian Basarab, Oleg Michailovich, Giulia Matrone, Alessandro Ramalli, Denis Kouamé, and Jean-Yves Tourneret. Blind deconvolution of fundamental and harmonic ultrasound images. In *Proc. IEEE Int. Symp. Biomed. Imaging (ISBI)*, pages 854–857, Iowa, USA, April 3-7, 2020.
- [HBV⁺20] Mohamad Hourani, Adrian Basarab, François Varray, Denis Kouamé, and Jean-Yves Tourneret. Block-wise ultrasound image deconvolution from fundamental and harmonic images. In *Proc. IEEE Int. Ultrason. Symp. (IUS)*, pages 1–4, Virtual symposium, September 6-11, 2020.
- [HGG99] Xiaohui Hao, Shangkai Gao, and Xiaorong Gao. A novel multiscale nonlinear thresholding method for ultrasonic speckle suppressing. *IEEE transactions on medical imaging*, 18(9):787–794, 1999.
- [HLL⁺01] Oddvar Husby, Torgrim Lie, Thomas Lango, Jorn Hokland, and Havard Rue. Bayesian

- 2-d deconvolution: A model for diffuse ultrasound scattering. *IEEE Trans. Ultrason. Ferroelect. Freq. Control.*, 48(1):121–130, 2001.
- [HLT98] Bruno Haider, Peter A Lewin, and Kai E Thomenius. Pulse elongation and deconvolution filtering for medical ultrasonic imaging. *IEEE Trans. Ultrason. Ferroelectr. Freq. Control.*, 45(1):98–113, 1998.
- [HNO06] Per Christian Hansen, James G Nagy, and Dianne P O’leary. *Deblurring images: matrices, spectra, and filtering*. SIAM, 2006.
- [HUW⁺17] Elizabeth Herbst, Sunil Unnikrishnan, Shiyang Wang, Alexander L Klibanov, John A Hossack, and F William Mauldin Jr. The use of acoustic radiation force decorrelation-weighted pulse inversion (adw-pi) for enhanced ultrasound contrast imaging. *Investigative radiology*, 52(2):95, 2017.
- [ILV89] DOMENICO Iraca, Luigi Landini, and LUCIO Verrazzani. Power spectrum equalization for ultrasonic image restoration. *IEEE Trans. Ultrason. Ferroelectr. Freq. Control.*, 36(2):216–222, 1989.
- [Jen53] Jørgen Arendt Jensen. Field: A program for simulating ultrasound systems. In *Med. Biol. Eng. Comput.*, 1996, vol. 34, Supplement 1, Part 1: 351–353.
- [Jen91] Jo/rngen Arendt Jensen. A model for the propagation and scattering of ultrasound in tissue. *The Journal of the Acoustical Society of America*, 89(1):182–190, 1991.
- [Jen92] Jørgen Arendt Jensen. Deconvolution of ultrasound images. *Ultrasonic imaging*, 14(1):1–15, 1992.
- [Jen94] Jørgen Arendt Jensen. Estimation of in vivo pulses in medical ultrasound. *Ultrasonic imaging*, 16(3):190–203, 1994.
- [Jen96] Jørgen Arendt Jensen. *Estimation of blood velocities using ultrasound: a signal processing approach*. Cambridge University Press, 1996.

- [Jen07] Jørgen Arendt Jensen. Medical ultrasound imaging. *Progress in biophysics and molecular biology*, 93(1-3):153–165, 2007.
- [JKKY05] Jeremy A Johnson, Mustafa Karaman, and Butrus T Khuri-Yakub. Coherent-array imaging using phased subarrays. part i: Basic principles. *IEEE Trans. Ultrason. Ferroelectr. Freq. Control.*, 52(1):37–50, 2005.
- [JL94] Jorgen Arendt Jensen and Sidney Leeman. Nonparametric estimation of ultrasound pulses. *IEEE Trans. Biomed. Eng.*, 41(10):929–936, 1994.
- [JM97] Jørgen Arendt Jensen and Peter Munk. *Computer Phantoms for Simulating Ultrasound B-Mode and CFM Images*, pages 75–80. Springer US, Boston, MA, 1997.
- [JMGS93] Jørgen Arendt Jensen, Jan Mathorne, Torben Gravesen, and Bjarne Stage. Deconvolution of in-vivo ultrasound b-mode images. *Ultrasonic Imaging*, 15(2):122–133, 1993.
- [JNGP06] Jørgen Arendt Jensen, Svetoslav Ivanov Nikolov, Kim Løkke Gammelmark, and Morten Høgholm Pedersen. Synthetic aperture ultrasound imaging. *Ultrasonics*, 44:e5–e15, 2006.
- [JSF04] Jing Yi Jin, Glauber T Silva, and Alejandro C Frery. Sar despeckling filters in ultrasound imaging. *Latin American applied research*, 2004.
- [JT06] Radovan Jirik and Torfinn Taxt. High-resolution ultrasonic imaging using two-dimensional homomorphic filtering. *IEEE Trans. Ultrason. Ferroelectr. Freq. Control.*, 53(8):1440–1448, 2006.
- [JT08] Radovan Jirik and Torfinn Taxt. Two-dimensional blind bayesian deconvolution of medical ultrasound images. *IEEE Trans. Ultrason. Ferroelectr. Freq. Control.*, 55(10):2140–2153, 2008.
- [KHY20] Shujaat Khan, Jaeyoung Huh, and Jong Chul Ye. Unsupervised deconvolution neural network for high quality ultrasound imaging. In *Proc. IEEE Int. Ultrason. Symp. (IUS)*, pages 1–4. IEEE, 2020.

- [KKL⁺07] Seung-Jean Kim, Kwangmoo Koh, Michael Lustig, Stephen Boyd, and Dmitry Gorinevsky. An interior-point method for large-scale ℓ_1 -regularized least squares. *IEEE J Sel Top Signal Process.*, 1(4):606–617, 2007.
- [Kou] Denis Kouam. Ultrasound imaging: Systems, signals and image processing.
- [LMG⁺20] Jingfeng Lu, Fabien Millioz, Damien Garcia, Sébastien Salles, Wanyu Liu, and Denis Friboulet. Reconstruction for diverging-wave imaging using deep convolutional neural networks. *IEEE Trans. Ultrason. Ferroelectr. Freq. Control.*, 67(12):2481–2492, 2020.
- [LPC⁺05] Christos P Loizou, Constantinos S Pattichis, Christodoulos I Christodoulou, Robert SH Istepanian, Marios Pantziaris, and Andrew Nicolaidis. Comparative evaluation of despeckle filtering in ultrasound imaging of the carotid artery. *IEEE Trans. Ultrason. Ferroelectr. Freq. Control.*, 52(10):1653–1669, 2005.
- [LTN90] Armand Lopes, Ridha Touzi, and E Nezry. Adaptive speckle filters and scene heterogeneity. *IEEE transactions on Geoscience and Remote Sensing*, 28(6):992–1000, 1990.
- [MA03] Oleg Michailovich and Dan Adam. Robust estimation of ultrasound pulses using outlier-resistant de-noising. *IEEE Trans. on Med. Imag.*, 22(3):368–381, 2003.
- [MA05] Oleg V Michailovich and Dan Adam. A novel approach to the 2-D blind deconvolution problem in medical ultrasound. *IEEE Trans. Med. Imag.*, 24(1):86–104, 2005.
- [MBBK13] Renaud Morin, Stéphanie Bidon, Adrian Basarab, and Denis Kouamé. Semi-blind deconvolution for resolution enhancement in ultrasound imaging. In *Proc. IEEE Int. Conf. Image Process. (ICIP)*, Melbourne, Australia, Feb. 2013.
- [MBK12] Renaud Morin, Adrian Basarab, and Denis Kouamé. Alternating direction method of multipliers framework for super-resolution in ultrasound imaging. In *Proc. IEEE Int. Symp. Biomed. Imaging (ISBI)*, pages 1595–1598, 2012.

- [MBK19] Oleg Michailovich, Adrian Basarab, and Denis Kouame. Iterative reconstruction of medical ultrasound images using spectrally constrained phase updates. In *Proc. IEEE Int. Symp. Biomed. Imaging (ISBI)*, pages 1765–1768. IEEE, 2019.
- [MF06] SO Reza Moheimani and Andrew J Fleming. *Piezoelectric transducers for vibration control and damping*. Springer Science & Business Media, 2006.
- [MFBS98] Sharon L Mulvagh, David A Foley, Marek Belohlavek, and James B Seward. Image enhancement by noncontrast harmonic echocardiography. part i. qualitative assessment of endocardial visualization. In *Mayo Clinic Proceedings*, volume 73, pages 1062–1065. Elsevier, 1998.
- [MGJ⁺00] Thanassis X Misaridis, Kim Gammelmark, Christian H Jørgensen, Niklas Lindberg, Anders H Thomsen, Morten H Pedersen, and Jørgen A Jensen. Potential of coded excitation in medical ultrasound imaging. *Ultrasonics*, 38(1-8):183–189, 2000.
- [MHEK⁺07] Benoît Mesurole, Tarek Helou, Mona El-Khoury, Michael Edwardes, Elizabeth J Sutton, and Ellen Kao. Tissue harmonic imaging, frequency compound imaging, and conventional imaging: use and benefit in breast sonography. *Journal of ultrasound in medicine*, 26(8):1041–1051, 2007.
- [MI86] Philip McCord Morse and K Uno Ingard. *Theoretical acoustics*. Princeton university press, 1986.
- [Mic17] Oleg V Michailovich. Non-stationary blind deconvolution of medical ultrasound scans. In *Medical Imaging 2017: Ultrasonic Imaging and Tomography*, page 101391C. Proc. Int. Soc. Opt. Eng., Bellingham, WA, USA, Mar. 2017.
- [MJR⁺12] David Maresca, Krista Jansen, Guillaume Renaud, Gijs van Soest, Xiang Li, Qun Zhou, Nico de Jong, K Kirk Shung, and AFW Van der Steen. Intravascular ultrasound chirp imaging. *Applied Physics Letters*, 100(4):043703, 2012.

- [MLSBG89] RJ Massay, RB Logan-Sinclair, JC Bamber, and DG Gibson. Quantitative effects of speckle reduction on cross sectional echocardiographic images. *Heart*, 62(4):298–304, 1989.
- [MMGZ05] Qingyu Ma, Yong Ma, Xiufen Gong, and Dong Zhang. Improvement of tissue harmonic imaging using the pulse-inversion technique. *Ultrasound in medicine & biology*, 31(7):889–894, 2005.
- [Mor13] Renaud Morin. *Amélioration de la résolution en imagerie ultrasonore*. PhD thesis, Université de Toulouse, Université Toulouse III-Paul Sabatier, 2013.
- [MRTM86] Giulia Matrone, Alessandro Ramalli, Piero Tortoli, and Giovanni Magenes. Experimental evaluation of ultrasound higher-order harmonic imaging with filtered-delay multiply and sum (F-DMAS) non-linear beamforming. *Ultrasonics*, 2018, pp. 59-68, vol. 86.
- [MT07] Oleg Michailovich and Allen Tannenbaum. Blind deconvolution of medical ultrasound images: A parametric inverse filtering approach. *IEEE Trans. Image Process.*, 16(12):3005–3019, 2007.
- [MvRT82] Paul A Magnin, Olaf T von Ramm, and Frederick L Thurstone. Frequency compounding for speckle contrast reduction in phased array images. *Ultrasonic imaging*, 4(3):267–281, 1982.
- [NBSF82] VL Newhouse, NM Bilgutay, J Saniie, and ES Furgason. Flaw-to-grain echo enhancement by split-spectrum processing. *Ultrasonics*, 20(2):59–68, 1982.
- [Nes83] Yurii E Nesterov. A method for solving the convex programming problem with convergence rate $O(1/k^2)$. In *Dokl. akad. nauk Sssr*, volume 269, pages 543–547, 1983.
- [Ng07] James Kee Huat Ng. *Restoration of medical pulse-echo ultrasound images*. PhD thesis, Citeseer, 2007.
- [Nik02] Svetoslav Ivanov Nikolov. *Synthetic aperture tissue and flow ultrasound imaging*. Center for Fast Ultrasound Imaging, Technical University of Denmark, 2002.

- [NLG⁺07] Maartje M Nillesen, Richard GP Lopata, Inge H Gerrits, Livia Kapusta, Henkjan J Huisman, Johan M Thijssen, and Chris L de Korte. Segmentation of the heart muscle in 3-d pediatric echocardiographic images. *Ultrasound in medicine & biology*, 33(9):1453–1462, 2007.
- [NO98] James G Nagy and Dianne P O’Leary. Restoring images degraded by spatially variant blur. *SIAM Journal on Scientific Computing*, 19(4):1063–1082, 1998.
- [NPK⁺06] James Ng, Richard Prager, Nick Kingsbury, Graham Treece, and Andrew Gee. Modeling ultrasound imaging as a linear, shift-variant system. *IEEE Trans. Ultrason. Ferroelectr. Freq. Control*, 53(3):549–563, 2006.
- [NPK⁺07] James Ng, Richard Prager, Nick Kingsbury, Graham Treece, and Andrew Gee. Wavelet restoration of medical pulse-echo ultrasound images in an em framework. *IEEE Trans. Ultrason. Ferroelectr. Freq. Control.*, 54(3):550–568, 2007.
- [NWX10] Michael K Ng, Pierre Weiss, and Xiaoming Yuan. Solving constrained total-variation image restoration and reconstruction problems via alternating direction methods. *SIAM journal on Scientific Computing*, 32(5):2710–2736, 2010.
- [OBS01] Alan V Oppenheim, John R Buck, and Ronald W Schafer. *Discrete-time signal processing. Vol. 2*. Upper Saddle River, NJ: Prentice Hall, 2001.
- [O’D92] Matthew O’Donnell. Coded excitation system for improving the penetration of real-time phased-array imaging systems. *IEEE Trans. Ultrason. Ferroelectr. Freq. Control.*, 39(3):341–351, 1992.
- [Oel07] Michael L Oelze. Bandwidth and resolution enhancement through pulse compression. *IEEE Trans. Ultrason. Ferroelectr. Freq. Control.*, 54(4):768–781, 2007.
- [OMF10] Sonia H Contreras Ortiz, James Macione, and Martin D Fox. Enhancement of ultrasound images by displacement, averaging, and interlacing. *Journal of Electronic Imaging*, 19(1):011014, 2010.

- [Opp65] Alan V Oppenheim. Superposition in a class of nonlinear systems. 1965.
- [P. 71] P. R. Stepanishen. Transient radiation from pistons in an infinite planar baffle. *The Journal of the Acoustical Society of America*, 49(5B):1629–1638, 1971.
- [Pas79] Gregory B Passty. Ergodic convergence to a zero of the sum of monotone operators in hilbert space. *Journal of Mathematical Analysis and Applications*, 72(2):383–390, 1979.
- [PDRT09] Gianmarco F Pinton, Jeremy Dahl, Stephen Rosenzweig, and Gregg E Trahey. A heterogeneous nonlinear attenuating full-wave model of ultrasound. *IEEE Trans. Ultrason. Ferroelectr. Freq. Control*, 56(3):474–488, 2009.
- [PE03a] P. Phukpattaranont and E.S. Ebbini. Post-beamforming second-order volterra filter for pulse-echo ultrasonic imaging. *IEEE Trans. Ultrason. Ferroelectr. Freq. Control*, 50(8):987–1001, 2003.
- [PE03b] Pornchai Phukpattaranont and Emad S Ebbini. Post-beamforming second-order volterra filter for pulse-echo ultrasonic imaging. *IEEE Trans. Ultrason. Ferroelectr. Freq. Control*, 50(8):987–1001, 2003.
- [Per16] Antonios Perperidis. Postprocessing approaches for the improvement of cardiac ultrasound b-mode images: A review. *IEEE Trans. Ultrason. Ferroelectr. Freq. Control*, 63(3):470–485, 2016.
- [PHL06] Hu Peng, XueMei Han, and Jianyu Lu. Study on application of complementary golay code into high frame rate ultrasonic imaging system. *Ultrasonics*, 44:e93–e96, 2006.
- [PL06] Jerry L Prince and Jonathan M Links. *Medical imaging signals and systems*. Pearson Prentice Hall Upper Saddle River, 2006.
- [PM90] P. Perona and J. Malik. Scale-space and edge detection using anisotropic diffusion. *IEEE Transactions on Pattern Analysis and Machine Intelligence*, 12(7):629–639, 1990.

- [PPC11] Nelly Pustelnik, Jean-Christophe Pesquet, and Caroline Chaux. Relaxing tight frame condition in parallel proximal methods for signal restoration. *IEEE Transactions on Signal Processing*, 60(2):968–973, 2011.
- [PS94] Soo-Chang Pei and Jong-Jy Shyu. Eigenfilter design of 1-d and 2-d iir digital all-pass filters. *IEEE Trans. Signal Process.*, 42(4):966–968, 1994.
- [RKB08] Ramsharan Rangarajan, CV Krishnamurthy, and Krishnan Balasubramaniam. Ultrasonic imaging using a computed point spread function. *IEEE Trans. Ultrason. Ferroelectr. Freq. Control.*, 55(2):451–464, 2008.
- [RS77] Oleg Vladimirovich Rudenko and Stepan Ivanovich Soluian. *Theoretical foundations of nonlinear acoustics*. Springer, 1977.
- [RSHB17] Lucien Roquette, Matthieu Simeoni, Paul Hurley, and Adrien Besson. On an analytical, spatially-varying, point-spread-function. In *Proc. IEEE Int. Ultrason. Symp. (IUS)*, pages 1–4, Washington, DC, USA, 2017.
- [RW84] DE Robinson and Mt Wing. Lateral deconvolution of ultrasonic beams. *Ultrasonic imaging*, 6(1):1–12, 1984.
- [SBBG86] CM Sehgal, GM Brown, RC Bahn, and JF Greenleaf. Measurement and use of acoustic nonlinearity and sound speed to estimate composition of excised livers. *Ultrasound in medicine & biology*, 12(11):865–874, 1986.
- [SCB99] David Hope Simpson, Chien Ting Chin, and Peter N Burns. Pulse inversion doppler: a new method for detecting nonlinear echoes from microbubble contrast agents. *IEEE Trans. Ultrason. Ferroelectr. Freq. Control*, 46(2):372–382, 1999.
- [SCL05] Che-Chou Shen, Yi-Hong Chou, and Pai-Chi Li. Pulse inversion techniques in ultrasonic nonlinear imaging. *Journal of Medical Ultrasound*, 13(1):3–17, 2005.
- [SG07] Siddharth Singh and Abha Goyal. The origin of echocardiography: a tribute to ingedler. *Texas Heart Institute Journal*, 34(4):431, 2007.

- [SHTA04] Qingling Sun, John A Hossack, Jinshan Tang, and Scott T Acton. Speckle reducing anisotropic diffusion for 3d ultrasound images. *Computerized Medical Imaging and Graphics*, 28(8):461–470, 2004.
- [Sie88] WM Siebert. The early history of pulse compression radar-the development of an/fps-17 coded-pulse radar at lincoln laboratory. *IEEE Transactions on Aerospace and Electronic Systems*, 24(6):833–837, 1988.
- [SO09] Jose R Sanchez and Michael L Oelze. An ultrasonic imaging speckle-suppression and contrast-enhancement technique by means of frequency compounding and coded excitation. *IEEE Trans. Ultrason. Ferroelectr. Freq. Control.*, 56(7):1327–1339, 2009.
- [SPN⁺09] Ho-Chul Shin, Richard Prager, James Ng, Henry Gomersall, Nick Kingsbury, Graham Treece, and Andrew Gee. Sensitivity to point-spread function parameters in medical ultrasound image deconvolution. *Ultrasonics*, 49(3):344–357, 2009.
- [STJ99] Jarle Strand, Torfinn Taxt, and Anil K Jain. Two-dimensional phase unwrapping using a block least-squares method. *IEEE Transactions on Image Processing*, 8(3):375–386, 1999.
- [SVE94] Ralf Seip, Philip VanBaren, and Emad S Ebbini. Dynamic focusing in ultrasound hyperthermia treatments using implantable hydrophone arrays. *IEEE Trans. Ultrason. Ferroelectr. Freq. Control.*, 41(5):706–713, 1994.
- [Sza04] Thomas L Szabo. *Diagnostic ultrasound imaging: inside out*. Academic Press, San Diego, California, 2004.
- [Sza16] Teodora Szasz. *Advanced beamforming techniques in ultrasound imaging and the associated inverse problems*. PhD thesis, 2016.
- [Tak79] Y Takeuchi. An investigation of a spread energy method for medical ultrasound systems: Part one: Theory and investigation. *Ultrasonics*, 17(4):175–182, 1979.

- [TASVR86] GE Traney, JW Allison, SW Smith, and OT Von Ramm. A quantitative approach to speckle reduction via frequency compounding. *Ultrasonic Imaging*, 8(3):151–164, 1986.
- [Tax95] Torfinn Taxt. Restoration of medical ultrasound images using two-dimensional homomorphic deconvolution. *IEEE Trans. Ultrason. Ferroelectr. Freq. Control.*, 42(4):543–554, 1995.
- [Tax97] Torfinn Taxt. Comparison of cepstrum-based methods for radial blind deconvolution of ultrasound images. *IEEE Trans. Ultrason. Ferroelectr. Freq. Control.*, 44(3):666–674, 1997.
- [Tax01] Torfinn Taxt. Three-dimensional blind deconvolution of ultrasound images. *IEEE Trans. Ultrason. Ferroelectr. Freq. Control.*, 48(4):867–871, 2001.
- [TF99] Torfinn Taxt and Galina V Frolova. Noise robust one-dimensional blind deconvolution of medical ultrasound images. *IEEE Trans. Ultrason. Ferroelectr. Freq. Control.*, 46(2):291–299, 1999.
- [TGEP99] F Tranquart, N Grenier, V Eder, and L Pourcelot. Clinical use of ultrasound tissue harmonic imaging. *Ultrasound in Medicine Biology*, 25(6):889 – 894, 1999.
- [TH07] Gail Ter Haar. Therapeutic applications of ultrasound. *Progress in biophysics and molecular biology*, 93(1-3):111–129, 2007.
- [TJ04] Torfinn Taxt and Radovan Jirik. Superresolution of ultrasound images using the first and second harmonic signal. *IEEE Trans. Ultrason. Ferroelectr. Freq. Control.*, 51(2):163–175, 2004.
- [TNL09] Ihor Trots, Andrzej Nowicki, and Marcin Lewandowski. Synthetic transmit aperture in ultrasound imaging. *Archives of Acoustics*, 34(4):685–695, 2009.
- [Tou14] Matthieu Toulemonde. *New beamforming strategy for improved ultrasound imaging: application to biological tissues nonlinear imaging*. PhD thesis, Université Claude Bernard-Lyon I; Università degli studi (Florence, Italie), 2014.

- [TS01] Torfinn Taxt and Jarle Strand. Two-dimensional noise-robust blind deconvolution of ultrasound images. *IEEE Trans. Ultrason. Ferroelectr. Freq. Control.*, 48(4):861–866, 2001.
- [TSVR86] Gregg E Trahey, Stephen W Smith, and OT Von Ramm. Speckle pattern correlation with lateral aperture translation: Experimental results and implications for spatial compounding. *IEEE Trans. Ultrason. Ferroelectr. Freq. Control.*, 33(3):257–264, 1986.
- [TTC11] Bradley E Treeby, Mustafa Tumen, and Benjamin T Cox. Time domain simulation of harmonic ultrasound images and beam patterns in 3d using the k-space pseudospectral method. In *Proc. Int. Conf. on Medical Image Computing and Computer-Assisted Intervention*, Toronto, Canada, 2011.
- [Tup69] Geoff E Tupholme. Generation of acoustic pulses by baffled plane pistons. *Mathematika*, 16(2):209–224, 1969.
- [Var11] François Varray. *Simulation in nonlinear ultrasound: application to nonlinear parameter imaging in echo mode configuration*. PhD thesis, Université Claude Bernard-Lyon I; Università degli studi (Florence, Italie), 2011.
- [VBA⁺16] François Varray, Olivier Bernard, Sonia Assou, Christian Cachard, and Didier Vray. Hybrid strategy to simulate 3-D nonlinear radio-frequency ultrasound using a variant spatial PSF. *IEEE Trans. Ultrason. Ferroelectr. Freq. Control.*, 63(9):1390–1398, 2016.
- [VBTC13] François Varray, Olivier Basset, Piero Tortoli, and Christian Cachard. Creanuis: a non-linear radiofrequency ultrasound image simulator. *Ultrasound in medicine & biology*, 39(10):1915–1924, 2013.
- [VE08] Michael Vogt and Helmut Ermert. Limited-angle spatial compound imaging of skin with high-frequency ultrasound (20 mhz). *IEEE Trans. Ultrason. Ferroelectr. Freq. Control.*, 55(9):1975–1983, 2008.

- [VSCE19] Ruud JG Van Sloun, Regev Cohen, and Yonina C Eldar. Deep learning in ultrasound imaging. *Proc. IEEE*, 108(1):11–29, 2019.
- [WBH97] B Ward, AC Baker, and VF Humphrey. Nonlinear propagation applied to the improvement of resolution in diagnostic medical ultrasound. *The Journal of the Acoustical Society of America*, 101(1):143–154, 1997.
- [WBSS04] Zhou Wang, Alan C Bovik, Hamid R Sheikh, and Eero P Simoncelli. Image quality assessment: from error visibility to structural similarity. *IEEE Trans. Image Process.*, 13(4):600–612, 2004.
- [WNF09] Stephen J Wright, Robert D Nowak, and Mário AT Figueiredo. Sparse reconstruction by separable approximation. *IEEE Transactions on signal processing*, 57(7):2479–2493, 2009.
- [WSVS⁺20] RR Wildeboer, F Sammali, RJG Van Sloun, Y Huang, Peiran Chen, M Bruce, C Rabotti, S Shulepov, G Salomon, Benedictus C Schoot, et al. Blind source separation for clutter and noise suppression in ultrasound imaging: Review for different applications. *IEEE Trans. Ultrason. Ferroelectr. Freq. Control.*, 67(8):1497–1512, 2020.
- [XFG17] Zheng Xu, Mario Figueiredo, and Tom Goldstein. Adaptive admm with spectral penalty parameter selection. In *Artificial Intelligence and Statistics*, pages 718–727. PMLR, 2017.
- [YA02] Yongjian Yu and Scott T Acton. Speckle reducing anisotropic diffusion. *IEEE Transactions on image processing*, 11(11):1260–1270, 2002.
- [YCB⁺06] Yong Yue, Mihai M Croitoru, Akhil Bidani, Joseph B Zwischenberger, and John W Clark. Ultrasound speckle suppression and edge enhancement using multiscale nonlinear wavelet diffusion. In *2005 IEEE Engineering in Medicine and Biology 27th Annual Conference*, pages 6429–6432. IEEE, 2006.

- [YCM⁺07] Shiro Yoshifuku, Shigao Chen, Eileen M McMahon, Akiko Yoshikawa, Partho P Sen-
gupta, Josef Korinek, and Marek Belohlavek. Parametric harmonic-to-fundamental
ratio contrast echocardiography: a novel approach to identification and accurate mea-
surement of left ventricular area under variable levels of ultrasound signal attenuation.
Ultrasonics, 46(2):109–118, 2007.
- [YKHY18] Yeo Hun Yoon, Shujaat Khan, Jaeyoung Huh, and Jong Chul Ye. Efficient b-mode
ultrasound image reconstruction from sub-sampled rf data using deep learning. *IEEE
Trans. on Med. Imag.*, 38(2):325–336, 2018.
- [YZX12a] C. Yu, C. Zhang, and L. Xie. A blind deconvolution approach to ultrasound imaging.
IEEE Trans. Ultrason. Ferroelectr. Freq. Control, 59(2):271–280, 2012.
- [YZX12b] Chengpu Yu, Cishen Zhang, and Lihua Xie. A blind deconvolution approach to ul-
trasound imaging. *IEEE Trans. Ultrason. Ferroelectr. Freq. Control*, 59(2):271–280,
2012.
- [Zab69] EA Zabolotskaya. Quasi-plane waves, in the nonlinear acoustics of confined beams.
Sov. Phys. Acoust., 15:35–40, 1969.
- [ZAI03] Roger J Zemp, Craig K Abbey, and Michael F Insana. Linear system models for
ultrasonic imaging: Application to signal statistics. *IEEE Trans. Ultrason. Ferroelectr.
Freq. Control*, 50(6):642–654, 2003.
- [ZBKT14] Ningning Zhao, Adrian Basarab, Denis Kouame, and Jean-Yves Tournet. Restoration
of ultrasound images using a hierarchical bayesian model with a generalized gaussian
prior. In *IEEE International Conference on Image Processing (ICIP)*, pages 4577–4581.
IEEE, 2014.
- [ZBKT16] Ningning Zhao, Adrian Basarab, Denis Kouamé, and Jean-Yves Tournet. Joint
segmentation and deconvolution of ultrasound images using a hierarchical bayesian

- model based on generalized gaussian priors. *IEEE transactions on Image Processing*, 25(8):3736–3750, 2016.
- [ZLG98] Xuli Zong, Andrew F Laine, and Edward A Geiser. Speckle reduction and contrast enhancement of echocardiograms via multiscale nonlinear processing. *IEEE transactions on medical imaging*, 17(4):532–540, 1998.
- [ZWB⁺16a] N. Zhao, Q. Wei, A. Basarab, N. Dobigeon, D. Kouamé, and J. Y. Tourneret. Fast single image super-resolution using a new analytical solution for $\ell_2 - \ell_2$ problems. *IEEE Trans. Image Process.*, 25(8):3683–3697, Aug 2016.
- [ZWB⁺16b] Ningning Zhao, Qi Wei, Adrian Basarab, Denis Kouamé, and Jean-Yves Tourneret. Single image super-resolution of medical ultrasound images using a fast algorithm. In *Proc. IEEE Int. Ultrason. Symp. (IUS)*, pages 473–476, Prague, Czech Republic, 2016.
- [ZWB⁺16c] Nini Zhao, Qi Wei, Adrian Basarab, Denis Kouamé, and Jean-Yves Tourneret. Blind deconvolution of medical ultrasound images using a parametric model for the point spread function. In *Proc. IEEE Int. Ultrason. Symp. (IUS)*, pages 1–4, Tours, France, 2016.
- [ZWZ98] Wenwu Zhu, Yao Wang, and Jun Zhang. Total least-squares reconstruction with wavelets for optical tomography. *JOSA A*, 15(10):2639–2650, 1998.
-